Three-Dimensional Shape-Based Reconstructions in Medical Imaging

Athanasios D.Zacharopoulos

A dissertation submitted in partial fulfillment

of the requirements for the degree of

Doctor of Philosophy

of the

University of London.

Department of Computer Science

University College London

November 2004

ProQuest LLC
789 East Eisenhower Parkway
P.O. Box 1346
Ann Arbor, MI 48106-1346

Abstract

This thesis describes methods for reconstruction in non-linear tomography applications. The specific example application in this thesis is Optical Tomography (OT), which seeks the recovery of optical properties such as absorption, scattering and refractive index, given measurements of transmitted light through biological tissue of several centimetres in thickness. Previous methods pose such a problem as the optimisation of a model fitting procedure over a space of piecewise local basis functions such as pixels (or voxels in 3D).

We employ a parametrisation of closed surfaces using spherical harmonics based on constrained minimisation of the distortions occurring by the mapping of the surfaces, acquired from voxel images, to a unit sphere. This method could be used to describe parametrically any closed surface, and overcomes the restriction to just star-shaped objects that is commonly found in literature.

A surface meshing algorithm is proposed by applying the parametrisation to map regular surface meshes initially defined on the a unit sphere, by tessellation of an embedded icosahedron, upon the parametrically defined surfaces. This procedure creates regular sampled meshes which is a prerequisite for a good discretisation of a surface, in an automatic procedure.

A Boundary Element Method for OT is constructed, for the solution of the diffusion equation on realistic geometrical models, constructed from segmented Magnetic Resonance Images (MRI) or Computed Tomography (CT) scans.

In this work we propose a method for reconstruction of the boundaries of piecewise constant regions. The shape description for closed surfaces is used in a novel shape estimation inverse problem in 3D using OT measurements, based on a forward solution constructed from BEM and the regular meshes. Some examples are given that portray the capabilities of the proposed method.

Acknowledgements

Coming to the joyful task of thanking all those people that contributed to the completion of this thesis, I would like to start with all my friends that showed their love and support throughout all those years. It is a difficult task to thank you all by name, so in this page I hope that you will permit me to restrict myself to those that played a direct role to this work.

I am very grateful to my supervisor Prof. Simon R. Arridge, for his guidance and support, for always importing helpful ideas in my work, for believing in my work in the first place and for making the introduction to the world of research a pleasant procedure.

Many thanks to Prof. Jan Sikora from the Warsaw University of Technology for without his collaboration and hard work on BEM, this work could have never reached its current level.

I would like to thank Prof. Andrew Todd-Pokropek, for his valuable support and for being the first to suggest that I should be involved in such a research task.

I would like to thank Prof. Jari Kaipio and Marko Vauhkonen for their useful suggestions, and especially Ville Kolehmainen for his help and for sharing his valuable experience on inverse problems and also the rest of the great people of the Dept. of Applied Physics in the University of Kuopio, Finland, for their hospitality.

I would like to thank Prof. David Boas and Vasilis Ntziachristos, for their hospitality and assistance during my visit in MGH/MIT/HMS A.A. Martinos Center for Biomedical Imaging, Boston. Especially, I would like to thank Thomas Witzel for his assistance and our interesting collaboration.

I would like to thank Joao Oliveira for his help on meshing and Dimitrios Miras, Rachid Elaloufi and Steve Wright, for their comments. Also, Jason Riley and Olivier Coulon for their valuable help and all the guys from room 212 for making life in UCL a good experience. I

would like to especially thank Martin Schweiger, for his valuable comments and for being a numerical "wizard", the provider of many of the computational tools used in this work.

I would like to thank Prof. Marc Bonnet, Jorge Ripoll, Oliver Dorn, and Michael Quicken, for their helpful suggestions, and also Adam Gibson and Richard Bayford for the MRI and CT data used in this work.

Above all, I wish to thank my father, Dimitrios Zacharopoulos, my mother Evaggelia Lomef Zacharopoulou and my sister Maria-Niki, for bringing me up in an environment that admired studies and research, and therefore I dedicate this work to them.

This work was financially supported by EPSRC GR/N14248/01 and the UK Medical Research Council Grant No. D2025/31. This sponsorship is gratefully acknowledged.

To my parents, Dimitrios and Evaggelia

Contents

List of Figures

Chapter 1

Prologue

1.1 Introduction

This thesis proposes methods for image reconstruction in non-linear tomography applications. Tomography, as a technique for creation of three dimensional images for the inside of the human body based on non-invasive measurements, has become one of the most prominent topics for the medical imaging community. The demand for safe, non-ionising methods that have the potential to provide information on structure and functional activity inside the human body has forced the evolution of new tomographic methods.

The specific example application in this thesis is Optical Tomography (OT), which seeks the recovery of optical properties such as light absorption and scattering, given measurements of transmitted light through biological tissue of several centimetres in thickness. There are several physiologically interesting observations which can be derived from the knowledge of the absorption and scattering of light from tissue including tissue oxygenation, blood volume and blood oxygenation [8]. In a typical measurement setup for OT, near infra-red light is guided to the body from a laser source by using optic fibers attached to the surface. The amount of light that is transmitted through the body is measured on the surface by using measurement fibers and light sensitive detectors. The objective of the image reconstruction is to estimate the absorption and diffusion or scattering coefficients within the body from the photon transmission data on the surface. Primary applications are the detection and classification of tumourous tissue in the breast, monitoring of the oxygenation level in infant brain tissue and functional brain activation studies.

The measurements on the surface are linked to the actual optical properties of a body only

through known physical laws. An inverse operator that given the measurements will produce the optical properties is not generally known. Therefore, the common reconstruction procedure is a non-linear inverse problem. Such an approach is based on a forward model that given the optical parameters calculates the theoretical measurements on the surface. With optimisation techniques, iteratively, one finds the optical parameters corresponding to the simulated data that will best fit , in a least squares sense, to the measured data. This problem is known to be ill-posed in the sense that even small errors in the measured data (noise), may cause arbitrary large errors in the estimate of the optical parameters.

Previous methods formulate such a problem as the optimisation of a model fitting procedure over a space of piecewise local basis functions such as pixels (or voxels in 3D). The forward model can be defined by a partial differential equation, in this case the diffusion approximation and a geometrical model of the body under investigation, usually a discretisation of the body's volume in small elements. This forward model, for complicated geometries, is commonly solved numerically using the Finite Elements Method.

However, for the geometry of human body parts such as the head, the creation of such a discretisation has been proven a laborious task. On the other hand, the necessary resolution for a good discretisation introduces a large number of parameters for the forward model, and therefore increases the size of the search space for the inverse solution.

We propose, in this thesis, a parameterisation method for the boundaries of regions with piecewise constant optical parameters using spherical harmonics, exploiting the fact that those regions can be described by closed surfaces topologically equivalent to a sphere. Segmented Magnetic Resonance Imaging (MRI) or Computed Tomography (CT) voxel images, could be used to define the geometry of the internal body as a set of nested, disjoint surfaces. An approximation to an invertible and continuous mapping from those surfaces to the unit sphere could then be defined by solving a constrained minimisation problem on the surface of the sphere. This mapping would allow the representation of those surfaces into suitable basis functions like spherical harmonics. The shape of surfaces could be approximated by a finite number of few spherical harmonics coefficients.

Furthermore, the mapping to the sphere could be used in an automatic procedure to construct regular sampled discretisations (meshes) of the body's geometry. Any mesh defined by the em-

bedding of a tesselated icosahedron on a sphere, could be mapped on the parametric surfaces. Any created mesh would inherit the regular spacing of the faces on the tesselated icosahedron. The surface meshes could be used to produce a geometric model of the domain under investigation.

In addition to the parametrisation and meshing we propose a method for the reconstruction of the boundaries of those regions using OT measurements on the external surface. A Boundary Element Method (BEM), based on the Green's second theorem that associates the integrals of a function over a volume to the integrals over the volume's boundary, is tested as a computational method for the forward problem. Employing the shape description of the regions boundaries in a finite number of spherical harmonic coefficients, the reconstruction of the image for the optical properties would become the recovery of those coefficients. The search space for the data fitting has the size of the finite number of spherical harmonics coefficients that define the boundaries between the regions with piecewise constant optical parameters.

Results presented in this dissertation, display that the method can be applied to the recovery of the shape and location from regions with piecewise constant optical properties. The method employs *a-priori* information for the internal geometry of the domain under investigation and reduces the search space for the inversion optimisation and therefore restrains the ill-posed behaviour of the problem.

1.2 Aims and Contents of this Thesis

The purpose of this thesis is to develop a shape based, three dimensional reconstruction method for OT. The main contributions of this thesis are:

- A description of closed surfaces via parameterisation using spherical harmonics basis expansion. The procedure consists of an initial mapping of MRI or CT volumetric data, upon a sphere and a constraint optimisation procedure to ensure the continiouty and invertibility of that mapping. The closed surfaces are then approximated by a finite number of spherical harmonics coefficients.

- An automatic surface meshing algorithm based on the parametrically defined surfaces. Starting from regular meshes defined by embedding a tesselated icosahedron on the sphere, we employ the spherical harmonics representation to lay them upon the parametric surfaces.

- An application of BEM for the forward problem in OT. The BEM is used as the computational method for the solution of the diffusion equation on meshes that approximate realistic geometries and are defined by spherical harmonics shape coefficients.

- A three dimensional shape based reconstruction approach for regions with piecewise constant optical properties using OT measurements. Defined as a least squares minimisation between the observed data and those produced from the application of the BEM forward problem. The search space for the optimisation becomes that of the geometric parameters that describe the internal geometry of the body.

This dissertation is structured as follows. In chapter 2 a short review on the general inversion theory is given with emphasis on the tomography applications and the shape based approach. Following the definitions of the terms forward and inverse problem and some of their most important properties, the least squares method for the solution of the inverse problem is presented. Tomography inverse problems examples are given for the linear, CT, and the non-linear, OT, case. This thesis discusses a shape based approach; therefore we present the general definition and some background from literature both for the implicit level set and for the explicit FEM-BEM and shape parametrisation approaches.

Chapter 3 deals with the physical laws that define the model used for OT. The Radiative Transfer Equation formed to describe the transportation of light through biological tissue and the diffusion approximation used in our approach are presented. The physical model of light's behaviour inside scattering medium is of paramount importance in the constitution of the forward problem therefore details about the experimental setup, the sources, the detectors and the different signals used in the construction of a realistic model are presented.

In chapter 4, a short review of the Boundary Element Method (BEM) is given. Starting from the assumption that human body consists of distinct regions with piecewise constant optical properties the theoretical approach with the application of the second Green's theorem for the solution of the diffusion equation in a 3D domain is given. The description continues with the actual details of the numerical implementation of BEM. From the formulation of a linear matrix system of equations to the integration techniques over the boundary elements the procedure that will be used for the solution of the forward problem is explained. Finally, results from BEM that are very close to the analytic solution for the sphere case are presented to support our choice for this numerical method.

The subject of chapter 5 is optimisation. The inverse problem solution is based on the fitting of theoretical constructed data to the real ones with the help of least squares minimisation. Also, the parametrisation procedure for the mapping of closed surfaces upon the sphere is heavily depended on constrained optimisation. The terms involved in a typical optimisation problem and some commonly used unconstrained optimisation methods are discussed. Next, the constrained optimisation problem is defined and an orthogonal spaces approach is explained with simple examples given to enhance comprehension. Finally, the optimisation approach to the least squares problem using Newton like methods and the extensions to the Levenberg Marquardt method are presented.

Chapter 6 deals with the problem of the parametrisation for closed surface by approximating a mapping upon a unit sphere. The initial mapping of the closed surface extracted from a 3D voxel image is the first step. Following, the application of constrained optimisation on the specific problem is given with the definition of the constraints involved and the methods used for the solution. The problem of creating a parametric description for a baby's scalp surface segmented from a MRI is used for illustration.

As a product of this work, chapter 7 deals with the reconstruction of the surface using spherical harmonics decomposition. A short description in a finite number of parameters for the shape of the parameterised volumetric object is constructed. Results are shown for the MRI data. Furthermore, the contribution of the parametrisation method in surface meshing is reviewed. Regular meshes on the sphere are created by the tessellation of an embedded icosahedron and then mapped on the parametrically described surface. A multi-layer model application is presented.

In chapter 8 the method for the recovery of smooth surface boundaries of piecewise constant absorption and diffusion coefficients is presented. The forward model for the shape based approach is defined using BEM for the numerical implementation of the physical model for OT starting from the geometrical parameters and the *a-priori* known optical properties. Then the inverse problem in a shape based approach is presented with the formulation of a least squares minimisation between observed and theoretical data in the search space of the geometrical parameters. Results presented for the shape based reconstruction approach illustrate the abilities and constraints of the proposed method.

Conclusion remarks along with some suggestions for future work can be found in the last chapter.

Chapter 2

Inverse Problem in Tomography and Imaging

"Forty-two!" yelled Loonquawl. "Is that all you've got to show for seven and a half million years' work?"
"I checked it very thoroughly," said the computer, "and that quite definitely is the answer. I think the problem, to be quite honest with you, is that you've never actually known what the question is."
Douglas Adams, from "The Hitch Hiker's Guide to the Galaxy"

2.1 Introduction

Human cognition in every day affairs is mostly based on synthetic, forward reasoning; given a *question* we are trying to find an appropriate *answer*. But then what about the problems like the one graphically described by D.Adams in the above quote? Then, the *inverse problem* is the manifestation of a suitable question for a given answer, based on the establishment of the forward relation between questions and answers, to be called the *forward problem*.

In a less philosophical frame, in science and engineering, inverse problems try to recover unknown model parameters from experimental observations, only indirectly related to those parameters. Hence, inverse problems are used on several applications of non-destructive evaluation, including medical imaging. Known applications spread from Magneto-Encephalography (MEG)[84], Electric Encephalography (EEG)[92], Electrical impedance Tomography (EIT)[30, 31], Diffusion Optical Tomography [11, 14, 13, 2, 115], etc.

Unfortunately, a typical feature of such inverse problems is ill-posedness, which could relate to the non-uniqueness of the solution or to a strong influence from noise. To make things more meaningful, we will provide a definition for the forward and inverse problems. Finally, we will describe the shape based approach, which is the main theme of this thesis.

2.2 Definition of the problem

Initially, we define the class of model parameters in a domain Ω, expressed using suitable functions f. For this class we assign a distance metric $\| \ \|^2$ in order to establish when two objects are close or far from each other. Then the class becomes a metric space typically, [11], a Sobolev space $\mathcal{H}^1(\Omega)$, which we call the *parameters space.*

Then, we define the class of the observable data described by functions g. For this class that contains the noisy and noise-free observation data we assign a similar metric. We can then define the metric space which we call the *data space* and is defined typically as the Sobolev space $\mathcal{H}^{-\frac{1}{2}}(\partial\Omega)$.

In practice, we need to consider the function f as a space distribution. A distribution or generalised function is defined as the inner product of $\langle f, \psi \rangle$, where ψ are some *test functions* with compact support. The representation of f will be then:

$$\mathbf{f}(\mathbf{r}) = \int_{\Omega} f(\mathbf{t}) \cdot \psi_i(\mathbf{r}+\mathbf{t}) d\mathbf{t} \approx \sum_i f_i \, \psi_i(\mathbf{r}) \tag{2.1}$$

The most common distribution is with the Dirac δ-function, that has the fundamental property:

$$\int_{-\infty}^{+\infty} f(\mathbf{r})\delta(\mathbf{r}+\mathbf{a}) = f(\mathbf{a}) \tag{2.2}$$

For the rest of this thesis we will consider the discrete version for parameters and data. The parameters will be expressed as vectors $\mathbf{f} = \{f_1, \cdots, f_M\} \in \mathbb{R}^M$, and the parameters vector space will be denoted $\mathbb{X} \subset \mathbb{R}^M$. The data $\mathbf{g} = \{g_1, \cdots, g_M\} \in \mathbb{R}^N$ will then live in the vector space $\mathbb{Y} \subset \mathbb{R}^N$.

In this setting the forward problem is defined by a mapping (operator) $\mathcal{K} : \mathbb{R}^M \rightarrow \mathbb{R}^N$, which transforms any object $\mathbf{f}$ of the space $\mathbb{X}$ into a noise free data $\mathbf{g}$ of the space $\mathbb{Y}$. Hence,we have:

$$\mathbf{g} = \mathcal{K}(\mathbf{f}). \tag{2.3}$$

If the model is linear in respect to $\mathbf{f}$, the forward model can be written as

$$\mathbf{g} = \mathrm{K}\,\mathbf{f} \tag{2.4}$$

where $\mathrm{K} \in \mathbb{R}^{N \times M}$.

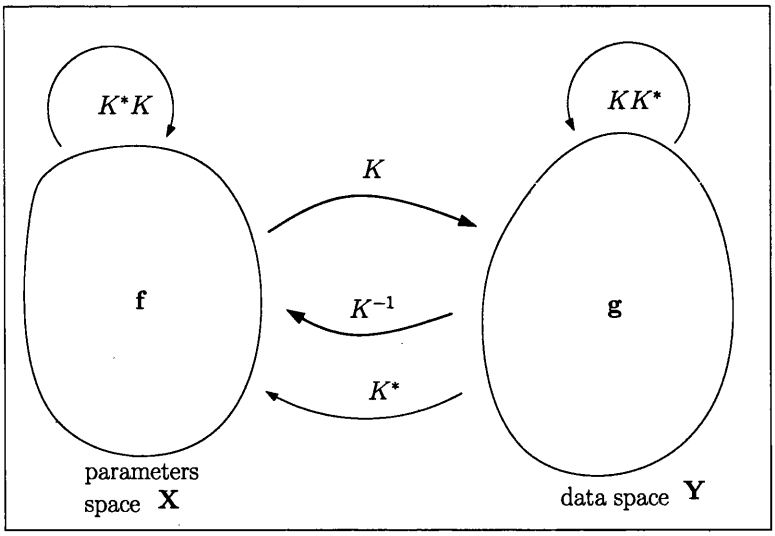

Figure 2.1: Inverse problem and the relations between the parameter and data spaces

We make the following definitions for the matrix K.

The *range* of the matrix $\mathrm{K} : \mathbb{R}^M \rightarrow \mathbb{R}^N$ is defined as

$$\mathcal{R}(\mathrm{K}) = \{\mathbf{g} \in \mathbb{R}^N | \mathbf{g} = \mathrm{K}\,\mathbf{f},\ \forall \mathbf{f} \in \mathbb{R}^M\}$$

The *nullspace* of K is defined as

$$\mathcal{N} = \{\mathbf{f} \in \mathbb{R}^M | \mathrm{K}\,\mathbf{f} = 0\}.$$

The *adjoint* K* of K is defined so that:

$$\langle \mathrm{K}\,\mathbf{f}, \mathbf{g} \rangle_{\mathrm{Y}} = \langle \mathbf{f}, \mathrm{K}^*\mathbf{g} \rangle_{\mathrm{X}}$$

where $\langle\ ,\ \rangle_{\mathbb{J}}$ denotes the inner product defined for a space $\mathbb{J}$.

To recap, in the above consideration the forward problem is set to "predict" the data g when the model parameters f are given. The corresponding inverse problem will be then to estimate the parameters f that could have produced the given data g. In the ideal case without measurement noise that would be the solution of

$$\mathrm{K}\mathbf{f} - \mathbf{g} = 0. \tag{2.5}$$

Commonly, in most practical situations modelling errors and measurement noise the measured data $\mathbf{g}$ does not belong to the direct range of K, $\mathbf{g} \notin \mathcal{R}(\mathrm{K})$. Then, it is common for the inversion procedure to be ill-posed.

In the Hadamard sense an inverse problem will be characterised as *well-posed* [128] if certain conditions apply:

1. [Existence] : For each $\mathbf{g} \in \mathbb{Y}$ there exists an $\mathbf{f} \in \mathbb{X}$ for which $\mathcal{K}(\mathbf{f}) = \mathbf{g}$ holds.

2. [Uniqueness] : The solution $\mathbf{f}$ is unique, i.e. $\mathcal{K}(\mathbf{f}_1) = \mathbf{g}$ and $\mathcal{K}(\mathbf{f}_2) = \mathbf{g}$ then $\mathbf{f}_1 = \mathbf{f}_2$, and

3. [Stability] : The solution is stable in respect to perturbations in $\mathbf{g}$. That is : If $\mathcal{K}(\mathbf{f}) = \mathbf{g}$ and $\mathcal{K}(\mathbf{f}') = \mathbf{g}'$ then $\mathbf{f} \rightarrow \mathbf{f}'$ when $\mathbf{g} \rightarrow \mathbf{g}'$

The problems that are not well-posed are called *ill-posed.*

Usually one or more of the well posedness conditions is not valid, and the usual way to define a solution is a Newton iterative technique based on successive linearisations of the model $\mathcal{K}(\mathbf{f})$, in order to minimise the least square distance $\Xi(\mathbf{f})$ between the measured data $\mathbf{g}$ and the predicted from the forward $\mathcal{K}(\mathbf{f})$ as

$$\mathbf{f}_{\min} = \arg\min_{\mathbf{f}} \Xi(\mathbf{f}), \tag{2.6}$$

where

$$\Xi(\mathbf{f}) := \|\mathbf{g} - \mathcal{K}(\mathbf{f})\|^2 \tag{2.7}$$

This minimisation ensures the existence of an approximate solution but is inadequate to ensure uniqueness and stability.

For finite space inverse problems an increased stability in the sense of the definition above should be featured, since the small perturbations in the data $\mathbf{g}$ cannot cause arbitrary large errors in the solution $\mathbf{f}$. However, in reality the discretisation used in inverse methodologies, renders the ill-posed inverse problem far too sensitive to small errors in the data and thus "effectively" ill-posed.

One typical method used for the analysis of a linear inverse problem is Singular Value Decomposition (SVD) of the forward operator K.

2.3 Singular Value decomposition of the matrix K

A linear forward operator $\mathrm{K} : \mathbb{X} \rightarrow \mathbb{Y}$ is expressed by the matrix $\mathrm{K} \in \mathbb{R}^{N \times M}$. The *singular value decomposition* of the *r-rank* matrix K is defined by:

$$\mathrm{K} = \mathrm{USV}^T \tag{2.8}$$

where

$$\mathrm{S} = \begin{pmatrix} \Sigma_r & 0 \\ 0 & 0 \end{pmatrix} \in \mathbb{R}^{N \times M}, \tag{2.9}$$

and $\Sigma_r = \mathrm{diag}(\lambda_1, \ldots, \lambda_r)$, with

$$\lambda_1 \geq \lambda_2 \geq \ldots \geq \lambda_r > 0$$

and $r \leq \min\{M, N\}$. The numbers λ_i are called *singular values.* The matrices $\mathrm{U} = (\mathbf{u}_1, \ldots, \mathbf{u}_N) \in \mathbb{R}^{N \times N}$, and $\mathrm{V} = (\mathbf{v}_1, \ldots, \mathbf{v}_M) \in \mathbb{R}^{M \times M}$ are orthonormal. The vectors $\mathbf{u}_i$ and $\mathbf{v}_i$ are called *left* and *right singular vectors* respectively, and satisfy:

$$\mathbf{u}_i^T \mathbf{u}_j = \delta_{ij} \quad , \quad \mathbf{v}_i^T \mathbf{v}_j = \delta_{ij} \tag{2.10}$$

$$\mathrm{K}\mathbf{v}_i = \lambda_i \mathbf{u}_i \quad , \quad \mathrm{K}^T \mathbf{u}_i = \lambda_i \mathbf{v}_i \tag{2.11}$$

$$\tag{2.12}$$

Where δ_{ij} is the Kronecker delta. From the above $U^T = U^{-1}$ and $V^T = V^{-1}$. Consider the forward mapping $\mathrm{K}\,\mathbf{f} = \mathbf{g}$ for an arbitrary vector $\mathbf{f} \in \mathbb{X}$. Given the SVD of K, $\mathbf{f}$ can be expressed as a linear combination of the right singular vectors $\mathbf{v}_i$

$$\mathbf{f} = \sum_{i=1}^{r} (\mathbf{v}_i^T\, \mathbf{f})\, \mathbf{v}_i. \tag{2.13}$$

Therefore we have:

$$\mathbf{g} = \sum_{i=1}^{r} \mathbf{u}_i\, \lambda_i (\mathbf{v}_i^T\, \mathbf{f}). \tag{2.14}$$

The *condition number* of the matrix K can be defined as

$$\text{cond}(\mathrm{K}) = \frac{\lambda_1}{\lambda_r} \tag{2.15}$$

and certain classifications for the nature of the ill-posedness of matrix K can be defined:

- The problem is *rank-deficient*(non-unique) if $r < min\{M, N\}$. This implies that at least one of the columns and rows of K is a linear combination of some other columns or rows. Therefore $\mathcal{N}(\mathrm{K}) \neq \{0\}$.

- In some cases where $\mathcal{N}(\mathrm{K}) = \{0\}$, K could have some very small singular values say $\{\lambda_{k+1}, \ldots, \lambda_r\}$ with a clear gap between them and the bigger values $\{\lambda_1, \ldots, \lambda_k\}$. In this case K contains $r - k$ almost linearly dependent rows and columns an the problem is said to be *numerically rank-deficient* with numerical rank k.

- Discrete ill-posed problems are characterised by a singular value spectrum, $\{\lambda_1, \ldots, \lambda_r\}$ that decays gradually to almost zero without a clear gap between bigger and smaller values in the SVD spectrum. Since there is no clear gap in this case the notion of numerical rank is arbitrary. A typical feature of the singular vectors $\mathbf{v}_i$ and $\mathbf{u}_i$ is that they become more and more oscillatory as i increases.[128].

Both numerical rank-deficient and discrete inverse problems are characterised by a very large condition number $\text{cond}(\mathrm{K})$. They both are to be considered as effectively underdetermined problems.

2.4 Least squares estimation

Having defined SVD, as a tool for the analysis of inverse problems, we will use it to draw some more conclusions for the solution of the inverse problem. For the ill-posed linear inverse problem the common approach is to minimise the distance between calculated and observed data using the least square functional (2.7), to estimate $\mathbf{f}_{\text{min}}$. From the least squares solution we get the minimum norm vector for $\mathbf{g} - \mathrm{K}\mathbf{f}$. Therefore,

$$\mathrm{K}^T \mathrm{K}\, \mathbf{f} = \mathrm{K}^T \mathbf{g} \tag{2.16}$$

In the case of a full r-rank matrix K, $r = M < N$ which yields $\mathcal{N}(\mathrm{K}) = \{0\}$, the solution can be obtained by

$$\mathbf{f}_{\min} = (\mathrm{K}^T\,\mathrm{K})^{-1}\,\mathrm{K}^T\,\mathbf{g} \tag{2.17}$$

where, the matrix $\mathrm{K}^\dagger = (\mathrm{K}^T\,\mathrm{K})^{-1}\,\mathrm{K}^T$ is called the *Moore Penrose generalised inverse* of K.

Going back to the more general case for K the SVD for the pseudoinverse $\mathrm{K}^\dagger$ gives,

$$\mathrm{K}^\dagger = \mathrm{V}\begin{pmatrix} \Sigma_r^{-1} & 0 \\ 0 & 0 \end{pmatrix}\mathrm{U}^T \tag{2.18}$$

And the solution is obtained as $\mathbf{f}_{\min} = \mathrm{K}^\dagger\,\mathbf{g}$.

For a numerically k-rank deficient K, $(k < r)$, the terms that correspond to the smaller singular values λ_i with $i > k$, are strongly amplified by the factor $1/\lambda_i$. This could introduce a strong domination of noise in data that are parallel to the corresponding singular vectors $\mathbf{u}_i,\ \ i > k$.

In the non-linear case the least squares formulation will be

$$\Xi(\mathbf{f}) := \|\mathbf{g} - \mathcal{K}(\mathbf{f})\|^2 \tag{2.19}$$

The natural way to minimise that for the non-linear problem is through an iterative Newton-Gauss formula where the update $\mathbf{f}^{(k+1)}$ for $\mathbf{f}$ is given by:

$$\mathbf{f}^{(k+1)} = \mathbf{f}^{(k)} + \left(J_k^T J_k\right)^{-1} J_k^T(\mathbf{g} - \mathcal{K}(\mathbf{f}^{(k)})) \tag{2.20}$$

where the notation $J_k = \frac{\partial \mathcal{K}}{\partial \mathbf{f}}(\mathbf{f}^{(k)})$ has been introduced for the derivative of operator $\mathcal{K}$. The derivation and further discussion on the Newton method and other optimisation methods follows in chapter 5.

2.5 Regularisation

To overcome the difficulties due to the ill-posed nature of the inverse problem, regularisation techniques have been used. Regularisation works on finding a well posed approximation for the ill-posed problem so that the regularised solution, which will be stable and unique, would be as close as possible to the solution of the equivalent ill-posed.

One commonly used method for regularisation is the damping of the smaller singular values in (2.9). This method, called Truncated-SVD (TSVD), replaces the singular values $\{\lambda_{k+1}, \ldots, \lambda_r\}$ with zeros. Tikhonov regularisation [70, 79, 128], achieves similar results by augmenting the original least squares problem (2.30), with additional regularisation penalty functionals which stabilise the solution.

$$\Xi(\mathbf{f}) = \|\mathbf{g} - \mathcal{K}(\mathbf{f})\|^2 + pA(\mathbf{f}) \tag{2.21}$$

Where $A(\mathbf{f}) > 0$ is the regularising functional term and $p > 0$ the regularisation parameter.

By the regularisation of the least square problem some *a-priori* information about the sought quantity is introduced into the optimisation problem. Typically, the *a-priori* information is related to the overall size or smoothness of the sought quantity. For example in TSVD the truncated singular values $\{\lambda_{k+1}, \ldots, \lambda_r\}$ were representing the higher frequency components. The effect of their truncation can be interpreted as a low pass filtering of the solution with a cut-off frequency k.

Sometimes, some specific information about the structure of the body Ω could be known. The prior information may be related for example to the (approximate) known internal geometry of the generally unknown body Ω, or even to the model parameters in some of the regions within the body Ω. It is reasonable to expect that the utilisation of the known properties will improve the image reconstruction process.

2.6 Inverse problem and tomography

Tomography, coming from the Greek word for the writing or representation of an object by using slices, refers to the methods used to reconstruct the internal structure of a 3D object by using measurements taken on its external surface. Usual practice for tomographic applications is the construction of a forward problem using known physical laws based on the parameters $\mathbf{f}$. The reconstruction of $\mathbf{f}$ now becomes the reconstruction of the distribution of values of f_i, $i = \{1, \cdots, M\}$ in the domain Ω discretised into a raster of pixels.

2.6.1 Linear case : Computed Tomography

One of the most well known applications of the inverse problem in medical imaging is in Computed Tomography CT. The basis behind CT is the absorption of X-rays by the human tissues. This absorption in the human body at a point $\mathbf{r}$ will be described by the function $f(\mathbf{r})$ whose value at $\mathbf{r}$ is the linear attenuation coefficient for this position. This function is roughly proportional to the density of the body tissue and it is the object of the CT imaging system.

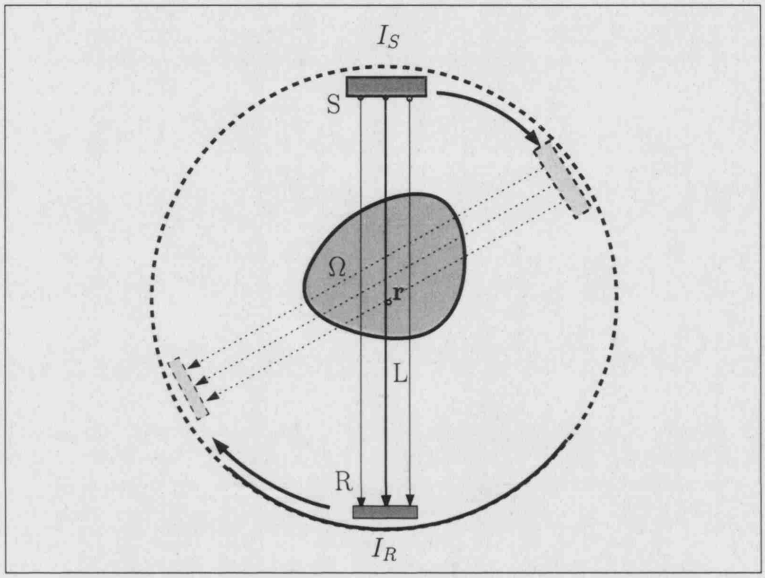

Figure 2.2: Schematic representation of the elementary process of Computed Tomography.

Consider a finely collimated source S emitting a pencil beam of X-rays, as shown in fig. (2.2), which propagate through the body Ω along the straight line Ł, up to a well collimated detector R. If we denote as $I(\mathbf{r})$ the intensity of the beam at point $\mathbf{r}$ on the line Ł, then the rate of change of the intensity along the line is given by [103, 79]:

$$\frac{dI(\mathbf{r})}{d\text{Ł}} = -f(\mathbf{r})I(\mathbf{r}) \tag{2.22}$$

where dŁ is a small element along the line. By integrating along the line we get

$$I_R = I_S \exp\left(-\int_{\text{Ł}} f(\mathbf{r})dr\right), \tag{2.23}$$

where I_S is the intensity at the source S and I_R the intensity at the detector R. Therefore if we know both I_S and I_R we obtain the integral of the parameter function $f(\mathbf{r})$ along the line.

By moving the source and detectors alinement around the body as shown in the above figure, we obtain a set of line integrals of $f(\mathbf{r})$ at different angles. The inverse problem in this case becomes the recovery of $f(\mathbf{r})$ from these data. If we consider a direction $\hat{\theta}$ then the lines Ł orthogonal to that direction can be defined by their signed distance s, from the origin, and the angle ϑ between $\hat{\theta}$ and the $y = 0$ axis, as seen in fig.(2.3). The line can then be expressed as Ł : $s\,\hat{\theta} + t\,\hat{\theta}^{\perp}$ with $t \in (-\infty, +\infty)$, where $\hat{\theta} = (\cos\vartheta, \sin\vartheta)$ and $\hat{\theta}^{\perp} = (-\sin\vartheta, \cos\vartheta)$.

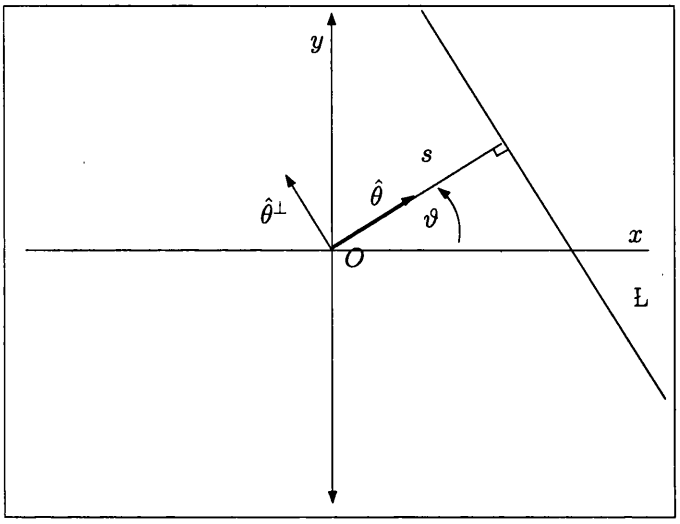

Figure 2.3: Definition of the geometric variables for the Radon transform.

Then the Radon transform [103] of the function f is given by

$$(\mathcal{R}f)(s,\vartheta) = \int_{Ł} \mathbf{f}(s\,\hat{\theta} + t\,\hat{\theta}^{\perp})dt \tag{2.24}$$

The (s,ϑ) plot of the values of the integrals of f, along the corresponding lines Ł, as grey levels, is called the *sinogram* of f.

Let $g(s,\vartheta)$ be a function defined for $s \in (-\infty, +\infty)$ and $\vartheta \in (-\frac{\pi}{2}, \frac{\pi}{2})$, we can introduce the transform:

$$(\mathcal{R}^{*}g)(\mathbf{r}) = \int_{-\frac{\pi}{2}}^{\frac{\pi}{2}} g(\mathbf{r}\cdot\hat{\theta},\vartheta)d\vartheta \tag{2.25}$$

Therefore $\mathcal{R}^{*}$ transforms the data function, represented in the sinogram, into a function of space $\mathbf{r}$.

We noted $\mathcal{R}^{*}$ due to the fact that this operator can be seen as the formal adjoint operator [79]

of $\mathcal{R}$, since:

$$\langle \mathcal{R}f,\ g \rangle_{L^2} = \langle f,\ \mathcal{R}^* g \rangle_{L^2} \tag{2.26}$$

where $\langle f, g \rangle_{L^2} = \int_\omega f(x)g(x)dx$ denotes inner product in L^2.

While the Radon operator $\mathcal{R}$ integrates over all points in line, the backprojection operator $\mathcal{R}^*$ integrates over all lines through a point. If $g(s, \vartheta)$ is the Radon transform of a function $f(\mathbf{r})$ as $g = \mathcal{R}f$ then $\mathcal{R}^*g = \mathcal{R}^*\mathcal{R}f$, which can be used to provide an image of $f = (\mathcal{R}^*\mathcal{R})^{-1}\mathcal{R}^*g$. We note $\mathcal{R}^\dagger := (\mathcal{R}^*\mathcal{R})^{-1}\mathcal{R}^*$ the filtered backprojection operator.

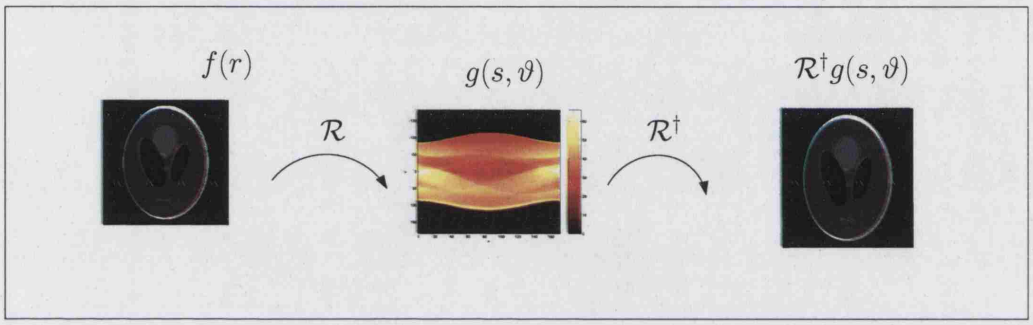

Figure 2.4: Reconstruction of a 2D slice using the Radon transform. On the left the original image, in the middle the sinogram, and on the right the reconstruction with filtered backprojection.

2.6.2 Non-linear case : Optical Tomography

Another application of tomography in medical imaging that has seen increasing interest in the recent years is Optical Tomography. In this case the unknown body Ω is transilluminated by near-infra-red (NIR) light that undergoes absorption and scattering which we measure using the absorption and diffusion coefficients, respectively μ_a and D.

Unlike X-Rays, due to the scattering nature of human tissue for those wavelengths, NIR light doesn't travel in straight lines inside the human body. Therefore a simple inverse operator that given the measurements will produce the optical properties is not known. An established method for the forward and inverse problem in OT, explained in detail by [13, 11, 2], deals with the identification of the distribution of the optical parameters inside the body.

More precisely, the forward mapping is from the two metric spaces, which we usually consider independent [11], of the optical parameters $(\mathbb{X}^{\mu_a}, \mathbb{X}^D)$ to the data space $\mathbb{Y}$ of the measurements

on the surface.

$$\mathcal{K}(D, \mu_a) = \mathbf{g}_{theoretical} \tag{2.27}$$

In practice, a forward model is constructed based on the solution of the diffusion equation (3.24) with boundary conditions (3.37) of Robin type on $\partial\Omega$, using FEM [137, 115]. The domain Ω is divided into N small elements, and values $\mu_{a,i}$ and D_i for the optical properties, are assigned for each of these elements. So that the optical parameters are described as a distribution:

$$\mu_a(\mathbf{r}) = \sum_{i=1}^{N} \mu_{a,i} \ \psi_i(\mathbf{r}) \tag{2.28}$$

$$D(\mathbf{r}) = \sum_{i=1}^{N} D_i \ \psi_i(\mathbf{r}) \tag{2.29}$$

where ψ_i are test functions with local limited support around the element i.

The inverse problem then will become to recover D and μ_a that will produce theoretical data close to the observed measurements $g_{observed} \in \mathbb{Y}$. The method applied is a least squares minimisation problem

$$\Xi(D, \mu_a) = \| \mathbf{g}_{observed} - \mathcal{K}(D, \mu_a) \|_2 \ . \tag{2.30}$$

The result is an image of the distribution of the optical parameters on the elements, as seen in the next fig. (2.5) for Optical Tomography when the light absorption coefficient is plotted in a colour scale.

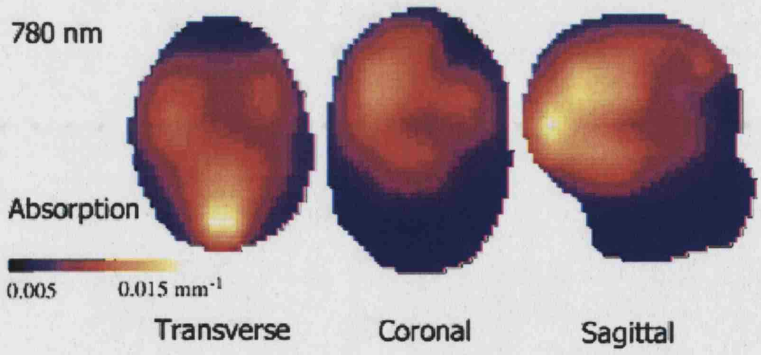

Figure 2.5: Reconstructed image for light absorption in a head model for 3D Optical Tomography. Picture courtesy of Adams Gibson, UCL.

From a mathematical point of view this estimation problem is nonlinear, and ill-posed in the sense that even small errors in the measured data can cause arbitrary large errors in the estimate

of the sought quantities [11, 70].

2.7 Shape based inverse problem

A different approach to the inverse problem is shape reconstruction. This approach identifies regions with piecewise constant coefficients from exterior measurements on a domain. Either an explicit or implicit shape representation scheme can be used. For the explicit scheme a parametric description for shapes is usually necessary. Then the optimisation works in the space of the shape parameters rather than the pixel basis model parameter distributions.

Let's consider the bounded domain $\Omega \subset \mathbb{R}^3$. Assume that Ω is divided into L disjoint regions Ω_ℓ

$$\Omega = \bigcup_{\ell=1}^{L} \Omega_\ell, \tag{2.31}$$

which are bounded by smooth surfaces that have piecewise constant model parameters f_ℓ.

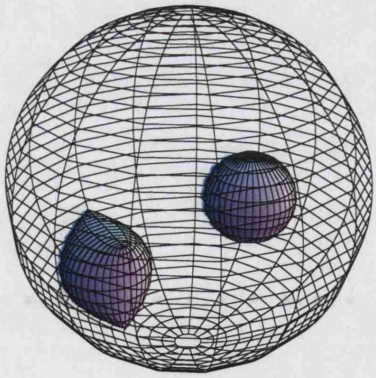

Figure 2.6: The bounded domain Ω (sphere), with two disjoint smooth closed subregions Ω_1 and Ω_2

If we define the characteristic function χ_ℓ to be identically one on Ω_ℓ, and zero elsewhere the

model parameters function takes the form,

$$f(\mathbf{r}) = \begin{cases} f_1\,\chi_1(\mathbf{r}), & \mathbf{r} \in \Omega_1; \\ \vdots & \vdots \\ f_\ell\,\chi_\ell(\mathbf{r}), & \mathbf{r} \in \Omega_\ell; \\ \vdots & \vdots \\ f_L\,\chi_L(\mathbf{r}), & \mathbf{r} \in \Omega_L. \end{cases} \tag{2.32}$$

Let $\Gamma_\ell \subset \Omega$, $\{\ell = 2, \ldots, L\}$ be the smooth boundary between region $\Omega_{\ell-1}$ and the region Ω_ℓ. The outer boundary region Γ_1 is $\partial\Omega$. And also lets assume that there is a parametric representation for the boundaries Γ_ℓ, given by sets of shape parameters $\{\gamma_\ell\}$, for each of the respective boundary Γ_ℓ.

We are looking to reconstruct for the missing internal boundaries Γ_ℓ, which define the areas of discontinuity for the parameters $\{f_\ell\}$. Recovering those boundaries Γ_ℓ, is sufficient for the reconstruction of the full distribution of the model parameters for the domain Ω.

The reconstruction method proposed uses the *a-priori* knowledge of the model properties $\{f_\ell\}$, for the different regions Ω_ℓ inside the domain. The recovery problem can be formulated then as a forward-inverse pair.

The forward problem, is expressed as a mapping from the shape description coefficients $\{\gamma_\ell\}$, $\{\ell = 2, \ldots, L\}$ and the values of $\{f_\ell\}$ to the data (measurements) g on $\partial\Omega$.

The inverse problem will then be the recovery of the boundaries between the several regions of the body by recovering the coefficients $\{\gamma_\ell\}$ that describe those closed surfaces, when the data g and the values $\{f_\ell\}$ are given. That leads to a functional:

$$\Xi(\{\gamma_\ell\}) := \|g - \mathcal{K}(\{\gamma_\ell\})\|^2 \tag{2.33}$$

There are several advantages in this approach. The dimension of the search space for the inverse problem is significantly reduced from the conventional pixel basis parameterisation of the known FEM methods, leading to a less ill-posed inverse problem. In addition, quantitative information of interest usually acquired from additional post-processing by segmentation can now be directly estimated from the data.

2.8 Background on Shape inverse problems

The recovery of unknown boundaries is a problem of great interest in many physical measurement techniques. In this section we will examine some of the techniques from the relevant literature. The main categories of the methods towards shape reconstruction can be divided according to the numerical method used and the parameterisation of the surfaces employed.

In literature, Boundary Elements have been used in numerous applications exploiting the inherent accuracy of the method in evaluating displacements and stresses as well as its robustness in dealing with changes in the geometry of the structure during optimisation.

In [80], an application of the forward solution for the obstacle recovery problem for 3D acoustics and traction free cavities in elastic medium is handled with the use of BEM. The parameterisation suggested for the unknown boundaries is based on a n-ellipsoidal, defined by nine geometric parameters the three centroid coordinates, the three principal axis and three Euler angles for the rotation. In the conclusions of this paper the author claims the importance of finding parameterised representations allowing general shapes for 3D surfaces while keeping the number of design parameters as low as possible.

A different approach can be found in [34, 35],where the parameterisation of the unknown shape is done by using polar coordinates, and therefore only uniformly star-shaped objects can be recovered. That is, objects that have at least one internal point that can be directly connected with a straight line to any of the boundary points. The construction and solution of the BEM system is hereafter done by a wavelet scheme for compression of the system matrices, which according to the authors increases the speed of the solution, but also the numerical error.

Medical imaging applications of the shape inverse problem are also available in the literature mainly in Electrical Impedance Tomography, like [30, 31], where regions of vanishing conductivity embedded in a domain of constant conductivity are recovered using a simple parameterisation of the unknowns in circles in 2D or spheres in 3D.

Several other applications in thermal problems [100, 93, 102], acoustic problems [25] and potential problems [56]are also available in literature.

A recent paper is [60], where the shape of a 3D perfectly conducting object is reconstructed in a cross borehole configuration. A spherical initial guess for the object is optimised, to derive the centre and the comparable radius of the unknown object,[59]. Next Fourier coefficients

are added describing some radial function $R(\vartheta, \varphi)$ on the sphere to refine the shape of the estimation. The functional derivative needed is calculated by the use of reciprocity relations and an adjoint technique described in [9].The development is stopped when there is no more improvement in the shape of the estimation. Numerical results are also shown, but only for an ellipsoid.

A very interesting finite element approach for recovery of piecewise constant coefficients for light absorption and diffusion in Optical Tomography using Continuous Wave (CW) data (see section (3.2)) comes from [72, 71].The proposed method is based on a Fourier series parametric approximation of smooth non intersecting curves, that define the boundaries between regions of piecewise constant coefficients and the employment of a FEM with local mesh perturbations during the procedure of the shape estimation. The existence of a parameterisation technique promises a link between pixel basis methods and the shape inverse that can lead to robust construction of the initial guess about the topology of the sought boundaries. The results are very promising for two dimensional domains. A weakness of the method discussed by the author is the convergence and stability problems that arise in cases where the initial estimates are long way from the true boundaries.

Another approach to the Optical Tomography problem using shape recovery comes from [69]. In this paper inhomogeneities in absorption only are estimated using an ellipsoid shape. A discretisation of a slab domain is done in voxels and therefore the ellipsoid is coarsely defined by the voxels for which their centre lays inside the ellipsoid surface. This method can recover only absorption anomalies that have the shape of an ellipsoid, but can provide useful information about the localisation of the anomaly.

2.9 Level-sets

A quite different approach to the shape inverse problem comes from level-sets, [116, 124], where the shape representation is implicit. A tool that has been effective in dealing with problems that involve moving boundaries and in the last few years has attracted many applications on shape inverse problems, [45, 82, 52, 90, 7].

Some interesting aspects of level sets will become apparent by a brief description of a reconstruction algorithm suggested by Santosa in [45]. One of advantages of this approach is that the level-set representation of the shapes is naturally integrated in the reconstruction scheme.

More precisely, lets assume that we have the generic shape recovery problem :

Find Ω_2 in the equation

$$\mathcal{K}(f) = g. \tag{2.34}$$

where

$$f(\mathbf{r}) = \begin{cases} f_{int} & \text{for } \mathbf{r} \in \Omega_2 \\ f_{ext} & \text{for } \mathbf{r} \notin \Omega_2 \end{cases} \tag{2.35}$$

where, g represents the data and f the model parameters, with value f_{ext} for the background and f_{int} for the obstacle. The operator $\mathcal{K}(\cdot)$ is the forward mapping from the model to the data.

By Ω_2 (a subset of $\Omega \subset \mathbb{R}^3$) we note the obstacle we are interested in recovering. The boundary of Ω_2, Γ_2 can be represented as the zero level of a function $y(\mathbf{r})$ of the three dimensional space,

$$\Gamma_2 = \{\mathbf{r} : y(\mathbf{r}) = 0\}. \tag{2.36}$$

In a level-set approach, a sequence of functions $y_k(\mathbf{r})$ is generated such that:

$$\Gamma_k \rightarrow \Gamma_2. \tag{2.37}$$

with $\Gamma_k = \{\mathbf{r} : y_k(\mathbf{r}) = 0\}$.

If we note $f(\mathbf{r})$ the distribution of the model parameter, the level set description follows:

$$f(\mathbf{r}) = \begin{cases} f_{int} & \text{for } \{\mathbf{r} : y(\mathbf{r}) < 0\} \\ f_{ext} & \text{for } \{\mathbf{r} : y(\mathbf{r}) > 0\} \end{cases} \tag{2.38}$$

So far we have formed the problem so that the final position of the function $y_k(\mathbf{r})$ will describe the boundary of the obstacle Γ_2 as its zero level.

Taking the variation of the equation $y(\mathbf{r}) = 0$ we get:

$$\delta y + \nabla y \cdot \delta \mathbf{r} = 0 \tag{2.39}$$

Creating the inverse problem in a least square sense, we seek for a minimiser for

$$\Xi(f) := \| \mathcal{K}(f) - g \|_2 \tag{2.40}$$

In the Gauss-Newton approach the descent update for f will be given by δf

$$\delta f = [J(f)^T J(f)]^{-1} J(f)^T (g - \mathcal{K}(f)) \tag{2.41}$$

Where $J(f)$ is the Jacobian of $\mathcal{K}(f)$ at f. In order to proceed in that direction we need to explore the dependance of the update δf onto the associated update δy for $y(\mathbf{r})$.

Let's assume that every point $\mathbf{r}$ on Γ_2 moves perpendicular to the surface.

$$\delta \mathbf{r} = a(\mathbf{r}) \frac{\nabla y}{| \nabla y |} \tag{2.42}$$

where $a(\mathbf{r})$ can be the velocity of the surface at $\mathbf{r}$, and $\frac{\nabla y}{|\nabla y|}$ is the unit outward normal.

On the other hand if we assume, without loss of generalisation, that the boundary at point $\mathbf{r}$ moves outwards by $\delta \mathbf{r}$, this movement will change f in the region between $\mathbf{r}$ and $\mathbf{r} + \delta \mathbf{r}$ that will become f_{int}. Therefore for those points $\delta f = f_{int} - f_{ext}$.

We consider now the inner product of δf with a test function $\psi(\mathbf{r})$. We have:

$$< \delta f, \psi >= \int_{\mathbb{R}^3} \delta f(\mathbf{r}) \psi(\mathbf{r}) d\mathbf{r} = \int_{\Omega_2 \bigcap \Omega_2'} \delta f(\mathbf{r}) \psi(\mathbf{r}) d\mathbf{r} \tag{2.43}$$

Now the value of $\delta f(\mathbf{r})$ is $\pm (f_{int} - f_{ext})$. We notice also that the increment volume over which f varies at point $\mathbf{r}$ is given by $\left(\delta \mathbf{r} \cdot \frac{\nabla y}{|\nabla y|} ds(\mathbf{r}) \right)$ where $ds(\mathbf{r})$ is the incremental surface area on Γ_2. Thus the inner product above, since $\delta \mathbf{r}$ is infinitesimal, can be expressed as an integration over all the boundary Γ_2 which leads to :

$$< \delta f, \psi >= \int_{\Gamma_2} (f_{int} - f_{ext}) \, \delta \mathbf{r} \cdot \frac{\nabla y}{| \nabla y |} \psi(\mathbf{r}) ds(\mathbf{r}) \tag{2.44}$$

From (2.43) and (2.44) we get a new definition for δf using $\delta \mathbf{r}$

$$\delta f = (f_{int} - f_{ext}) \frac{\nabla y}{| \nabla y |} \cdot \delta \mathbf{r} \, |_{\mathbf{r} \in \Gamma_2} \, . \tag{2.45}$$

From (2.42)

$$\delta f = (f_{int} - f_{ext})\ a(\mathbf{r})\ |_{\mathbf{r}\in\Gamma_2}\ . \tag{2.46}$$

Rearranging,

$$a(\mathbf{r}) = \frac{\delta f}{(f_{int} - f_{ext})}\ . \tag{2.47}$$

From (2.39) and (2.47) we get:

$$\delta y(\mathbf{r}) = -\frac{\delta f}{f_{int} - f_{ext}}\ |\ \nabla y_k(\mathbf{r})\ | \tag{2.48}$$

Having established the relationship between the update for $y(\mathbf{r})$ and the update for $f(\mathbf{r})$ we can now give the full algorithm of the level-set optimisation method.

- Choose $y_0(\mathbf{r})$: set $k = 0$.
- Compute associated f : If $\Xi(f) > \tau$, where τ some tolerance limit, do :
  1. Compute : $\delta f = [J(f)^T J(f)]^{-1} \cdot J(f)^T (g - \mathcal{K}(f))$
  2. Then, compute : $\delta y(\mathbf{r}) = -\frac{\delta f'}{f_{int} - f_{ext}}\ |\ \nabla y_k(\mathbf{r})\ |$
  3. Set $k = k + 1$, update $y_{k+1}(\mathbf{r}) = y_k(\mathbf{r}) + \delta y(\mathbf{r})$

A very interesting feature of the level set representation is that the topological constraint to simple connected surfaces is no longer necessary. Roughly speaking, there is no need for the knowledge of the number of obstacles that we reconstructing, which was a prerequisite in the traditional shape optimisation techniques. Nevertheless, in problems where the topology is known and should be maintained, e.g. reconstructing for the shape of a brain, artificial constraints have to be introduced in the level-set representation in order for the topology to remain unchanged.

2.10 Summary

A general background on inversion theory with some important definitions and the most common tools used, was given in this chapter. We tried to describe briefly the notions useful to understand the solution of a forward-inverse problem pair using a least squares minimisation. Also we presented an introduction of the shape based inverse problem and its applications on tomography.

All this work is connected with the next chapters, where a description of the physical model used in OT followed by a numerical solution method with Boundary Elements will be constructing the forward problem. Next, a parametrisation for shapes using spherical harmonics will provide the necessary shape description in chapter 6. Finally, we will return to the non-linear inverse problem involved, in chapter 8, to explain the shape based approach using the spherical harmonics shape description.

Chapter 3

The Physical Model in Optical Tomography

3.1 Introduction

In this chapter we will examine the mathematical terms that model the physical reality underlaying Optical Tomography OT. Since we decided to use OT as a test bed for the reconstruction techniques proposed in this thesis, the presentation of the functionalities and mathematical terms of OT is appropriate at this stage.

Biological tissue is visually opaque. Photons travelling within are mainly scattered rather than absorbed. Indeed, someone holding a flashlight up his to or her hand will notice that some of the light is transmitted through the hand even though it scatters. Light travels through tissue in a process similar to heat diffusion.

According to [11], Optical Tomography refers to the use of low-energy visible or near infrared light, in the wavelength of $\sim 700 - 1000nm$, to probe highly scattering media, in order to derive qualitative or quantitative images of the optical properties of these media.

Visible and near infrared light interacts with biological tissue predominantly by absorption and elastic scattering. There are several physiologically interesting molecules which have characteristic absorption spectra at these wavelengths. In particular, the spectra of oxy-haemoglobin (HbO) and deoxy-haemoglobin (Hb) differ markedly, and so do the oxygenation-dependent spectra of cytochrome oxidase. Haemoglobin provides an indicator of blood volume and oxygenation, whereas the cytochrome enzymes indicate tissue oxygenation [8].

The different absorption spectra of HbO and HHb are routinely exploited in physiological monitoring techniques such as pulse oximetry and near infrared spectroscopy (NIRS). Diffuse

optical tomography techniques aim to process this information further and produce spatially resolved images. These images may display the specific absorption and scattering properties of the tissue, or physiological parameters such as blood volume and oxygenation.

Optical tomography is a popular subject for many research teams around the world [2, 8, 53, 54, 72, 89] and has attracted large attention due to its safe non-ionising measurements and the ability to generate full three-dimensional (3D) images of interesting physiological parameters from measurements taken from sources and detectors widely spaced over the surface of the object.

3.2 Experimental setup

In the experimental setup used for optical tomography we consider S optic fibers placed on the source positions $p_s \in \partial\Omega, (s = 1, \ldots, S)$ on the boundary of the body Ω and M measurement positions $m_d \in \partial\Omega, (d = 1, \ldots, M)$, as displayed in figure (3.1).

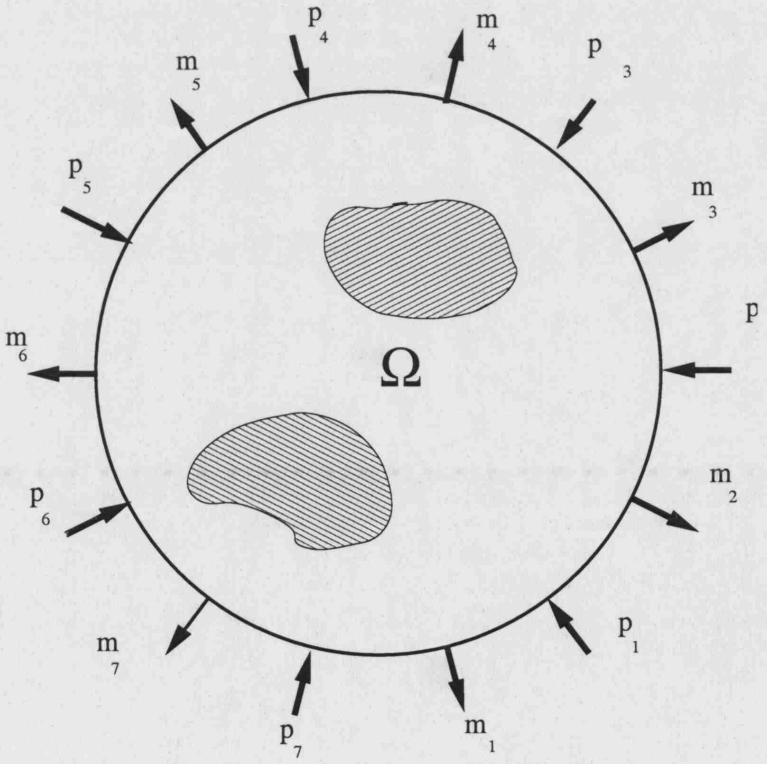

Figure 3.1: The Optical Tomography experimental setup in the two dimensional space

There are three main types of measurements that can be acquired in an OT system; Continuous Wave (CW), Frequency Domain (FD) and Time Resolved (TR) or Time Domain. The main

idea behind those systems is similar: Light from the laser is guided through the optic fibers to one of the sources p_s and into the body. Then, measurements of the transmitted through the body light are collected at all the measurement positions m_d, using the optic fibers and light sensitive detectors. The process is repeated for each of the S sources.

The CW systems use steady state light source and only the intensity of the emerging light can be measured. Even though this is the simplest and easiest method to implement, the information from measurements of just light intensity are insufficient [11] to distinguish between scatter and absorption and the unambiguous reconstruction of both is impossible.

In TR systems the input is an ultra short (duration $\sim$ $10ps$) laser pulse and the measured quantity the temporal distribution of the transmitted photons through the tissue. The temporal distribution is in the form of a Temporal Point Spread Function (TPSF). The number of photons measured can represent the amplitude of the wave, while Fourier Transform of the pulse can produce the frequency domain components of the signal. A TPSF contains a variety of information and is the optimum measurement to characterise a system, but there is a high cost and mechanical complexity for the time resolved instrumentation.

Finally, in FD systems the light used is created from a sinusoidally modulated laser source (Frequency $\sim$ 10 MHz - 1 GHz),and the measured quantities are the modulation amplitude and the phase shift of the transmitted light. In practice all those systems benefit significantly from the use of many source-detectors pairs and many optical wavelengths. In this thesis we focus on frequency domain systems, but the results can also be applied to time-resolved and continuous wave methods.

The dominance of high scattering of light into tissue makes impossible the direct reconstruction of the image from those measurements. For example, the use of the Radon Transform, see section (2.6.1), is insufficient since light does not travel in straight lines though the tissue like X-rays. In order to image through the diffusive media, we need to know the effect that the structure inside the media will have to the measurements on the surface.

In the next section we will examine the so called forward problem in Optical Tomography, the theoretical model for the behaviour of light through the diffusive media. We will try to develop a quantitative model that describes the distribution of light in a biological medium, knowing the optical properties of the tissue.

3.3 The Radiative Transfer Equation (RTE)

Light propagating through biological tissue follows the Radiative Transfer (or Boltzmann transport) equation. Assuming that $\Omega \subset \mathbb{R}^3$ and denoting $\mathbf{r} \in \Omega$ the position vector and $t \in \mathbb{R}$ the time variable, RTE will have the form:

$$\left(\frac{1}{c}\frac{\partial}{\partial t} + \hat{\mathbf{s}} \cdot \nabla + \mu_a + \mu_s\right) \phi(\mathbf{r}, t, \hat{\mathbf{s}}) = \mu_s \int_{S^2} \phi(\mathbf{r}, t, \hat{\mathbf{s}}') \, \Theta(\hat{\mathbf{s}}, \hat{\mathbf{s}}') \, d\hat{\mathbf{s}}' + q(\mathbf{r}, t, \hat{\mathbf{s}}), \quad (3.1)$$

where μ_a is the absorption and μ_s the scattering coefficients with units in mm^{-1}, the scalar $\phi(\mathbf{r}, t, \hat{\mathbf{s}})$ is the energy radiance, the number of photons per unit volume at position $\mathbf{r}$ at time t with velocity in direction $\hat{\mathbf{s}}$, c the speed of light in the medium, $\hat{\mathbf{s}} \in S^2$ a unit vector and $q(\mathbf{r}, t, \hat{\mathbf{s}})$ the source term representing the number of photons per unit volume per unit time at the source position $\mathbf{r}$ at time t with velocity c in direction $\hat{\mathbf{s}}$.

$\Theta(\hat{\mathbf{s}}, \hat{\mathbf{s}}')$ represents the scattering phase function, that has the property,

$$\int_{S^2} \Theta(\hat{\mathbf{s}}, \hat{\mathbf{s}}') d\hat{\mathbf{s}}' = 1, \quad (3.2)$$

and describes the probability density of scattering from direction $\hat{\mathbf{s}}$ to direction $\hat{\mathbf{s}}'$. For an isotropic material which is rotationally invariant $\Theta(\hat{\mathbf{s}}, \hat{\mathbf{s}}') = \Theta(\hat{\mathbf{s}} \cdot \hat{\mathbf{s}}')$ which depends only on the cosine of the scattering angle between $\hat{\mathbf{s}}$ and $\hat{\mathbf{s}}'$.

The RTE (3.1) ignores the wave nature of light: it treats photons as energetic particles that undergo elastic collisions until they are absorbed or escape the domain Ω. The physical basis of the RTE comes from the change of energy radiance $\phi(\mathbf{r}, t, \hat{\mathbf{s}})$ due to the energy flow. Loss of energy is due to absorption and scattering and gain is due to the radiation sources and scattering. RTE is widely accepted as a valid model for the propagation of near infrared light in tissue.

However, due to difficulties to compute numerical solutions for the RTE in complex geometries and for arbitrary parameter distributions, most of the current approaches in OT use the diffusion approximation (DA) to model the light propagation inside diffusive medium.

3.4 Derived Quantities in Transport Theory

We consider some important quantities in transport theory, namely: specific intensity, photon density, energy and flux density.

Considering, a flow of wave energy at a point $\mathbf{r}$, the frequency, phase and amplitude of that wave undergo random variations in time, and therefore the magnitude and direction of its power flux density vector vary continuously in time [62].

For a given direction defined by a unit vector $\hat{\mathbf{s}}$, the average power flux density, that is number of photons per unit volume within a solid angle in this direction at point $\mathbf{r}$ at time t, is noted $\phi(\mathbf{r}, \hat{\mathbf{s}}, t)$ and its called *specific intensity* or *energy radiance* and its unit is $Wm^{-2}sr^{-1}$.

The photon density then would be given by integrating the specific intensity in all directions on the S^2 sphere.

$$\Phi(\mathbf{r}, t) = \int_{4\pi} \phi(\mathbf{r}, t, \hat{\mathbf{s}}) d\hat{\mathbf{s}} \tag{3.3}$$

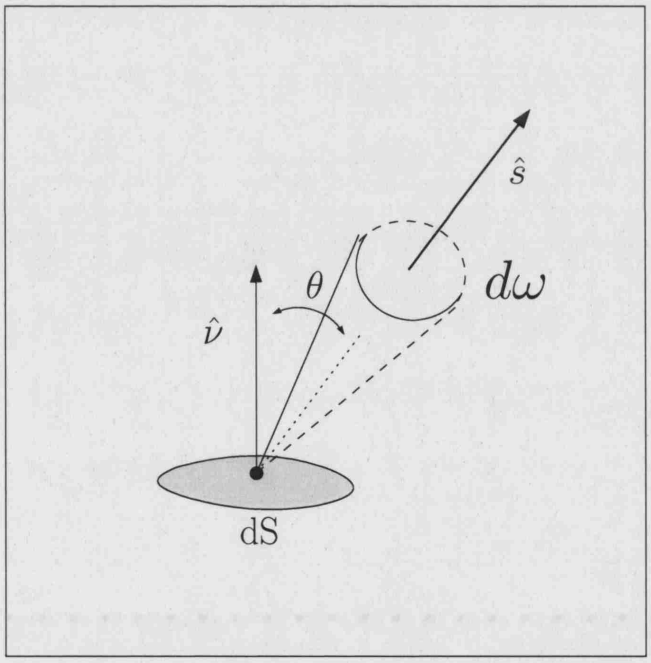

Figure 3.2: Specific Intensity, $\phi(\mathbf{r}, \hat{\mathbf{s}}, t)$

The energy leaving the area dS in time dt within a solid angle $d\omega$ through the elementary area dS oriented in a direction of the unit vector $\hat{\mathbf{s}}$ is, (see fig.(3.2)),

$$dP = \phi(\mathbf{r}, \hat{\mathbf{s}}, t)\, dS\, d\omega\, dt. \tag{3.4}$$

Let us consider the total flux passing through the small area dS. The forward flux density can

be defined by integrating (3.4) over $\hat{\mathbf{s}}$, when $\hat{\mathbf{s}} \cdot \hat{\nu} > 0$:

$$J_+(\mathbf{r}, t, \hat{\nu}) = \int_{\hat{\mathbf{s}}\cdot\hat{\nu} > 0} \phi(\mathbf{r}, t, \hat{\mathbf{s}})\, \hat{\mathbf{s}} \cdot \hat{\nu}\, d\hat{\mathbf{s}} \tag{3.5}$$

While, the backward flux density J_- for the flux flowing through dS in the backward direction $\hat{\mathbf{s}}$, with $\hat{\mathbf{s}} \cdot \hat{\nu} < 0$ is :

$$J_-(\mathbf{r}, t, \hat{\nu}) = \int_{\hat{\mathbf{s}}\cdot\hat{\nu} < 0} \phi(\mathbf{r}, t, \hat{\mathbf{s}})\, \hat{\mathbf{s}} \cdot (-\hat{\nu})\, d\hat{\mathbf{s}} \tag{3.6}$$

The total flux density in the direction $\hat{\nu}$ can then be expressed as:

$$\mathbf{J}(\mathbf{r}, t) \cdot \hat{\nu} = J_+(\mathbf{r}, t) - J_-(\mathbf{r}, t) \tag{3.7}$$

Where $\mathbf{J}(\mathbf{r})$ represents the flux density vector,

$$\mathbf{J}(\mathbf{r}, t) = \int_{4\pi} \phi(\mathbf{r}, t, \hat{\mathbf{s}})\, \hat{\mathbf{s}}\, d\hat{\mathbf{s}}. \tag{3.8}$$

Where the integration is performed over the sphere S^2.

3.5 The Diffusion Approximation to RTE

In the derivation of the diffusion approximation we use the P_N approximation approach, where the quantities $\phi(\mathbf{r}, t, \hat{\mathbf{s}})$ and $q(\mathbf{r}, t, \hat{\mathbf{s}})$ from equation (3.1) are expanded into series of spherical harmonics

$$\phi(\mathbf{r}, t, \hat{\mathbf{s}}) = \sum_{l=0}^{\infty} \sum_{m=-l}^{m=l} \left(\frac{2l+1}{4\pi}\right)^{\frac{1}{2}} \phi_m^l(\mathbf{r}, t) Y_m^l(\hat{\mathbf{s}}) \tag{3.9}$$

and

$$q(\mathbf{r}, t, \hat{\mathbf{s}}) = \sum_{l=0}^{\infty} \sum_{m=-l}^{m=l} \left(\frac{2l+1}{4\pi}\right)^{\frac{1}{2}} q_m^l(\mathbf{r}, t) Y_m^l(\hat{\mathbf{s}}). \tag{3.10}$$

Assuming the P_1 approximation, where $\phi_m^l, q_m^l = 0$ for $|l| > 1$ and through some computations, see for example [11], we obtain the approximation:

$$\phi(\mathbf{r}, t, \hat{\mathbf{s}}) \approx \frac{1}{4\pi}\Phi(\mathbf{r}, t) + \frac{3}{4\pi}\hat{\mathbf{s}} \cdot \mathbf{J}(\mathbf{r}, t) \tag{3.11}$$

where Φ is the photon density from (3.3) and $\mathbf{J}$ the photon current defined in (3.8). Similarly, for the source terms:

$$q(\mathbf{r}, t, \hat{\mathbf{s}}) \approx \frac{1}{4\pi} q_0(\mathbf{r}, t) + \frac{3}{4\pi} \hat{\mathbf{s}} \cdot q_1(\mathbf{r}, t) \tag{3.12}$$

where the quantity

$$q_0(\mathbf{r}, t) = \int_{4\pi} q(\mathbf{r}, t, \hat{\mathbf{s}}) d\hat{\mathbf{s}} \tag{3.13}$$

is the isotropic component of the source term and

$$q_1(\mathbf{r}, t) = \int_{4\pi} q(\mathbf{r}, t, \hat{\mathbf{s}})\, \hat{\mathbf{s}}\, d\hat{\mathbf{s}} \tag{3.14}$$

is the first angular moment of the source term. Inserting (3.12) and (3.11) into (3.1) we arrive at the pair of equations

$$\left(\frac{1}{c} \frac{\partial}{\partial t} + \mu_a(\mathbf{r}) \right) \Phi(\mathbf{r}, t) + \nabla \cdot J(\mathbf{r}, t) = q_0(\mathbf{r}, t) \tag{3.15}$$

and

$$\left(\frac{1}{c} \frac{\partial}{\partial t} + \mu_a(\mathbf{r}) + \mu_s'(\mathbf{r}) \right) J(\mathbf{r}, t) + \frac{1}{3} \nabla \Phi(\mathbf{r}, t) = q_1(\mathbf{r}, t) \tag{3.16}$$

where

$$\mu_s' = (1 - \Theta_1)\mu_s \tag{3.17}$$

is the reduced scattering coefficient and Θ_1 is the mean cosine of the scattering phase function, i.e.

$$\Theta_1 = \int_{4\pi} \hat{\mathbf{s}} \cdot \hat{\mathbf{s}}' \Theta(\hat{\mathbf{s}} \cdot \hat{\mathbf{s}}') d\hat{\mathbf{s}}'. \tag{3.18}$$

The diffusion approximation results from equations (3.15), (3.16) and the assumptions

$$q_1(\mathbf{r}, t) = 0 \tag{3.19}$$

and

$$\frac{\partial \mathbf{J}(\mathbf{r}, t)}{\partial t} = 0 \tag{3.20}$$

with these assumptions equation (3.16) is simplified into Fick's law

$$\mathbf{J}(\mathbf{r}, t) = -D \nabla \Phi(\mathbf{r}, t), \tag{3.21}$$

where

$$D = \frac{1}{3(\mu_a + \mu_s')} \tag{3.22}$$

is the diffusion coefficient of the medium. By inserting (3.21) into (3.15) we arrive at the diffusion approximation in time domain

$$-\nabla \cdot D(\mathbf{r})\nabla\Phi(\mathbf{r},t) + \mu_a(\mathbf{r})\Phi(\mathbf{r},t) + \frac{1}{c}\frac{\partial\Phi(\mathbf{r},t)}{\partial t} = q_0(\mathbf{r},t), \mathbf{r} \in \Omega \tag{3.23}$$

or in frequency domain, obtained by Fourier Transform

$$-\nabla \cdot D(\mathbf{r})\nabla\hat{\Phi}(\mathbf{r},\omega) + \mu_a(\mathbf{r})\hat{\Phi}(\mathbf{r},\omega) + \frac{i\omega}{c}\hat{\Phi}(\mathbf{r},\omega) = \hat{q}_0(\mathbf{r},\omega) \tag{3.24}$$

Examining the assumptions for the diffusion approximation we get (3.19) meaning that any anisotropic component of the source term $q(\mathbf{r},t,\hat{\mathbf{s}})$ is neglected and (3.20) implying that the rate of change of photon current is zero which is erroneous in the time-dependent case, but is usually justified by specifying the condition $\mu_a \ll \mu_s'$. To clear this up, let assume that $\mathbf{J}$ is dominated by an exponential decaying term with time constant $c\lambda$. Then (3.21) becomes:

$$(1 - 3\,D\,\lambda)\,\mathbf{J}(\mathbf{r},t) = -D\nabla\Phi(\mathbf{r},t), \tag{3.25}$$

leading to

$$\hat{D} = \frac{D}{(1 - 3\,D\,\lambda)} = \frac{1}{3(\mu_a + \mu_s' - \lambda)} \tag{3.26}$$

instead of (3.22). [131] has argued that in this case $\lambda = \mu_a$ which is consistent with the long time limit observation of an exponentially decaying solution and leads to,

$$\hat{D} = \frac{1}{\mu_s'} \tag{3.27}$$

which when compared with (3.22) shows the necessity for the condition $\mu_a \ll \mu_s'$.

The near-infrared spectral window of biological tissue lies between the intense visible absorption bands of hemoglobin and the near-infrared absorption band of water. In this window the reduced scattering coefficient is often 10 to 1000 times greater than the absorption coefficient [2]. This justifies the necessary condition. In general the diffusion approximation (3.23) seems to produce correct predictions of boundary measurement, following the experimental results

and Monte Carlo simulations [115]. So we can regard diffusion equation as a valid model for calculating measurement signals.

3.6 Helmholtz equation

If we consider a homogenous domain where the optical parameters do not depend on $\mathbf{r}$, the diffusion equation (3.24) takes the form:

$$-D \cdot \nabla^2 \Phi(\mathbf{r}, \omega) + \mu_a \Phi(\mathbf{r}, \omega) + \frac{i\omega}{c} \Phi(\mathbf{r}, \omega) = q_0(\mathbf{r}, \omega) \tag{3.28}$$

If we define the wave number:

$$k = \left(\frac{\mu_a + \frac{i\omega}{c}}{D} \right)^{\frac{1}{2}} \tag{3.29}$$

we arrive at the equivalent Helmholtz equation

$$\nabla^2 \Phi(\mathbf{r}, \omega) - k^2 \Phi(\mathbf{r}, \omega) = -\frac{q_0(\mathbf{r}, \omega)}{D} \tag{3.30}$$

The solution to (3.30) when the right hand side is a δ-function, defines the Green's function in an infinite medium. This would be a spherical wave.

$$G(\mathbf{r}, \mathbf{r_s}, \omega) = \frac{1}{4\pi |\mathbf{r} - \mathbf{r_s}|} e^{-k|\mathbf{r}-\mathbf{r_s}|} \tag{3.31}$$

where $|\mathbf{r} - \mathbf{r_s}|$ represents the distance between a point $\mathbf{r}$ of the body and a source at position $\mathbf{r_s}$.

3.7 Boundary conditions

The solution of diffusion or Helmholtz equations require the application of appropriate boundary conditions. The physical assumption is that no photons travel in an inward direction at the boundary, except for source terms,

$$\phi(\mathbf{m}, t, \hat{\mathbf{s}}) = 0 \qquad \text{for} \qquad \hat{\mathbf{s}} \cdot \hat{\nu} < 0, \tag{3.32}$$

where $\hat{\nu}$ is the outward normal and point $\mathbf{m} \in \partial\Omega$. For the diffusion equation this condition is transformed to the total inward directed current being zero.

$$\int_{\hat{\mathbf{s}}\cdot\hat{\nu}<0} \phi(\mathbf{m}, t, \hat{\mathbf{s}})\, \hat{\mathbf{s}} \cdot \hat{\nu}\, d\hat{\mathbf{s}} = 0. \tag{3.33}$$

which leads, (see [62]), to the Robin Boundary condition:

$$\Phi(\mathbf{m}) + 2D(\mathbf{m})\frac{\partial\Phi(\mathbf{m})}{\partial\hat{\nu}} = 0 \tag{3.34}$$

This represents the physical model of a non scattering medium surrounding Ω, assuming no diffusive reflection at $\partial\Omega$, [115]. To incorporate a mismatch between refractive indices within Ω and the surrounding medium, equation (3.33) becomes

$$\int_{\hat{\mathbf{s}}\cdot\hat{\nu}<0} \phi(\mathbf{m}, t, \hat{\mathbf{s}})\, \hat{\mathbf{s}} \cdot \hat{\nu}\, d\hat{\mathbf{s}} = \int_{\hat{\mathbf{s}}\cdot\hat{\nu}>0} R(\hat{\mathbf{s}})\phi(\mathbf{m}, t, \hat{\mathbf{s}})\, \hat{\mathbf{s}} \cdot \hat{\nu}\, d\hat{\mathbf{s}}. \tag{3.35}$$

where R is a directional varying reflection parameter. The modified Robin condition then takes the form:

$$\Phi(\mathbf{m}) + 2D(\mathbf{m})\frac{\partial\Phi(\mathbf{m})}{\partial\hat{\nu}} = R\left[\Phi(\mathbf{m}) + 2D(\mathbf{m})\frac{\partial\Phi(\mathbf{m})}{\partial\hat{\nu}}\right]. \tag{3.36}$$

With a bit of rearrangement:

$$\Phi(\mathbf{m}) + 2\alpha D(\mathbf{m})\frac{\partial\Phi(\mathbf{m})}{\partial\hat{\nu}} = 0, \tag{3.37}$$

where $\alpha = \frac{(1+R)}{(1-R)}$, [11, 115].

3.8 Sources

When modelling the light source incident at a point on the boundary $\partial\Omega$, we can distinguish two cases [115].

A collimated source is represented by a diffusive point source and the last term of equation (3.24) takes the form:

$$q_0(\mathbf{r}, \omega) = \delta(\mathbf{r} - \mathbf{r_s}) \tag{3.38}$$

where $\mathbf{r_s}$ is located at the depth of one scattering length $(1/\mu_s')$ below the tissue surface, [32]. This would produce accurate results at distances from the source larger than the mean free path,

but breaks down close to the source.

A different approach is that of a diffusive source on the surface where the initially condition is represented as an inward directed photon current distributed over a boundary segment. The diffusive source can be incorporated directly into the boundary conditions.

$$\Phi(\mathbf{m}) + 2\alpha D(\mathbf{m})\frac{\partial\Phi(\mathbf{m})}{\partial\hat{\nu}} = -4A_s w(\mathbf{m}), \tag{3.39}$$

Where $\mathbf{m}$ belongs to the source boundary segment, A_s is the strength of the source current and $w(\mathbf{m})$ is a weighting function.

3.9 Summary

Based on the physical model that uses the diffusion approximation to simulate the transport of light through a scattering medium, which was described earlier we can built a forward mapping for OT inverse problems. In the actual model that we use there are some assumptions that we should remember. First of all the assumption that $\mu_a \ll \mu_s'$ which is generally true for the tissues involved in the human head, apart from the cerebrospinal fluid, a thin fluid layer that surrounds the brain where the scattering is almost zero. [10, 41, 104] indicates that the diffusion approximation is not the valid model for the transportation of light through this region and a radiosity-diffusion method should be used instead. Up to this point in our work we haven't found a fast and reliable technique for the implementation of such a model in a complicated 3D geometry and therefore we will deal with that in our future work.

Chapter 4

Boundary Element Method

4.1 Introduction

The world around us consists of physical phenomena that science is called to model and analyse. It is often that those phenomena are expressed on complex structures and characterised by a continuum behaviour. Human conception was often unable to comprehend those phenomena in one operation. Thus the process of subdividing whole systems into individual components or *elements*, whose behaviour is well understood, and then rebuilding the original system from those components to study its behaviour is a usual tactic followed by scientists.

Modelling physical phenomena found fertile soil with the advent of computers. The discrete nature of computer operations ease the solution of discrete problems, even when the number of calculations included is very large. Thus the computer's finite capacity complicated the manipulation of problems in continuum. Continuity, as part of mathematical fiction, is impossible to achieve by computers and approximation techniques had to be involved.

Various methods of discretisation have been proposed by engineers and mathematicians to approximate the true continuum solution by a number of discrete variable parameters. The intention in those techniques is the approximation of a set of partial differential equations, governing the behaviour of a system by a set of algebraic equations as closely as desired to the real one. The numerical techniques that are widely used by scientists include FEM, Finite Differences and BEM [73].

In the Optical Tomography field there are many cases where analytic solutions using the Green's functions have been used for the modelling of the diffusion equation [91, 107, 2]. Un-

fortunately, in most analytic approaches, solutions only exist for simple homogeneous geometries. The traditional approach to deal with complicated geometries is that of Finite Elements [2, 11, 13, 70]. The main feature of this method lays in the discretisation of the domain into a finite number of small volume elements.

The complicated geometry of the internal human structures and the lack of an reliable method to create a successful discrete approximation of the 3D geometries involved, draw our attention into the Boundary Element Method, [16, 17, 20, 51, 67, 81, 83], where a boundary integral equation is solved numerically by dividing the surface rather than the volume into elements in each of which a simple approximation applies. BEM has been used in the past for the forward problem in Electrical Impedance Tomography [28, 31, 50] and there have been some similar approaches recently in the field of Optical Tomography [105, 121, 122, 120], with sufficiently good results.

4.2 Formulation of the problem

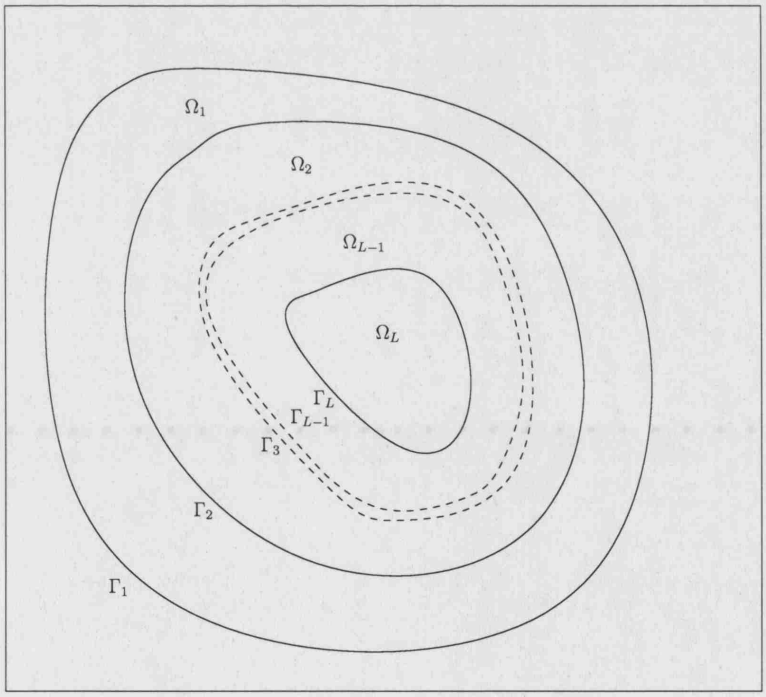

Figure 4.1: The domain Ω, divided into disjoint regions Ω_i

The problem of Optical Tomography in highly diffusive body Ω can be modelled by the use of the diffusion equation in the frequency domain form (3.24) with Robin boundary conditions

(3.37).

For the scope of our model, we assume that the body Ω is divided in L nested subregions Ω_ℓ, $(1 \leq \ell \leq L)$ shown in the following graph (4.1). Each region is defined by the smooth boundaries Γ_ℓ,$(1 \leq \ell \leq L)$ and are characterised by constant material parameters, diffusion D_ℓ and absorption $\mu_{a,\ell}$ coefficients for the respective subdomain Ω_ℓ, $\ell = 1, \ldots, L$. The outer boundary Γ_1 of the region Ω_1 is $\partial\Omega$. In a homogeneous medium since the subdomains have constant optical parameters the diffusion equation is equivalent to the Helmholtz equation. If we denote Φ_ℓ the restriction of Φ in the subdomain Ω_ℓ,we get:

$$\nabla^2\Phi_\ell(\mathbf{r}) - k_\ell^2\Phi_\ell(\mathbf{r}) = -q_\ell(\mathbf{r}) \text{ in } \Omega_\ell \tag{4.1}$$

Where the source term $q_\ell = q_1\delta_{i,1}$ is non-zero only for $i = 1$, and:

$$k_\ell = \left(\frac{\mu_{a,\ell} + \frac{i\omega}{c}}{D_\ell}\right)^{\frac{1}{2}}. \tag{4.2}$$

The three-dimensional fundamental solutions G_ℓ, (Green's functions) of the Diffusion equation in an infinite medium are simply spherical waves and have the form (3.31) which we reproduce here:

$$G_\ell(\mathbf{r}, \mathbf{r_s}, \omega) = \frac{1}{4\pi|\mathbf{r} - \mathbf{r_s}|}e^{-k_\ell|\mathbf{r}-\mathbf{r_s}|} \tag{4.3}$$

where $|\mathbf{r} - \mathbf{r_s}|$ represents the distance between a point $\mathbf{r}$ of the body and a source at position $\mathbf{r_s}$. The normal derivative of the fundamental solution, where $\hat{\nu}$ notes the exterior normal vector on the surface Γ_ℓ, can then be written:

$$\hat{\nu} \cdot \nabla G = \hat{\nu} \cdot \frac{\mathbf{r} - \mathbf{r_s}}{|\mathbf{r} - \mathbf{r_s}|}\left(\frac{-1}{4\pi|\mathbf{r} - \mathbf{r_s}|^2} - \frac{k_\ell}{4\pi|\mathbf{r} - \mathbf{r_s}|}\right)e^{-k_\ell|\mathbf{r}-\mathbf{r_s}|} \tag{4.4}$$

In section (3.6) we mention that the Green's functions in each subdomain Ω_ℓ arise as solutions of the equations

$$\nabla^2 G_\ell(\mathbf{r}, \mathbf{r_s}) - k_\ell^2 G_\ell(\mathbf{r}, \mathbf{r_s}) = -\delta(\mathbf{r} - \mathbf{r_s}) \tag{4.5}$$

with the asymptotic condition

$$G_\ell(\mathbf{r}, \mathbf{r_s})|_{\mathbf{r}\to\infty} = 0 \tag{4.6}$$

Following the graph (4.1), Γ_ℓ will be the interface between subdomain $\Omega_{\ell-1}$ and Ω_ℓ, where

$1 \leq \ell \leq L$. There are certain interface conditions that should be satisfied

$$\Phi_{\ell-1}|_{\Gamma_\ell} = \Phi_\ell|_{\Gamma_\ell} = I_\ell, \tag{4.7}$$

$$-D_{\ell-1}\,\partial_{\ell-1}\Phi_{\ell-1}|_{\Gamma_\ell} = D_\ell\,\partial_\ell\Phi_\ell|_{\Gamma_\ell} = J_\ell, \quad 1 \leq \ell \leq L \tag{4.8}$$

Where we used the abbreviated notation

$$\partial_\ell = \hat{\nu}\cdot\nabla \tag{4.9}$$

for the normal derivatives. For the outer surface Γ_1 we should satisfy the Robin boundary conditions.

$$I_1 + 2\alpha J_1 = 0 \tag{4.10}$$

4.3 Green's second theorem

The essence of the Boundary Element formulation is to drop the dimensionality of the problem by one, i.e. to transform the variables from volume variables to surface ones. This can be simply done by using the second Green's theorem which for three dimensions can be stated as:

$$\int_{\partial\Omega}(U\frac{\partial V}{\partial\hat{\nu}} - V\frac{\partial U}{\partial\hat{\nu}})\;dS = \int_\Omega U\nabla^2 V - V\nabla^2 U\;dP \tag{4.11}$$

4.4 Integral representation

From equations (4.5) and (4.1), by multiplying (4.5) with $\Phi(\mathbf{r})$ and (4.1) with $G_\ell(\mathbf{r},\mathbf{r_s})$, and subtracting we get:

$$\Phi_\ell(\mathbf{r})\nabla^2 G_\ell(\mathbf{r},\mathbf{r_s}) - G_\ell(\mathbf{r},\mathbf{r_s})\nabla^2\Phi_\ell(\mathbf{r}) = -\delta(\mathbf{r}-\mathbf{r_s})\Phi_\ell(\mathbf{r}) + q_\ell(\mathbf{r})G_\ell(\mathbf{r},\mathbf{r_s}) \tag{4.12}$$

Integrating both parts of the equation over the whole subregion Ω_ℓ in respect to $\mathbf{r_s}$, and applying the second Green's Theorem we get the following *integral representation formula*:

$$\Phi_\ell(\mathbf{r}) = \left(\int_{\Gamma_\ell} - \int_{\Gamma_{\ell+1}}\right)\left(G_\ell(\mathbf{r},\mathbf{r_s})\partial_\ell\Phi_\ell(\mathbf{r_s}) - \Phi_\ell(\mathbf{r_s})\partial_\ell G_\ell(\mathbf{r},\mathbf{r_s})\right)dS(\mathbf{r_s}) + Q_\ell(\mathbf{r}), \tag{4.13}$$

where $\Gamma_{L+1} = \emptyset$ and the source term Q_ℓ is:

$$Q_\ell(\mathbf{r}) = \int_{\Omega_\ell} G_\ell(\mathbf{r}, \mathbf{r_s}) q_\ell(\mathbf{r}) d(\mathbf{r_s}) \tag{4.14}$$

Moreover, from the definition of the Dirac distribution we have:

$$\Phi_\ell(\mathbf{r}) = \int_{\Omega_\ell} \delta(\mathbf{r} - \mathbf{r_s}) \Phi_\ell(\mathbf{r}) d(\mathbf{r_s}) \quad \forall \quad \mathbf{r} \in \Omega \tag{4.15}$$

Let's consider Equation (4.13) on the subdomain Ω_ℓ once more. The function $\Phi_\ell(\mathbf{r})$ satisfies the values of diffusion equation for every point $\mathbf{r} \in \Omega$ by definition. However, the Green's functions $G_\ell(\mathbf{r}, \mathbf{r_s})$ satisfies diffusion equation everywhere except on the boundary $\partial\Omega$,where it has a singularity when $\mathbf{r_s} \rightarrow \mathbf{r}$.

4.5 Boundary Integral Equation

To obtain the *Boundary Integral Equation*, a governing equation for the values of $\Phi_\ell(\mathbf{r})$ over the boundary, let $\mathbf{r}$ approach the outer boundary Γ_ℓ and returning to the notations that we used earlier to get:

$$\begin{aligned} I_\ell(\mathbf{r}) \; + \; & \int_{\Gamma_\ell} \left(I_\ell(\mathbf{r_s}) \partial_\ell G_\ell(\mathbf{r}, \mathbf{r_s}) - G_\ell(\mathbf{r}, \mathbf{r_s}) D_\ell^{-1} J_\ell(\mathbf{r_s}) \right) dS(\mathbf{r_s}) \\ - \; & \int_{\Gamma_{\ell+1}} \left(I_{\ell+1}(\mathbf{r_s}) \partial_\ell G_\ell(\mathbf{r}, \mathbf{r_s}) - G_\ell(\mathbf{r}, \mathbf{r_s}) D_{\ell+1}^{-1} J_{\ell+1}(\mathbf{r_s}) \right) dS(\mathbf{r_s}) = Q_\ell(\mathbf{r}) \\ & 1 \leq \ell \leq L-1 \end{aligned} \tag{4.16}$$

We notice that in this form the first integral is singular while the second has a continuous kernel. Similarly, if the variable $\mathbf{r}$ approach the inner interface $\Gamma_{\ell+1}$, we get the equation:

$$\begin{aligned} I_{\ell+1}(\mathbf{r}) \; - \; & \int_{\Gamma_{\ell+1}} \left(I_{\ell+1}(\mathbf{r_s}) \partial_\ell G_\ell(\mathbf{r}, \mathbf{r_s}) - G_\ell(\mathbf{r}, \mathbf{r_s}) D_{\ell+1}^{-1} J_{\ell+1}(\mathbf{r_s}) \right) dS(\mathbf{r_s}) \\ + \; & \int_{\Gamma_\ell} \left(I_\ell(\mathbf{r_s}) \partial_\ell G_\ell(\mathbf{r}, \mathbf{r_s}) - G_\ell(\mathbf{r}, \mathbf{r_s}) D_\ell^{-1} J_\ell(\mathbf{r_s}) \right) dS(\mathbf{r_s}) = Q_\ell(\mathbf{r}) \\ & 1 \leq \ell \leq L-1 \end{aligned} \tag{4.17}$$

where again the first integral is singular so that the integral over $\Gamma_{\ell+1}$ may not converge for $\mathbf{r} \in \Gamma_{\ell+1}$. A proper limiting process described in [16, 20], must be invoked, designed to account for the singularity of the fundamental solutions. The above equation, when $\mathbf{r}$ approaches the outer boundary Γ_ℓ, will take the form:

$$\begin{aligned} C_\ell^+(\mathbf{r})I_\ell(\mathbf{r}) \;+\; & \int_{(\Gamma_\ell - \sigma_\varepsilon^+)} \left(I_\ell(\mathbf{r_s})\partial_\ell G_\ell(\mathbf{r},\mathbf{r_s}) - G_\ell(\mathbf{r},\mathbf{r_s})D_\ell^{-1}J_\ell(\mathbf{r_s})\right) dS(\mathbf{r_s}) \\ - \; & \int_{\Gamma_{\ell+1}} \left(I_{\ell+1}(\mathbf{r_s})\partial_\ell G_\ell(\mathbf{r},\mathbf{r_s}) - G_\ell(\mathbf{r},\mathbf{r_s})D_{\ell+1}^{-1}J_{\ell+1}(\mathbf{r_s})\right) dS(\mathbf{r_s}) = Q_\ell(\mathbf{r}) \\ & 1 \le \ell \le L-1 \end{aligned} \tag{4.18}$$

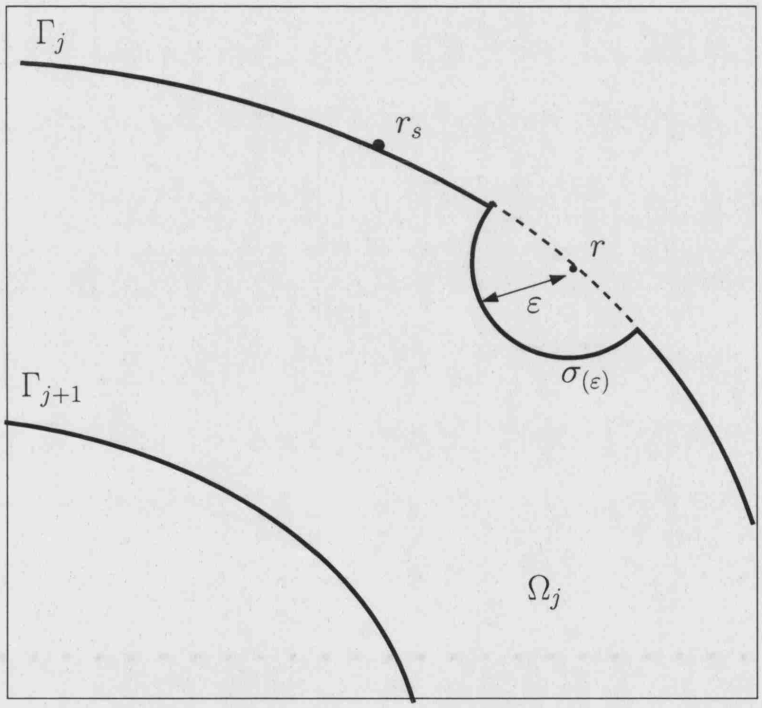

Figure 4.2: Limiting process for the small hemisphere $\sigma_{(\varepsilon)}$

The term $C_\ell^{\pm}(\mathbf{r})$, arises due to the singularities on the boundary, and the integration of the Green's functions over the interface. $C_\ell^{\pm}(\mathbf{r})$ can be calculated by surrounding the point $\mathbf{r}$, which lays on the boundary, by a small hemisphere $\sigma_{(\varepsilon)}$ of radius ε and taking each term in (4.18) in the limit when $\varepsilon \to 0$. We notice that in this form that both integrals are now continuous.

Similarly, if the variable $\mathbf{r}$ approach the inner interface $\Gamma_{\ell+1}$, we get the equation:

$$\begin{aligned} C_\ell^-(\mathbf{r})I_{\ell+1}(\mathbf{r}) \quad - & \int_{(\Gamma_{\ell+1}-\sigma_\varepsilon^-)} \left(I_{\ell+1}(\mathbf{r_s})\partial_\ell G_\ell(\mathbf{r},\mathbf{r_s}) - G_\ell(\mathbf{r},\mathbf{r_s})D_{\ell+1}^{-1}J_{\ell+1}(\mathbf{r_s})\right) dS(\mathbf{r_s}) \\ + & \int_{\Gamma_\ell} \left(I_\ell(\mathbf{r_s})\partial_\ell G_\ell(\mathbf{r},\mathbf{r_s}) - G_\ell(\mathbf{r},\mathbf{r_s})D_\ell^{-1}J_\ell(\mathbf{r_s})\right) dS(\mathbf{r_s}) = Q_\ell(\mathbf{r}) \\ & 1 \le \ell \le L-1 \end{aligned} \tag{4.19}$$

In [16], [20] it is shown that this term does not need to be calculated explicitly, and can be obtained indirectly by some physical considerations. In the case of the observation point upon a smooth surface,which is the case considered here:

$$C_\ell^+(\mathbf{r}) = C_\ell^-(\mathbf{r}) = \frac{1}{2}. \tag{4.20}$$

Using,(4.18) and (4.19) and the boundary conditions (4.10), to state the relation between I_1 and J_1 and thus eliminate one of the unknowns, we can construct a system of $2n-1$ equations with $2n-1$ unknowns, $I_1, I_2, \ldots, I_L, J_2, \ldots, J_L$.Solving for these functions the integral representation (4.13), yields the field Φ.

4.6 Numerical implementation

The Boundary Integral formulation that has been developed so far has a clear mathematical form. If the boundaries of the domains Ω_ℓ can be represented by simple equations, for example a sphere, then analytic integration of (4.18) and (4.19) could be possible, though quite tedious.

However to cover general geometries, a numerical implementation of the integration is necessary. As in any form of numerical integration the surface interfaces Γ_ℓ will be discretised in P_ℓ surface elements $\tau_{\ell,k}$; $k = 1, \ldots, P_\ell$ with N_ℓ vertices $\mathbf{N}_{\ell,k'}$; $k' = 1, \ldots, N_\ell$. Those surface elements will be called *Boundary Elements*.

The discretisation procedure using parametric surfaces and mapping on the sphere will be explained in chapter 6. For the framework of the numerical implementation we should only note, that triangles defined by 6 nodes using the quadratic shape functions (4.38) have been used in our approach, like the one shown in the following graph.

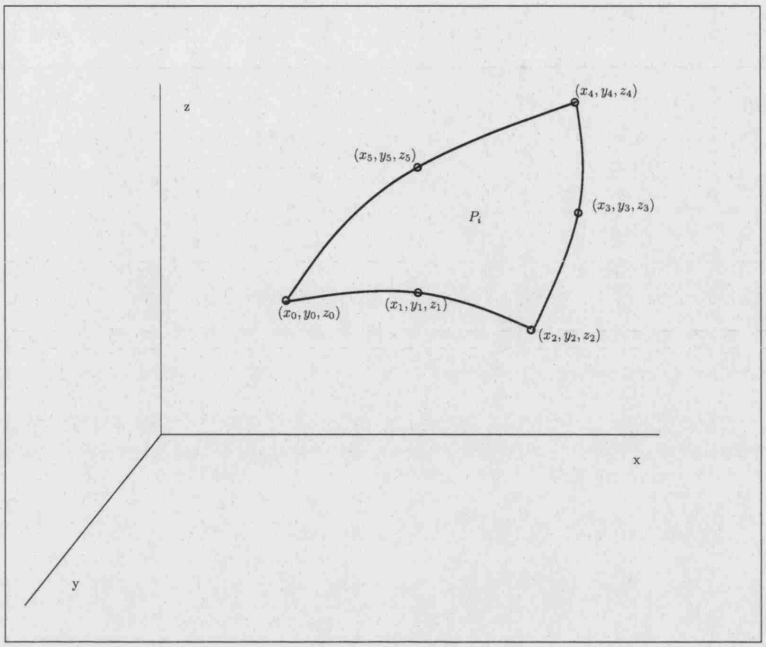

Figure 4.3: Quadratic surface triangle defined by six nodes

Having defined the discretisation of the surface Γ_ℓ we can approximate the functions I_ℓ and J_ℓ by the use of nodal basis functions u_k, restricted to Γ_ℓ.

$$I_\ell(\mathbf{r}) \approx \sum_{k'=1}^{N_\ell} I_{\ell,k'} u_{\ell,k'}(\mathbf{r}), \qquad J_\ell(\mathbf{r}) \approx \sum_{k'=1}^{N_\ell} J_{\ell,k'} u_{\ell,k'}(\mathbf{r}) \tag{4.21}$$

Nodal basis functions are one efficient way to describe the variation of the variables on an element, since they use only the nodal values to describe the behaviour of any element. We should also notice that representation (4.21) expresses both I_ℓ and J_ℓ using the nodal basis functions. This representation enforces J_ℓ to be at least continuous or C^0, where the notation C^e function refers to an e times differentiable function with continuous derivatives. The integrals occurring in the Boundary Integral equations (4.18) and (4.19) take the form:

$$i_\ell = \sum_{k'=1}^{N_\ell} I_{\ell,k'} \int_{\Gamma_\ell} \partial_\ell G_\ell(\mathbf{r}, \mathbf{r_s}) u_{\ell,k'} dS(\mathbf{r_s}) \tag{4.22}$$

$$j_\ell = \sum_{k'=1}^{N_\ell} J_{\ell,k'} \int_{\Gamma_\ell} G_\ell(\mathbf{r}, \mathbf{r_s}) u_{\ell,k'} dS(\mathbf{r_s}) \tag{4.23}$$

To obtain the discrete representation, we formally consider integrating the quantities

$i_\ell(\mathbf{r})$, $j_\ell(\mathbf{r})$ in the above equations with the test function $\psi_k(\mathbf{r})$:

$$i_{\ell,k} = \int_{\Gamma_\ell} \psi_k(\mathbf{r}) i_\ell(\mathbf{r}) dS(\mathbf{r_s}) \tag{4.24}$$

$$= \sum_{k'=1}^{N_\ell} I_{\ell,k'} \int_{\Gamma_\ell} \int_{\Gamma_\ell} \psi_k(\mathbf{r}) \partial_\ell G_\ell(\mathbf{r}, \mathbf{r_s}) u_{\ell,k'}(\mathbf{r_s}) dS(\mathbf{r_s}) dS(\mathbf{r}) \tag{4.25}$$

$$j_{\ell,k} = \int_{\Gamma_\ell} \psi_k(\mathbf{r}) j_\ell(\mathbf{r}) dS(\mathbf{r_s}) \tag{4.26}$$

$$= \sum_{k'=1}^{N_\ell} J_{\ell,k'} \int_{\Gamma_\ell} \int_{\Gamma_\ell} \psi_k(\mathbf{r}) G_\ell(\mathbf{r}, \mathbf{r_s}) u_{\ell,k'}(\mathbf{r_s}) dS(\mathbf{r_s}) dS(\mathbf{r}) \tag{4.27}$$

For *Galerkin BEM* we take

$$\psi_k(\mathbf{r}) = u_{\ell,k}(\mathbf{r}) \tag{4.28}$$

following an approach familiar from the Finite Element method. For the scope of the calculations that are necessary for our problem we decided to use a much easier approach, that of *Collocation BEM*, where the integral equation is enforced exactly at the nodal points $\mathbf{N}_{\ell,k}$ and therefore:

$$\psi_k(\mathbf{r}) = \delta(\mathbf{r} - \mathbf{N}_{\ell,k})) =: \delta_{\ell,k}(\mathbf{r}). \tag{4.29}$$

The use of the *point Collocation* is a common practice in the BEM literature [16, 17, 67] and in comparison with the *weighted residual methods* e.g. Galerkin it reduces the complexity and the computational effort without resulting in substantial decrease in accuracy [17].

4.7 Matrix assembly

For the solution of the system of the $2L-1$ equations that we formed we introduce the following notation. Let $\mathrm{A}_{\ell\ell'}, \mathrm{B}_{\ell\ell'}$, be $N_\ell \times N_{\ell'}$ matrices corresponding to surface $\Gamma_{\ell'}$ of subdomain Ω_ℓ with entries:

$$\mathrm{A}_{\ell\ell'}(k,k') = \int_{\Gamma_{\ell'}} \int_{\Gamma_{\ell'}} \delta_{\ell',k}(\mathbf{r}) \partial_\ell G_\ell(\mathbf{r}, \mathbf{r_s}) u_{\ell',k'}(\mathbf{r_s}) dS(\mathbf{r_s}) dS(\mathbf{r}) = \tag{4.30}$$

$$= \int_{\Gamma_{\ell'}} \partial_\ell G_\ell(\mathbf{N}_{\ell',k}, \mathbf{r_s}) u_{\ell',k'}(\mathbf{r_s}) dS(\mathbf{r_s}) \tag{4.31}$$

$$\mathrm{B}_{\ell\ell'}(k,k') = D_\ell^{-1} \int_{\Gamma_{\ell'}} \int_{\Gamma_{\ell'}} \delta_{\ell',k'}(\mathbf{r}) G_\ell(\mathbf{r}, \mathbf{r_s}) u_{\ell',k'}(\mathbf{r_s}) dS(\mathbf{r_s}) dS(\mathbf{r}) = \tag{4.32}$$

$$= D_\ell^{-1} \int_{\Gamma_{\ell'}} G_\ell(\mathbf{N}_{\ell',k}, \mathbf{r_s}) u_{\ell',k'}(\mathbf{r_s}) dS(\mathbf{r_s}) \tag{4.33}$$

Using the boundary conditions (4.10) to reduce the J_1 function from the first equation:

$$J_1 = -\frac{I_1}{2\alpha} \tag{4.34}$$

Equations (4.18)and (4.19) give rise to a discrete form:

$$\begin{aligned}
\left[\frac{1}{2}\mathrm{I} + \mathrm{A}_{11} + \frac{1}{2\alpha}\mathrm{B}_{11}\right] I_1 - \mathrm{A}_{12} I_2 + \mathrm{B}_{12} J_2 &= Q_1 \\
&\vdots \\
\left[\frac{1}{2}\mathrm{I} + \mathrm{A}_{\ell\ell}\right] I_\ell - \mathrm{B}_{\ell\ell} J_\ell - \mathrm{A}_{\ell\ell+1} I_{\ell+1} + \mathrm{B}_{\ell\ell+1} J_{\ell+1} &= 0 \\
\mathrm{A}_{\ell\ell} I_\ell - \mathrm{B}_{\ell\ell} J_\ell + \left[\frac{1}{2}\mathrm{I} - \mathrm{A}_{\ell\ell+1}\right] I_{\ell+1} + \mathrm{B}_{\ell\ell+1} J_{\ell+1} &= 0 \\
&\vdots \\
\left[\frac{1}{2}\mathrm{I} + \mathrm{A}_{nn}\right] I_n - \mathrm{B}_{nn} J_n &= 0
\end{aligned}$$

Adjusting the notation to save space:

$$\mathrm{C}_{\ell\ell} = \frac{1}{2}\mathrm{I} + \mathrm{A}_{\ell\ell}, \qquad \mathrm{D}_{\ell\ell} = \frac{1}{2}\mathrm{I} - \mathrm{A}_{\ell\ell}, \qquad \bar{\mathrm{C}}_{\ell\ell} = \mathrm{C}_{\ell\ell} + \frac{1}{2\alpha}\mathrm{B}_{\ell\ell}$$

We get the matrix system:

$$\begin{pmatrix}
\bar{\mathrm{C}}_{11} & -\mathrm{A}_{12} & \mathrm{B}_{12} & 0 & \cdots & 0 & 0 & 0 \\
 & \cdots & \cdots & & & & & \\
0 & \mathrm{C}_{\ell\ell} & -\mathrm{B}_{\ell\ell} & -\mathrm{A}_{\ell\ell+1} & \mathrm{B}_{\ell\ell+1} & & & \\
\vdots & \mathrm{A}_{\ell\ell} & -\mathrm{B}_{\ell\ell} & \mathrm{D}_{\ell\ell+1} & \mathrm{B}_{\ell\ell+1} & & & \\
0 & 0 & 0 & \mathrm{C}_{\ell+1\ell+1} & -\mathrm{B}_{\ell+1\ell+1} & -\mathrm{A}_{\ell+1\ell+2} & \mathrm{B}_{\ell+1\ell+2} & \\
0 & 0 & \cdots & \mathrm{A}_{\ell+1\ell+1} & -\mathrm{B}_{\ell+1\ell+1} & \mathrm{D}_{\ell+1\ell+2} & \mathrm{B}_{\ell+1\ell+2} & \\
\vdots & \vdots & \cdots & \cdots & & & & \\
0 & 0 & \cdots & & & & \mathrm{C}_{nn} & -\mathrm{B}_{nn}
\end{pmatrix}
\begin{pmatrix} I_1 \\ I_2 \\ J_2 \\ \vdots \\ I_\ell \\ J_\ell \\ I_{\ell+1} \\ J_{\ell+1} \\ \vdots \\ I_n \\ J_n \end{pmatrix}
=
\begin{pmatrix} Q_1 \\ Q_2 \\ 0 \\ \vdots \\ 0 \\ 0 \\ 0 \\ 0 \\ \vdots \\ 0 \\ 0 \end{pmatrix}$$

Where the terms Q_1 and Q_2 are calculated from the source term (4.14), for the nodes of the participating boundaries Γ_1 and Γ_2 respectively. This is due to the positioning of the source we decided to use, located inside Ω_1 and therefore visible from both Γ_1 and Γ_2.

We can rewrite (4.35)as a linear matrix equation:

$$\mathrm{T}\,\mathbf{\Phi} = \mathbf{q} \tag{4.35}$$

4.8 Non-singular integrals

The calculation of the integrals present in the Boundary Integral Equation (4.18) and (4.19), especially with the use of the higher-order elements, becomes too complicated for analytical integration. However due to the fact that the precise calculation of those integrals is fundamental to the accuracy of the numerical implementation of the integral equations, an efficient and accurate numerical integration scheme is necessary [16].

In the case of non-singular integrals, ($\mathbf{r} \neq \mathbf{r_s}$), a mapping of the quadratic triangle to local coordinates in addition to a Gaussian quadrature scheme is used. A brief description for the technique follows.

Initially, every triangle described in Cartesian coordinates is mapped to the local coordinates (ξ_1, ξ_2). The objective of this mapping is to convert the three dimensional quadratic triangle as shown in figure (4.3) to the equivalent two-dimensional flat triangle shown in figure (4.4). The following nonlinear mapping functions were used.

$$\begin{aligned} x(\xi_1,\xi_2) &= \sum_{i=1}^{6} u_i(\xi_1,\xi_2)x_i \\ y(\xi_1,\xi_2) &= \sum_{i=1}^{6} u_i(\xi_1,\xi_2)y_i \\ z(\xi_1,\xi_2) &= \sum_{i=1}^{6} u_i(\xi_1,\xi_2)z_i \end{aligned} \tag{4.36}$$

(4.37)

Where the shape functions u_i were defined by:

$$\begin{aligned} u_1 &= (\xi_1+\xi_2)+2(\xi_1+\xi_2)^2 & u_2 &= -4\xi_1(\xi_1+\xi_2) \\ u_3 &= -\xi_1(1-2\xi_1) & u_4 &= 4\xi_1\xi_2 \\ u_5 &= -\xi_2(1-2\xi_2) & u_6 &= -4\xi_2(\xi_1+\xi_2) \end{aligned} \tag{4.38}$$

Considering the integrals of the boundary element formulation (4.30), they have the form:

$$\int_{\Gamma} f(x,y,z)dS, \tag{4.39}$$

where by $f(x,y,z)$ we represent the integrand, either Green's functions or the normal derivatives of Green's functions expressed in the Cartesian coordinates. Then the introduced mapping changes the variables (x,y,z) to (ξ_1,ξ_2) producing the equivalent expression for (4.39):

$$\int_0^1 \int_0^{1-\xi_1} f(\xi_1,\xi_2)\, J_1(\xi_1,\xi_2)\, d\xi_1 d\xi_2. \tag{4.40}$$

We notice the introduction of

$$J_1(\xi_1,\xi_2) = \begin{vmatrix} \frac{\partial x}{\partial \xi_1} & \frac{\partial x}{\partial \xi_2} & \hat{\mathbf{e}}_x \\ \frac{\partial y}{\partial \xi_1} & \frac{\partial y}{\partial \xi_2} & \hat{\mathbf{e}}_y \\ \frac{\partial z}{\partial \xi_1} & \frac{\partial z}{\partial \xi_2} & \hat{\mathbf{e}}_z \end{vmatrix}. \tag{4.41}$$

which is the transformation Jacobian necessary for the change of the integration variables and $\{\hat{\mathbf{e}}_x, \hat{\mathbf{e}}_y, \hat{\mathbf{e}}_z\}$ the normal unit vectors in the respective directions x,y and z.

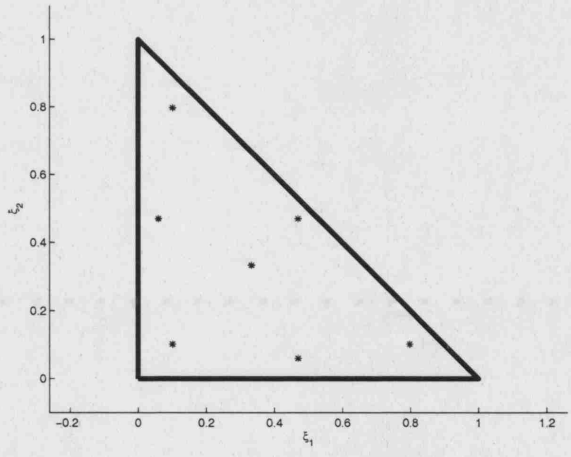

Figure 4.4: Quadratic surface triangle mapped onto the flat triangle of local coordinates $(\xi_1,\ \xi_2)$. Gaussian points used, printed as stars.

Using Gaussian quadrature, the integral of a function f can be approximated by the sum of its functional values at a set of predefined points, multiplied by certain aptly defined weighting coefficients [97].

$$\int_0^1 \int_0^{1-\xi_1} f(\xi_1,\xi_2)\ J_1(\xi_1,\xi_2)\ d\xi_1 d\xi_2 = \sum_{m=1}^{g_m} f(\xi_{1,m},\xi_{2,m})\ J_1(\xi_{1,m},\xi_{2,m})\ w_m \quad (4.42)$$

The Gaussian scheme is based on an approximation of a smooth function by polynomials. In order to produce accurate results an optimisation of the points and weights should be performed on the specific domain and integrand. However, the scheme finally used was taken from literature [137], where it comes as a generic approach for the case of flat triangular elements and uses the seven Gaussian points and weights given in table (4.1), produced satisfactory results. In the future work we hope to investigate further on the optimised Gaussian quadrature in order to reduce cost and possibly increase accuracy.

m	$\xi_{1,m}$	$\xi_{2,m}$	w_m
1	0.333333333333333	0.333333333333333	0.1125
2	0.059715871789769	0.470142064105115	0.0661970763942531
3	0.470142064105115	0.0597158717897698	0.0661970763942531
4	0.470142064105115	0.470142064105115	0.0661970763942531
5	0.797426985353087	0.101286507323456	0.0629695902724136
6	0.101286507323456	0.797426985353087	0.0629695902724136
7	0.101286507323456	0.101286507323456	0.0629695902724136

Table 4.1: Gaussian points and weights for a flat triangular element.

4.9 Singular integrals

When the point $\mathbf{r}$ is near or coincident with one of the integration points $\mathbf{r_s}$ the integral varies sharply. A singularity occurs in this case due to the denominator in the Green's function (3.31) approaching zero, and a special treatment for the integration is necessary. The method that we choose for the effective integration with high accuracy without an excessive amount of calculation is a regularisation method introducing a division of the singular elements into several triangles and then a transformation of the singular triangles to squares (fig.(4.5)). Gaussian quadrature is then applied to the squares for the integration. The transformation results in a concentration of Gaussian points around the singularity (4.6), and therefore better approximation of the rapid variation of the integrand around it.

Starting from the quadratic triangle defined in a three dimensional Cartesian space (x, y, z) the mapping (4.36), with the shape functions u_i defined in (4.38), as in the non-singular case is

used to transform the triangle to a two dimensional local coordinate space (ξ_1, ξ_2). The results of this mapping are visualised in the graph (4.7) on the first two rows.

For the next step there are two different approaches depending on the position of the singular node on the triangle.

1. In the case of a singular node in the corner of the triangle, as shown in the left column of (4.7), the triangle is first divided to four subtriangles T_1, T_2, T_3 and T_0 as shown in figure (4.7). The singularity is now placed in subtriangle T_0 and so the integral over T_1, T_2 and T_3 can be calculated by the use of the non-singular method.

   The subtriangle T_0 should be treated differently and it is mapped onto a square by introducing a new space of local coordinates (η_1, η_2) as shown in the left bottom of figure (4.7). We notice that the singularity point will be mapped to a side of the square. The mapping is defined by the equations

$$\xi_1 = \sum_{i=1}^{3} M_i(\eta_1\eta_2)\xi_{1i} \tag{4.43}$$

$$\xi_2 = \sum_{i=1}^{3} M_i(\eta_1\eta_2)\xi_{2i} \tag{4.44}$$

   Where the transformation functions are defined by:

$$\begin{aligned} M_1 &= \frac{1}{4}(1+\eta_1)(1-\eta_2) \\ M_2 &= \frac{1}{4}(1+\eta_1)(1+\eta_2) \\ M_3 &= \frac{1}{2}(1-\eta_1) \end{aligned} \tag{4.45}$$

   This mapping introduces a second Jacobian $J_2(\eta_1, \eta_2)$ which is calculated by,

$$J_2(\eta_1, \eta_2) = \begin{vmatrix} \frac{\partial \xi_1}{\partial \eta_1} & \frac{\partial \xi_1}{\partial \eta_2} \\ \frac{\partial \xi_2}{\partial \eta_1} & \frac{\partial \xi_2}{\partial \eta_2} \end{vmatrix}. \tag{4.46}$$

   The integral (4.39) takes then the equivalent expression:

$$\int_{-1}^{1}\int_{-1}^{1} f(\eta_1, \eta_2)\ J_1(\eta_1, \eta_2)\, J_2(\eta_1, \eta_2)\, d\eta_1 d\eta_2 \tag{4.47}$$

There is a Gaussian quadrature scheme for calculation of integrals on the square from [83], using all the combinations of the points and weights in table (4.2). There are 6 Gauss points for each direction and the 36 combinations used are shown plotted as dots on fig.(4.5). From the Gaussian quadrature (4.47) can be approximated by

$$\sum_{m=1}^{6}\sum_{n=1}^{6} f(\eta_{1,m},\eta_{2,n})\ J_1(\eta_{1,m},\eta_{2,n})\ \ J_2(\eta_{1,m},\eta_{2,n})\ \ w_m\, w_n \tag{4.48}$$

We should notice fig.(4.6) where the Gauss points from the square are mapped back to the flat triangle, the concentration of Gauss points around the corner node with the singularity $(0,0)$ is apparent.

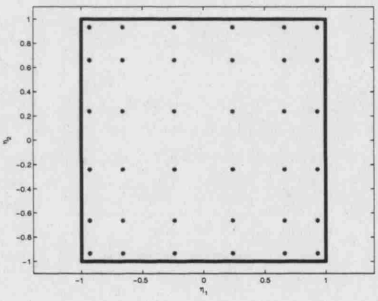

Figure 4.5: The triangle mapped on the square (η_1,η_2).

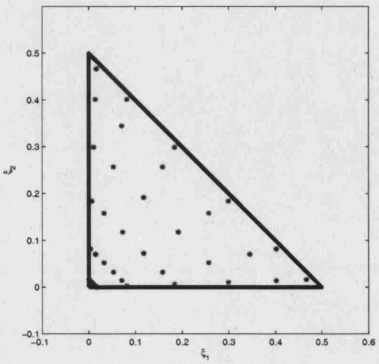

Figure 4.6: The Gaussian quadrature points used on the square mapped back to the flat triangle space (ξ_1,ξ_2). We notice the concentration of points around the singularity point $(0,0)$.

m	$\eta_{1,m}$	$\eta_{2,m}$	w_m
1	-0.93246951420315202781	-0.93246951420315202781	0.17132449237917034504
2	-0.66120938646626451366	-0.66120938646626451366	0.36076157304813860757
3	-0.23861918608319690863	-0.23861918608319690863	0.46791393457269104739
4	0.23861918608319690863	0.23861918608319690863	0.46791393457269104739
5	0.66120938646626451366	0.66120938646626451366	0.36076157304813860757
6	0.93246951420315202781	0.93246951420315202781	0.17132449237917034504

Table 4.2: Gauss points and weights for the flat square (4.5)

2. On the case where the singular node is in the middle of the triangle edge, as shown in figure (4.7) on the right side, the triangle is divided into the four subtriangles T_0, T_1, T_2 and T_3. The singular node participates in the three triangles T_0, T_1, T_2. Following, integration over the triangle T_3 is calculated as in the non-singular case, while triangles T_0, T_1, T_2 are individually mapped to squares and the numerical integration proceeds as explained previously.

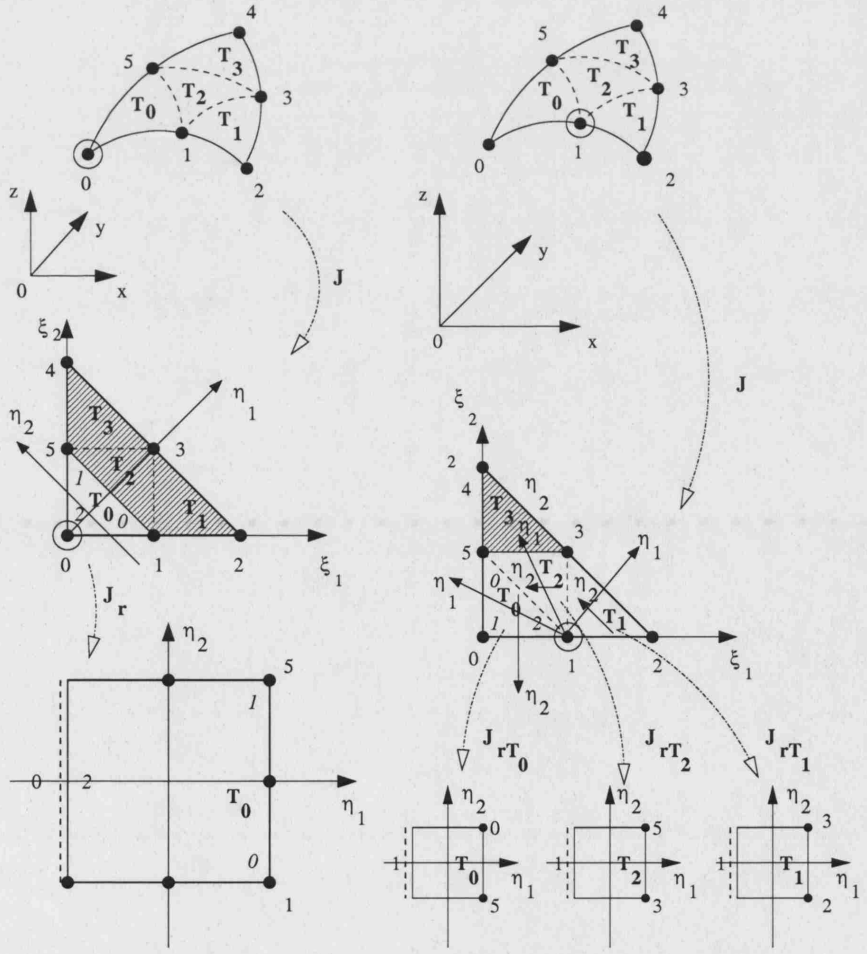

Figure 4.7: Two cases of iso-parametric triangle subdivision for different positions of the singular point. (Graph courtesy Prof. Jan Sikora)

4.10 Solution of the linear system

As a general rule, the underlying principal in most numerical techniques is the formation of a set of linear algebraic equations where the number of equations is equal to the number of unknown functions to be calculated. In the previous sections Boundary Element Method was used for the construction of this linear system of equations (4.35) , which we rewrite here:

$$\mathbf{T}\Phi = \mathbf{q}. \tag{4.49}$$

T is the system matrix, Φ the vector of unknown boundary field values and $\mathbf{q}$ the vector of known coefficients calculated from the light sources in the problem. In this BEM implementation since the system matrix is non-symmetric and quite populated the Generalised Minimum Residuals Method (GMRES), is used to solve (4.35). This method initially proposed by Saad and Schultz in [109] is commonly used for the solution of large linear systems of algebraic equations.

4.11 Conclusions and results

In this chapter the boundary element method was formulated for the solution of the diffusion equation (3.24) or rather the equivalent for homogeneous regions Helmholtz (3.30), with Robin boundary conditions (3.37). This formulation will be used for the physical modelling of the light measurements used in optical tomography, and is part of the forward operator necessary for the solution of the inverse problem.

To test the accuracy of the BEM solution before using it on non-trivial geometries, we will use a homogeneous spherical region presented in fig.(4.8) where the analytical solution of the diffusion equation is possible [12].

Calculations have been performed for a point source on a sphere with $20mm$ diameter. The source was located a distance $z_d = 1/\mu_s' mm$ in from the surface, and a refractive index of 1.0 was assumed, the speed of light was $c = 0.3mm\ (ps)^{-1}$. Representative optical properties of the brain tissue $\mu_a = 0.025mm^{-1}$ and $\mu_s' = 2.0mm^{-1}$ were used. The modulation frequency was $200MHz$.

The discretisation of the surface was in 980 quadratic triangular boundary elements with 1962 nodes, as seen in fig.(4.8).

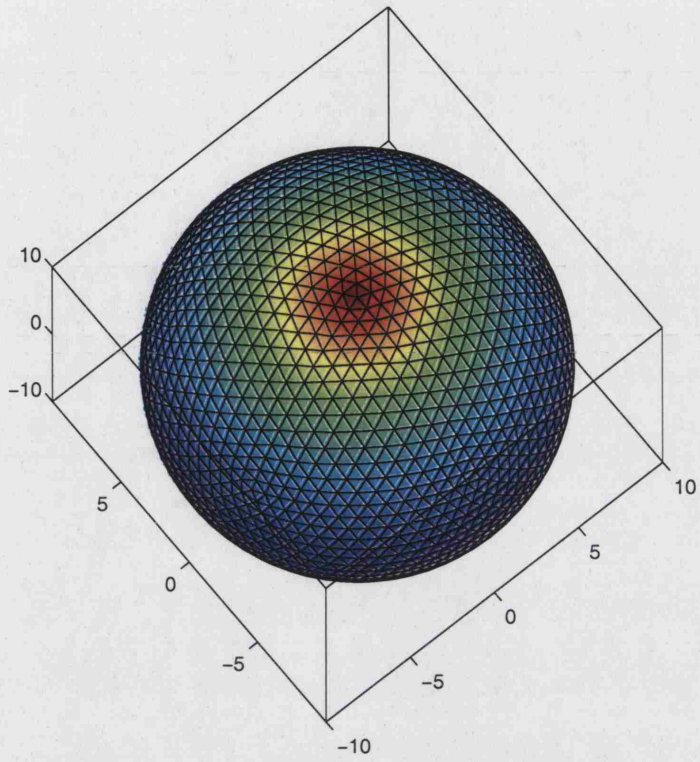

Figure 4.8: Discretisation of a sphere surface, in quadratic triangle elements.

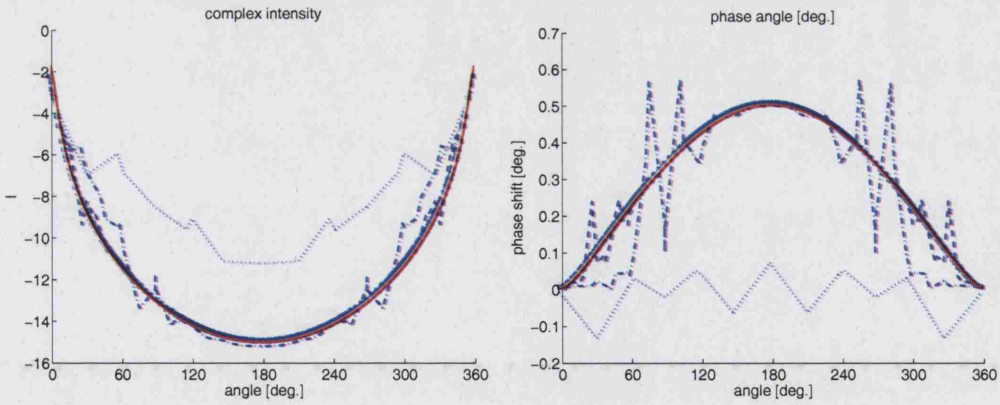

Figure 4.9: BEM convergence results for the photon density I along the equator on the surface of the sphere fig. (4.8). On the left the log plot of amplitude $|I|$ and on the right the phase shift $\arg(I)$. $(\cdot\cdot)$: BEM solution with 20 elements. $(\cdot-)$: BEM solution with 80 elements. $(--)$: BEM solution with 180 elements. (x) : BEM solution with 980 elements. (solid line) : analytical solution .

The results of the solution from the boundary elements linearised system (4.35) for the photon density I_1 on the sphere's surface can be seen in fig. (4.9). In the (FD) experiment the results are complex numbers so that the amplitude and the phase shift of the photon density I_1 on the circumference of the sphere on the equator has been plotted, together with an analytical solution

taken from [12].

In (4.9 the convergence of BEM results is demonstrated , as the resolution of the mesh is increased, to the analytical expression for the Green's function for this system, [14]. The general conclusion is that BEM can be used to produce a quite accurate and stable numerical solution for problems governed from the diffusion equation with Robin boundary conditions. Therefore, it could be suitable for the modelling of the measurements used in Optical Tomography as long as the assumption that the domain Ω could be divided into homogeneous regions Ω_ℓ, holds.

Furthermore, the setting up of the geometrical model is easy to facilitate, since the discretisation of just the boundaries Γ_ℓ is sufficient. In chapter (6), a parametric description of such boundaries will be employed for the construction of a flexible geometric model.

Chapter 5

Optimisation

5.1 Introduction

Optimisation is an important strategy for the solution of an inverse problem with the minimisation of the least squares functional. Furthermore, optimisation is an essential part of the parametrisation algorithm that we describe in chapter 6. Therefore, in this chapter a general introduction to the notions involved in the optimisation of a scalar function h that depends on one or more independent *variables* $\mathbf{x}$ is given. The term optimisation in the mathematical sense, refers to the tracking of the point in the parameter space of $\mathbf{x}$, where h takes on a minimum or maximum value. The two problems of maximisation and minimisation are conceptually related to each other since maximisation of h is equal to minimisation of $-h$. Therefore, we will refer to optimisation as the procedure for the minimisation of the function h. In the framework of optimisation h will be called the *objective function.*

Several powerful methods for the minimisation of functions have been presented in the numerical research world. Speed and memory requirements are the main computational characteristics of a minimisation algorithm. On the other hand the sensitivity to local minima and the involvement or not of the derivatives of the function pose a vital role in the selection of a particular algorithm for each problem. According to [97] algorithms that make use of the derivative of the objective function are somewhat more powerful than those that use only the function. In the scopes of this thesis we will examine three families of multidimensional minimisation that includes the calculation of first derivatives, that is *steepest descent*, *conjugate gradient* and *Newton* method.

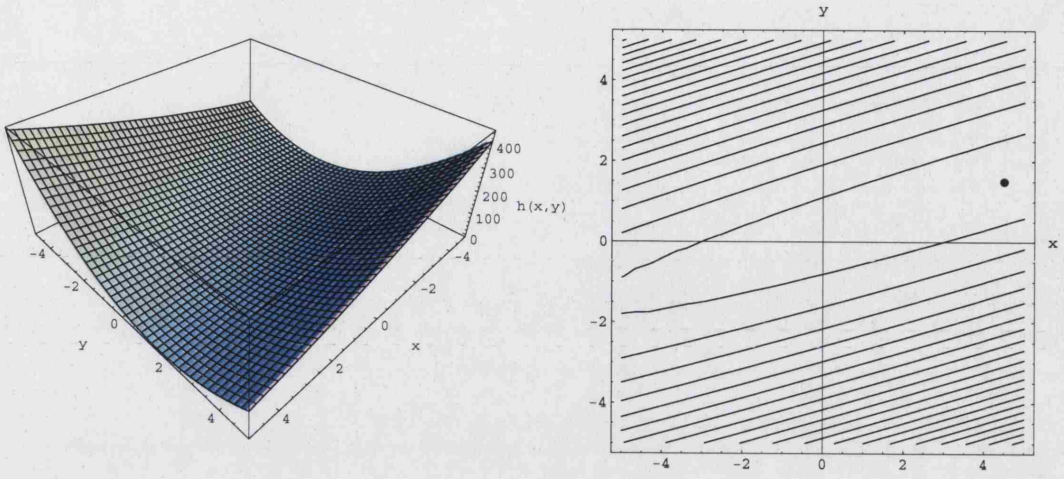

Figure 5.1: (left) Graph of the function h. (right) Contour plot for h. Each ellipsoidal curve has constant $h(\mathbf{x})$

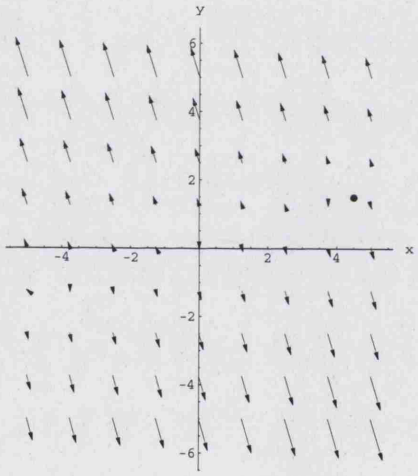

Figure 5.2: Gradient of the function h, plotted as a vector field. At each $\mathbf{x}$ the gradient points in the steepest increase direction and is orthogonal to the contour lines.

For better visual comprehension we will use the scalar function

$$h(x, y) = (x - 3y)^2 + (y - 1.5)^2. \tag{5.1}$$

Starting from the point $\mathbf{x}_0 = \{-4, 0.7\}$ we will try to find the minimum, which is at point $\{4.5, 1.5\}$ (see fig. 5.1). The gradient of h at a point $\mathbf{x}_i = \{x_i, y_i\}$ will be given by

$$\nabla h(\mathbf{x}_i) = \mathbf{G}(x_i, y_i) = [\ 2(x_i - 3y_i)\ ,\quad -6(x_i - 3y_i) + 2(-1.5 + y_i)\ ]^T \tag{5.2}$$

which will point in the steepest ascent direction and be orthogonal to the contour lines of h (see

fig. 5.2).

5.2 Steepest descent method

One basic method for finding the nearest local minimum of a function, which presupposes that the gradient of the function can be computed, is steepest descent. At a point $\mathbf{x}_i$ the gradient vector $\nabla h(\mathbf{x}_i)$ shows the steepest assent direction. Steepest descent works iteratively, moving from $\mathbf{x}_i$ to $\mathbf{x}_{i+1}$ by minimising along the line extending from $\mathbf{x}_i$ in the direction of $-\nabla h(\mathbf{x}_i)$, opposite to the local uphill gradient. The iterative update for $\mathbf{x}$ will be given by:

$$\mathbf{x}_{i+1} = \mathbf{x}_i - \lambda \nabla h(\mathbf{x}_i) \tag{5.3}$$

The directional minimum is reached by a line search along the values of λ. Results from the steepest descent method can be seen in fig. (5.3). We notice that since λ minimises h, along the line $\lambda \nabla h(\mathbf{x}_i)$, the directional derivative $\frac{\partial}{\partial \lambda} h(\mathbf{x}_i)$ should be zero. Therefore the gradient of h at the point $\mathbf{x}_{i+1}$ should be orthogonal to the direction $\lambda \cdot \nabla h(\mathbf{x}_i)$. So as we can see in fig. (5.3), steepest descent moves in directions orthogonal to the previous steps. Usually, steepest descent method has slow convergence in finding local minima. [118, 94].

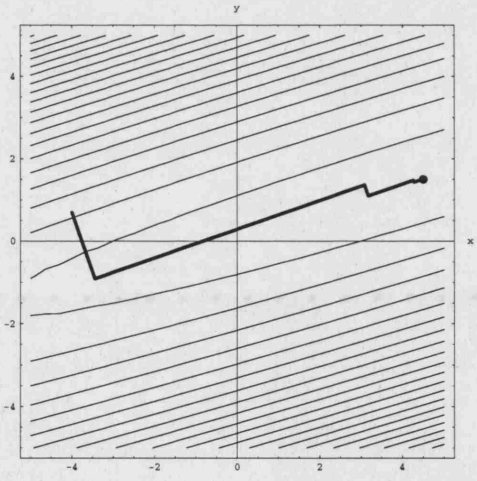

Figure 5.3: The method of steepest descent

5.3 Conjugate Gradient method

The Conjugate Gradient method addresses the problem of the slow convergence of the steepest descent methods. As we can see in fig. (5.3) steepest descent finds the minimum by taking steps

along the same directions as in previous steps. [118]. The rough idea behind conjugate gradient algorithms is that instead of using each time the orthogonal direction given by steepest descent, we can use a new direction constructed as a linear combination of the current and the previous directions and therefore reduce the iterations necessary to reach the minimum

More precisely, starting from the point $\mathbf{x}_0$ and moving along the direction $\mathbf{P}_0 = -\mathbf{G}(\mathbf{x}_0)$ given by steepest descent for the first step we get to the point $\mathbf{x}_1$. For the next iteration instead of the steepest descent direction $-\mathbf{G}(\mathbf{x}_1)$ we will move along a direction.

$$\mathbf{P}_1 = -\mathbf{G}(\mathbf{x}_1) + \gamma \mathbf{P}_0 \tag{5.4}$$

Which is the conjugate direction. The results are given in fig.(5.4). The scalar parameter γ is given by Fletcher-Reeves [118] as

$$\gamma_{i+1} = \frac{\mathbf{G}(\mathbf{x}_{i+1})^T \cdot \mathbf{G}(\mathbf{x}_{i+1})}{\mathbf{G}(\mathbf{x}_i)^T \cdot \mathbf{G}(\mathbf{x}_i)} \tag{5.5}$$

or by Polak-Ribière, as

$$\gamma_{i+1} = \frac{\mathbf{G}(\mathbf{x}_{i+1})^T \cdot (\mathbf{G}(\mathbf{x}_{i+1}) - \mathbf{G}(\mathbf{x}_i))}{\mathbf{G}(\mathbf{x}_i)^T \cdot \mathbf{G}(\mathbf{x}_i)}. \tag{5.6}$$

Finally, we present the pseudo algorithm for conjugate gradient method using the Polak-Ribière, approach for γ.

Algorithm 1 Conjugate Gradient Algorithm, Polak and Ribière approach [128].

initialise:
$i = 0$;
$\mathbf{G}_0 = \nabla h(\mathbf{x}_0)$;
$\mathbf{P}_0 = -\mathbf{G}(\mathbf{x}_0)$;
repeat
  find: $\lambda_i := \arg\min_\lambda \{\mathbf{x_i} + \lambda\ \mathbf{P}_i\}$ (Line search);
  set: $\mathbf{x_{i+1}} := \mathbf{x_i} + \lambda_i\ \mathbf{P}_i$
  calculate :
  $\mathbf{G}_{i+1} = \nabla h(\mathbf{x}_{i+1})$;
  $\gamma_{i+1} = \frac{\mathbf{G}_{i+1}^T \cdot (\mathbf{G}_{i+1} - \mathbf{G}_i)}{\mathbf{G}_i^T \cdot \mathbf{G}_i}$
  set:
  $\mathbf{P}_{i+1} = -\mathbf{G}_{i+1} + \gamma_{i+1}\mathbf{P}_i$
  $i = i + 1$
until h reaches minimum

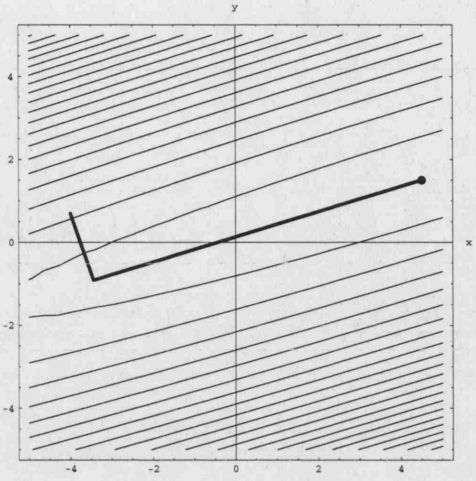

Figure 5.4: The method of conjugate gradient

5.4 Newton method

The Newton method is motivated by the first few terms of the Taylor series of function h in the vicinity of a minimum. The Taylor series of $h(\mathbf{x})$ about the point $\mathbf{x_0}$ is given by:

$$h \approx \hat{h}(\mathbf{x}) = h(\mathbf{x_0}) + h'(\mathbf{x_0})(\mathbf{x} - \mathbf{x_0}) + \frac{1}{2}h''(\mathbf{x_0})(\mathbf{x} - \mathbf{x_0})^2 + \dots \tag{5.7}$$

Keeping terms only up to the second order, the minimum of $\hat{h}$ will be at the point where :

$$\hat{h}'(\mathbf{x}) = 0 \Rightarrow h'(\mathbf{x_0}) + h''(\mathbf{x_0})(\mathbf{x} - \mathbf{x_0}) = 0, \tag{5.8}$$

which could be used to calculate the iterative step.

$$\mathbf{x_{i+1}} = \mathbf{x_i} - \left(h''\left(\mathbf{x_i}\right)\right)^{-1} h'\left(\mathbf{x_i}\right) \tag{5.9}$$

In (5.9), we used the assumption that the second derivative (the Hessian) (h'') exists and is invertible. A fact that is indeed true for the our example function h (5.1), since:

$$h'' = \begin{pmatrix} \frac{\partial^2 h}{\partial x^2} & \frac{\partial^2 h}{\partial x\, \partial y} \\ \frac{\partial^2 h}{\partial y\, \partial x} & \frac{\partial^2 h}{\partial y^2} \end{pmatrix} = \begin{pmatrix} 2 & -6 \\ -6 & 20 \end{pmatrix} \tag{5.10}$$

and

$$(h'')^{-1} = \frac{1}{\det(h'')} \begin{pmatrix} \frac{\partial^2 h}{\partial y^2} & -\frac{\partial^2 h}{\partial x\, \partial y} \\ -\frac{\partial^2 h}{\partial y\, \partial x} & \frac{\partial^2 h}{\partial x^2} \end{pmatrix} = \begin{pmatrix} 5 & 1.5 \\ 1.5 & 0.5 \end{pmatrix} \tag{5.11}$$

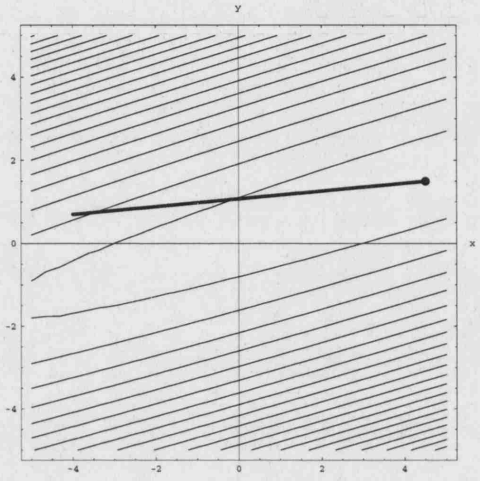

Figure 5.5: The Newton method

We should notice that (5.8) is based on a sometimes crude approximation that any function has a quadratic behaviour in a region around a point $\mathbf{x}$. Therefore, Newton method will converge to the minimum with one only step only in the special case of a quadratic h (see fig. (5.5)). For the more general case Newton method will need many iterations until quadratically converge, $\frac{(h(\mathbf{x_{i+1}}))^2}{(h(\mathbf{x_i}))^2} < \alpha$ for $0 < \alpha < 1$, to the minimum.

5.5 Line search

Line search algorithms are a common technique for most of the optimisation algorithms that use gradient information. That is due to the fact that gradient algorithms , e.g.the Newton method, are based on an linearisation of the otherwise non-linear functional (h) in a small area around its current state $\mathbf{x}$. Therefore the computed minimisation step $\mathbf{P}_i$ could be too long and the actual minimum be missed. Line search works on optimising the one-dimensional functional

$$\beta(\lambda_i) = h\left(\mathbf{x}_i + \lambda_i \mathbf{P}_i\right) \tag{5.12}$$

with respect to λ_i when a current point $\mathbf{x}_i$ and the descent direction $\mathbf{P}_i$ for h are given. Finding λ_i and setting

$$\mathbf{x}_{i+1} = \mathbf{x}_i + \lambda_i \mathbf{P}_i \tag{5.13}$$

provides the next state point $\mathbf{x}_{i+1}$.

5.5.1 Backtracking

A simple line search algorithm that we are going to use in the constraint minimisation calculations later, is *backtracking*. It seems common sense to require that $h(\mathbf{x}_{i+1}) < h(\mathbf{x}_i)$ but according to [63, 65], this simple condition alone does not guarantee that $\mathbf{x}_i$ will converge to the minimum of h. The main problem that we may encounter is the achievement of very small decrease in values of h in respect to the length of the steps. We can fix that be requiring that the average rate of decrease from $h(\mathbf{x}_i)$ to $h(\mathbf{x}_{i+1})$ be at least some prescribed fraction of the initial rate of decrease in this direction, [63], that is, we pick a $c \in (0,1)$ and chose a λ_i so that $h(\mathbf{x}_i + \lambda_i \mathbf{P}_i) \leq h(\mathbf{x}_i) + c\,\lambda_i\,\nabla h(\mathbf{x}_i) \cdot \mathbf{P}_i$. This is known as the *sufficient decrease* condition from Wolfe [65]. The sufficient decrease condition alone is still not sufficient since there is still the problem of the steps being very small relative to the initial rate of decrease of h, [63]. However, if the algorithm chooses the candidate values of λ_i appropriately, as in the backtracking algorithm, given in the pseudo code following, then it can give satisfactory results according to [65].

Algorithm 2 Backtracking line search

1: **set:** $\tilde{\lambda} > 0; \quad \sigma, c \in (0,1);$
2: **set:** $\lambda = \tilde{\lambda};$
3: **repeat**
4: **set:** $\lambda = \sigma * \lambda;$
5: **until** $h(\mathbf{x}_i + \lambda \mathbf{P}_i) < h(\mathbf{x}_i) + c\,\lambda\,\nabla h(\mathbf{x}_i) \cdot \mathbf{P}_i$
6: **set:** $\lambda_i = \lambda$

The usual values set for $c = 10^{-4}$ and $\sigma = 0.5$, while the initial step length is chosen $\tilde{\lambda} = 1$.

5.5.2 Quadratic fit

Through experiments with several line search algorithms in the relevant bibliography [97, 118, 65] we decided to use a *quadratic fit* line search method. The general idea is that if we can fit a quadratic approximation $Q(\lambda) = a\lambda^2 + b\lambda + c$ to the function $\beta(\lambda)$ using three points $\lambda_1 < \lambda_2 < \lambda_3$ so that $\beta(\lambda_2) < min\{\beta(\lambda_1), \beta(\lambda_3)\}$, in order to calculate a, b and c, then

$Q(\lambda)$ will be convex and its unique minimum will be given by:

$$\hat{\lambda} = \frac{(\lambda_2^2 - \lambda_3^2)\beta(\lambda_1) + (\lambda_3^2 - \lambda_1^2)\beta(\lambda_2) + (\lambda_1^2 - \lambda_2^2)\beta(\lambda_3)}{2[(\lambda_2 - \lambda_3)\beta(\lambda_1) + (\lambda_3 - \lambda_1)\beta(\lambda_2) + (\lambda_1 - \lambda_2)\beta(\lambda_3)]} \tag{5.14}$$

The method used is summarised in the next pseudo algorithm.

Algorithm 3 Quadratic fit line Search

1: **1st part : define** $\lambda_1, \lambda_2, \lambda_3$
2: **initialise** $\lambda_1 = 0\,;$ $\lambda_3 = 2;$ $\beta(\lambda_1) = h\,(\mathbf{x}_i);$
3: **calculate** $\beta(\lambda_3);$
4: **if** $\beta(\lambda_3) < \beta(\lambda_0)$ **then**
5: **set:** $\lambda_2 = \lambda_3;$ $\beta(\lambda_2) = \beta(\lambda_3);$ $\lambda_3 = \lambda_3 * 2.0;$
6: **calculate** $\beta(\lambda_3);$
7: **while** $\beta(\lambda_3) < \beta(\lambda_2)$ **do**
8: **set:** $\lambda_1 = \lambda_2;$ $\beta(\lambda_1) = \beta(\lambda_2);$ $\lambda_2 = \lambda_3;$ $\beta(\lambda_2) = \beta(\lambda_3);$
9: **set:** $\lambda_3 = \lambda_3 * 2.0;$
10: **calculate** $\beta(\lambda_3);$
11: **end while**
12: **else**
13: **set:** $\lambda_2 = 0.5 * \lambda_3;$
14: **calculate** $\beta(\lambda_2);$
15: **while** $\beta(\lambda_2) > \beta(\lambda_1)$ **do**
16: **set:** $\lambda_3 = \lambda_2;$ $\beta(\lambda_3) = \beta(\lambda_2);$
17: **set:** $\lambda_2 = 0.5 * \lambda_3;$
18: **calculate** $\beta(\lambda_2);$
19: **end while**
20: **end if**
21: **2nd part : calculate min :** $\hat{\lambda}$
22: **calculate** $a = ((\beta(\lambda_1) - \beta(\lambda_3))/(\lambda_1 - \lambda_3) - (\beta(\lambda_1) - \beta(\lambda_2))/(\lambda_1 - \lambda_2))/(\lambda_3 - \lambda_2);$
23: **calculate** $b = (\beta(\lambda_1) - \beta(\lambda_2))/(\lambda_1 - \lambda_3) - a * (\lambda_1 + \lambda_3);$
24: **calculate** $\hat{\lambda} = -b/(2.0 * a);$

5.6 Constrained optimisation

In a constrained optimisation problem there are *a-priori* limitations on the parameter space of $\mathbf{x}$. The allowed values for $\mathbf{x}$ are determined by the *constraint functions*, often equalities or inequalities that define the boundaries of a *feasible area* for the optimisation variables. The success of the optimisation rely strongly on the satisfaction of the constraints. The traditional methods for optimisation under constraints, are mainly based on adding penalty terms in the objective

function for each constraint. Lets suppose that the constraints are equalities or inequalities :

$$C_i(\mathbf{x}) = 0 \tag{5.15}$$

or

$$B_j(\mathbf{x}) \geq 0 \tag{5.16}$$

For the formulation of the optimisation problem the set of equalities constraints are gathered in a constraints vector $\mathbf{C}(\mathbf{x})$:

$$\mathbf{C}^T(\mathbf{x}) = (C_1(\mathbf{x}), \ldots, C_m(\mathbf{x})). \tag{5.17}$$

The feasible area then will be all the values of $\mathbf{x}$ where:

$$\mathbf{C}(\mathbf{x}) = \mathbf{0}. \tag{5.18}$$

Using this notation we can use the Lagrangian function $\mathcal{L}$ to incorporate the equality constraints into the optimisation problem.

$$\mathcal{L}(\mathbf{x}, \lambda) = h(\mathbf{x}) - \lambda^T \cdot \mathbf{C}(\mathbf{x}) \tag{5.19}$$

The optimisation problem then becomes that of minimising the Lagrangian $\mathcal{L}(\mathbf{x}, \lambda)$. The values $\mathbf{x}$ and λ that minimise (5.19) will provide a solution $\mathbf{x}$ that minimises h and at the same time satisfy the constraints $\mathbf{C} = 0$. The constraints have been included and the problem can be solved by the standard techniques that we described in the previous sections using this time the gradient of the Lagrangian in respect to both $\mathbf{x}$ and λ. Each step calculates the new step for $\mathbf{x}$ as long as the update for λ.

The inequalities on the other hand can be dealt by several different ways. One known method is setting a barrier function, $b(\mathbf{x})$ as a penalty term for the objective function. The barrier function should be designed to increase sharply when $\mathbf{x}$ violates the inequality constraint and be close to zero for $\mathbf{x}$ that satisfy the inequality. By adding the barrier function to the objective, we could increase the optimisation cost when the inequality is violated and similarly decrease it when it is satisfied. This methodology will force the direction of proceeding to respect the inequality.

Despite the fact that barrier functions are a simple way to incorporate an inequality in to an optimisation problem, when the number of inequalities increases the construction and use of barriers becomes a laborious task. To cope with larger problems an active set method [42] is preferred for the inclusion of inequality constraints in to the optimisation problem. The active set method proceeds by partitioning the problem's inequality constraints into two sets: active (or sufficiently close to be deemed active for this iteration) and inactive. The inactive constraints are ignored for the next iteration. The active inequalities on the other hand are transformed to equalities. For example if

$$B_j(\mathbf{x}) \geq 0 \tag{5.20}$$

is violated, that is $B_j(\mathbf{x})$ is less that zero, we form a constraint,

$$B_j(\mathbf{x}) = p \Rightarrow B_j(\mathbf{x}) - p = 0 \tag{5.21}$$

by the use of a parameter p which is positive and slightly larger that zero. The new equality constraint included in the constraint vector $\mathbf{C}$, will force the proceeding of the minimisation to move to the direction that will deactivate the original inequality. The new point is selected by moving on the surface defined by the active inequalities and the equalities. The active set changes slowly; at each iteration the step is chosen so that at most one constraint is added to or dropped from the active set.

5.7 Constrained Optimisation in Orthogonal Spaces

The methods discussed construct powerful tools for the minimisation of a function. A complicated optimisation problem will always pose a hard task to any sophisticated algorithm, a "perfect" generic method does not exist. According to the complexity and the kind of constraints in a problem we can decide on the use of a specific technique or a combination of many methods to achieve a fast and low cost solution.

Solving a constrained optimisation problem can be considered as a combination of two things that should happen simultaneously, the minimisation of the objective function and the satisfaction of the constraints. Constrained optimisation in orthogonal spaces, [22, 46], is a method that can deal with enforcement of hard constraints without undue computational cost increase, while retaining the desirable convergence properties. This approach effectively decouples the prob-

lem into two, one of fitting the data according to the objective function and a second enforcing the constraints by decomposing each iteration into two steps.

1. Enforce the constraints by projecting the current state of our problem onto the constraints hypersurface. This involves solving the system of non linear equations by linearising them and taking Newton steps

2. Minimise the objective function by projecting its gradient onto the tangent subspace to the constraint surface and perform a line search in the direction of the projection, so that the resulting state does not digress too far away from the constraints surface.

In figure (5.6) we can see the result of this procedure in a simple two dimensional problem. That is, minimise

$$h(x, y) = (x - 0.3y)^2 + (y - 0.5)^2 \tag{5.22}$$

under the constraint that

$$C(x, y) = (\frac{x}{2})^2 + y^2 - 2 = 0 \tag{5.23}$$

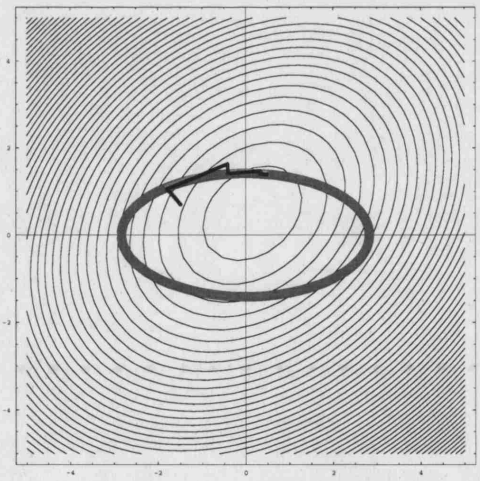

Figure 5.6: The constrained optimisation in orthogonal spaces for a simple 2D problem. The gray thick ellipsis represents the feasible region, the iso-contours represent the objective function. The solution starts from the point $\{x = -1.5, y = 0.7\}$) and following the thick black line terminates in the solution $\{0.476706, 1.39753\}$

The algorithm starts from the point $(x_0, y_0) = (-1.5, 0.7)$ and takes a Newton step $\delta \mathbf{s}^T = (\delta x, \delta y)$ so that

$$C(x_0 + \delta x, y_0 + \delta y) \approx 0 \tag{5.24}$$

if we note $\mathbf{C}'$ the gradient of C in respect to the two variables,

$$\mathbf{C}'(x_0, y_0) = \left[\frac{\partial C(x_0, y_0)}{\partial x}, \frac{\partial C(x_0, y_0)}{\partial y}\right] \tag{5.25}$$

According to the Newton algorithm

$$C(x_0 + \delta x, y_0 + \delta y) \approx C(x_0, y_0) + \mathbf{C}'(x_0, y_0) \cdot \delta \mathbf{s} \tag{5.26}$$

Since we want to satisfy the constraints we need to solve the equation,

$$\mathbf{C}'(x_0, y_0) \cdot \delta \mathbf{s} = -C(x_0, y_0), \tag{5.27}$$

and calculate the step $\delta \mathbf{s}$. Multiplying both sides with $\mathbf{C}'^T$,

$$\mathbf{C}'^T(x_0, y_0) \cdot \mathbf{C}'(x_0, y_0) \cdot \delta \mathbf{s} = -\mathbf{C}'^T(x_0, y_0) \cdot C(x_0, y_0), \tag{5.28}$$

or in a least squares formulation, we can rewrite:

$$\delta \mathbf{s} = -\left(\mathbf{C}'^T(x_0, y_0) \cdot \mathbf{C}'(x_0, y_0)\right)^{-1} \cdot \mathbf{C}'^T(x_0, y_0) \cdot C(x_0, y_0). \tag{5.29}$$

The step $\delta \mathbf{s}$ will propagate the current state perpendicular and close to the feasible curve $C(x, y) = 0$, which in our graph is represented as the thick grey curve.

Let, now (x_1, y_1) be the current state after the minimisation of the constraints, and $\mathbf{G} = \nabla f$ the gradient of the objective function at (x, y). The second half of the constraint optimisation in orthogonal spaces iteration would involve the minimisation of the objective function. The gradient $\mathbf{G}$ would provide such a direction as we show in the steepest descent algorithm. Knowing that the first half of the iteration forced the problem to move in a direction perpendicular to the constraints space, we want the next step to move in a direction tangent to the constraint curve towards the minimisation of the objective function, so that the effect of that step limits the violation of the constraints.

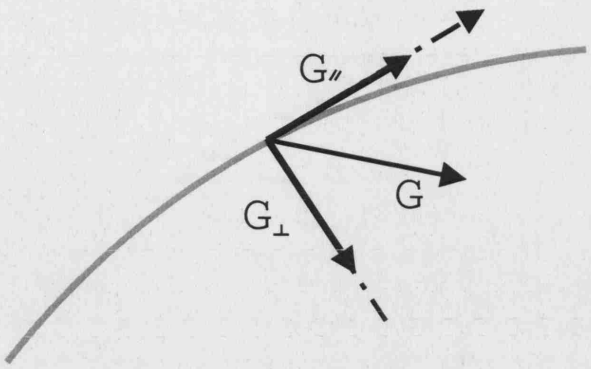

Figure 5.7: The projections of the gradient $\mathbf{G}$.

Following figure (5.7), we consider the projections of the gradient $\mathbf{G}(x_1, y_1)$ in the spaces tangent $\mathbf{G}_{\|}$ and perpendicular $\mathbf{G}_{\perp}$ to the constraints space $C(x, y) = 0$. Now, $\mathbf{G}_{\perp}$ has the direction of the previous step therefore could be expressed as a linear combination of the constraint normals, $\mathbf{C}'(x_0, y_0)\lambda$, where $\mathbf{C}'(x_0, y_0)$ was calculated for the Newton step. We solve the problem:

$$\mathbf{C}'(x_0, y_0)\lambda = \mathbf{G}_{\perp} \tag{5.30}$$

in respect to λ , in a least square sense, by multiplying both sides by $\mathbf{C}'^{T}$

$$\mathbf{C}'^{T}(x_0, y_0)\mathbf{C}'(x_0, y_0)\lambda = \mathbf{C}'^{T}(x_0, y_0)\mathbf{G}(x_1, y_1) \tag{5.31}$$

and getting

$$\lambda = (\mathbf{C}'^{T}(x_0, y_0)\mathbf{C}'(x_0, y_0))^{-1}\mathbf{C}'^{T}(x_0, y_0)\mathbf{G}(x_1, y_1) \tag{5.32}$$

$\mathbf{C}'(x_0, y_0)\lambda$ will be the perpendicular component $\mathbf{G}_{\perp}$, consequently for $\mathbf{G}_{\|}$:

$$\mathbf{G}_{\|} = \mathbf{G} - \mathbf{G}_{\perp} \Rightarrow \mathbf{G}_{\|} = \mathbf{G} - \mathbf{C}'(x_0, y_0)\lambda \tag{5.33}$$

The algorithm continues with a line search in the direction of $\mathbf{G}_{\|}$ which is the steepest descent for the projected gradient. A variation of the algorithm that has produced greater efficiency is to calculate the new direction, using a conjugate gradient algorithm, using a direction which will be a linear combination of all the previous $\mathbf{G}_{\|}$ directions.

Back to the problem in figure (5.6) we can see that three iterations later the minimisation

is achieved and the solution $(0.342444, 1.40523)$ lies upon the feasible area for the specific constraint in the area closest to the minimum of the objective function.

5.8 Optimisation and nonlinear least squares problems

In chapter 2 we discussed that the least squares minimisation is of primary importance in the solution of a nonlinear inverse problem. Methods for solving such problems are iterative, and each iteration requires the solution of a least squares problem. The nonlinear least squares problem is a special case of the general unconstrained optimisation problem for the minimisation of the squared distance between nonlinear functionals:

$$f_{\min} = \min_f \arg \Xi(f) \text{ where } \Xi(f) = \|g - \mathcal{K}(f)\|^2. \tag{5.34}$$

Where g and $\mathcal{K}(f)$ are defined over $\mathbb{R}^N$ while $f \in \mathbb{R}^M$. In the following we assume that $\Xi(f)$ is twice differentiable and therefore can be approximated by the second degree Taylor expansion around the current estimate $f^{(k)}$:

$$\Xi(f) \approx \tilde{\Xi}(f) = \Xi(f^{(k)}) + \left(\frac{\partial \Xi}{\partial f}(f^{(k)}) + \frac{1}{2}(f - f^{(k)})^T \frac{\partial^2 \Xi}{\partial f^2}(f^{(k)})\right)(f - f^{(k)}) \tag{5.35}$$

For the approximation $\tilde{\Xi}(f)$ we can derive:

$$\frac{\partial \tilde{\Xi}}{\partial f}(f^{(k+1)}) = \frac{\partial \Xi}{\partial f}(f^{(k)}) + (f^{(k+1)} - f^{(k)})^T \frac{\partial^2 \Xi}{\partial f^2}(f^{(k)}). \tag{5.36}$$

The next update $f^{(k+1)}$ will be found in the descent direction of $\tilde{\Xi}(f)$. When $\tilde{\Xi}(f)$ is at the minimum $f^{(k+1)}$ we have :

$$\frac{\partial \tilde{\Xi}}{\partial f}(f^{(k+1)}) = 0 = \frac{\partial \Xi}{\partial f}(f^{(k)}) + (f^{(k+1)} - f^{(k)})^T \frac{\partial^2 \Xi}{\partial f^2}(f^{(k)}) \tag{5.37}$$

Assuming that the Hessian matrix $\frac{\partial^2 \Xi}{\partial f^2}$ is invertible, and rearranging (5.37) we get:

$$f^{(k+1)} = f^{(k)} - \left(\frac{\partial^2 \Xi}{\partial f^2}(f^{(k)})\right)^{-1} \frac{\partial \Xi}{\partial f}(f^{(k)}) \tag{5.38}$$

From (5.34) the gradient $\frac{\partial \Xi}{\partial f} \in \mathbb{R}^M$ will be:

$$\frac{\partial \Xi}{\partial f}(f^{(k)}) = -2\left(\frac{\partial \mathcal{K}}{\partial f}(f^{(k)})\right)^T (g - \mathcal{K}(f^{(k)})) \tag{5.39}$$

The Hessian matrix $\frac{\partial^2 \Xi}{\partial f^2} \in \mathbb{R}^{M\times M}$ has then the form :

$$\frac{\partial^2 \Xi}{\partial f^2}(f^{(k)}) = -2\left(\sum_{i=1}^{N}(g_i - \mathcal{K}_i(f^{(k)}))\frac{\partial^2 \mathcal{K}_i}{\partial f^2}\right) + 2\left(\frac{\partial \mathcal{K}}{\partial f}(f^{(k)})\right)^T \left(\frac{\partial \mathcal{K}}{\partial f}(f^{(k)})\right) \tag{5.40}$$

using equations (5.38)-(5.40) and introducing the notation:

$$J_k = \frac{\partial \mathcal{K}}{\partial f}(f^{(k)}), \tag{5.41}$$

$$\mathbf{S}_k = -\left(\sum_{i=1}^{N}(g_i - \mathcal{K}_i(f^{(k)}))\frac{\partial^2 \mathcal{K}_i}{\partial f^2}\right) \tag{5.42}$$

we arrive in the Newton-Raphson iteration formula

$$f^{(k+1)} = f^{(k)} + \left(\mathbf{S}_k + J_k^T J_k\right)^{-1} J_k^T (g - \mathcal{K}(f^{(k)})) \tag{5.43}$$

In practice the computations involved in the Hessian of a large problem can be prohibitively costly and slow. Therefore, there is a variety of different approximations that can be derived from (5.43). For example, replacing the whole $\left(\mathbf{S}_k + J_k^T J_k\right)$ term with the identity matrix I we get the Landweber method [18].

$$f^{(k+1)} = f^{(k)} + J_k^T (g - \mathcal{K}(f^{(k)})) \tag{5.44}$$

5.8.1 Gauss-Newton method

Ignoring the term $\mathbf{S}_k$ leads to the most commonly used Gauss-Newton iteration.

$$f^{(k+1)} = f^{(k)} + \left(J_k^T J_k\right)^{-1} J_k^T (g - \mathcal{K}(f^{(k)})) \tag{5.45}$$

We can reach this formula also by approximating the system (5.34) in the vicinity of a given point $f^{(k)}$ with the first order Taylor series:

$$\breve{\Xi}(f) = \Xi(f^{(k)}) + J_k^T(f - f^{(k)}), \tag{5.46}$$

and solve instead the linear least squares problem:

$$\min_f \|\Xi(f^{(k)}) + J_k^T(f - f^{(k)})\|^2 \tag{5.47}$$

The Gauss-Newton algorithm has good local convergence only when the second derivative $\frac{\partial^2 \Xi}{\partial f^2} \approx 0$ or the residual $\|g - \mathcal{K}(f)\|^2$ is small [97, 18]. We should notice also that the method is similar to the general nonlinear optimisation Newton method that we described in section (5.4).

5.8.2 Levenberg-Marquardt method

Replacing, S_k with a control term $\lambda_k \mathrm{I}$ leads to the Levenberg-Marquardt iteration.

$$f^{(k+1)} = f^{(k)} + \left(J_k^T J_k + \lambda_k \mathrm{I}\right)^{-1} J_k^T(g - \mathcal{K}(f^{(k)})) \tag{5.48}$$

The Levenberg-Marquardt method was put together by Marquardt [78] based on a suggestion of Levenberg for varying smoothly between the extremes of the Newton-Gauss method ($\lambda_k \to 0$) and the steepest descent ($\lambda_k \to \infty$). The choice for λ_k is based on estimating a maximum neighbourhood where the linearised Taylor series will give an adequate estimate for the non-linear model. Outside this neighbourhood λ_k will turn to the steepest descent direction which is known for fast convergence in the first few iterations. A typical Levenberg-Marquardt algorithm is given from [97]. Noticeably the Levenberg-Marquardt method doesn't depend on a line search in each iteration for good convergence.

Algorithm 4 Levenberg-Marquardt Algorithm

initialise:
$f^{(k)} = f^{(0)}$;
λ_k to some modest value e.g. $\lambda_k = 0.001$;.
repeat
calculate: $\Xi(f^{(k)})$;
calculate: $f^{(k+1)}$ from equation (5.48)
if $\Xi(f^{(k+1)}) \geq \Xi(f^{(k)})$ **then**
set: $\lambda_k = 10 * \lambda_k$;
else
set: $\lambda_k = 10^{-1} * \lambda_k$;
end if
until $\Xi(f^{(k+1)})$ reaches a suitably small value

5.9 Conclusions

This chapter discusses the optimisation of a nonlinear scalar function. Starting from the definitions of the problem and the necessary terminology used in optimisation theory and proceeded with a brief review of the most commonly used methods.

The first method reviewed was steepest descent. We illustrated that this method shows fast convergence in the first few iterations but it slows down once close to the minimum. Afterwards, the conjugate gradient method was presented to accommodate for the slow convergence of steepest descent by removing the unnecessary multiple steps along the same directions. The Taylor-series based methods were presented with the Newton method, which based on a linearised version of the nonlinear function shows good convergence once in the vicinity of the minimum but large divergence when started far from it.

Implicit in all the method mentioned so far is a line search method to determine an acceptable step size. An exact line search using a quadratic fit and a non-exact based on the Wolfe conditions and backtracking were reviewed and given in pseudo-algorithm format.

The introduction of constraints, that restrict the feasible region of the optimisation problem was treated by a brief review of the Lagrangian method for equalities and barrier functions or active sets for inequalities. Orthogonal spaces are also used for constrained minimisation by decoupling the problem into two parts, one for the minimisation of the objective function and one for the satisfaction of the constraints.

Finally, the last section of this chapter is dedicated to the minimisation of least squares func-

tionals, a theme with paramount importance in the inversion theory. The Taylor series of second degree was used in this case, leading to the Newton-Raphson method that require second derivatives. Since the computation of the Hessian is a costly procedure, alternative methods using steepest descent and the Gauss-Newton iteration are employed suggesting the Levenberg-Marquardt iteration that comes to combine the advantages of the two methods.

There is a great deal of methods that could be used for the minimisation of constrained or unconstrained functionals. In this chapter we covered the ones that we encounter in the duration of this work. Since optimisation is such an important discipline in the world of numerics we feel that there is always space for improvement in our future work.

Chapter 6

Parametric Description of Surfaces

6.1 Introduction

Since the evolution of reliable digital imaging methods for the medical world, the acquisition and analysis of three dimensional images of human organs has become a common practice for the diagnosis and treatment of patients. Within the domain of medical imaging, MRI and CT have become the prominent methods for acquiring structural information about organisms in a non-destructive way.

However, the data acquired constitute a very raw representation of the anatomical structures into lists of three dimensional pixels or *voxels* as they are commonly called. This low level representation, can provide a good base for the visual examination by doctors but lacks the structural description necessary for an automatic registration and identification system. Some problems, shape based reconstructions being one of them, could benefit significantly from a description of anatomical structures, using a small number of parameters. Therefore, there is a need for transformation of the raw data to some compact and flexible description. Moreover, several anatomical structures of the human body do not have any structural holes on their surface (e.g. the brain), therefore possess the genus of a sphere. From topology we know that for a closed object that is topologically equivalent to a sphere, there exists a mapping function, a *homeomorphism*, that can project the surface of that object upon a sphere's surface S^2.

6.2 Spherical Parameterisation

In practice the procedure that starts from a discrete representation of a closed surface M, e.g. mesh V of connected vertices $\mathbf{v}$, and forms a mapping $\upsilon : S^2 \longrightarrow M$ from the unit sphere S^2

to the surface M, is called *spherical parametrisation.* The mapping is defined by assigning each vertex $\mathbf{v}$ a parametrisation $\mathbf{s} = v^{-1}(\mathbf{v})$. Then, each mesh edge is mapped to a spherical great circle arc and each quadrilateral or triangle is mapped to a spherical quadrilateral or spherical triangle respectively defined by those arcs.

In the 1995 paper by C. Brechbüchler et al [23], a method that can produce an approximation to such a mapping was described using voxel volumetric data and utilising the uniform quadrilateral data structures in a non-linear optimisation problem. In the recent year the medical community became familiar with a cortical surface-based analysis system from [39], where a combined flattening and inflation procedure is applied on cortical surfaces. Starting from high density triangular surface meshes of the cortex a morphing is defined to the surface of a sphere utilising unfolding of the sulci surface using oriented areas and minimisation of the metric distortions.

A few years later, parametrisation appears to be a gaining interest as a topic, especially in the area of computer graphics, where many applications have been found in shape analysis [47, 119, 99], compression [111] and mesh morphing [77]. Recently, in 2003, in [36] a spherical parametrisation method using triangular surface meshes was presented with applications in texture mapping. The algorithm proposed uses successively simplification of a surface mesh by using vertex collapses to a progressive mesh sequence, until it reaches a tetrahedron. Then the tetrahedron is embedded on a sphere and a refinement brings the surface back to its original resolution introducing spherical coordinates for the re-introduced vertices and optimising their location in order to minimise distortions.

Borrowing elements from the work described in [23], this chapter describes the method used for the creation of a mapping function from a sphere-like anatomical structure upon a unit sphere. By creating a continuous and invertible mapping, from every point on an anatomical object's surface to one and only one point on the sphere, functions that usually live on the sphere's surface can now be expressed upon the object. An example of such basis functions are spherical harmonics. We will present a technique that creates a description of the objects surface using a small number of spherical harmonics coefficients. The description of the object will be parametric inheriting the two spherical parameters ϑ andφ. In the next pages we are going to present in detail the method used for the construction of such a parameterisation. In addition, some relevant applications and interesting properties of the parametric representation

will be discussed.

6.3 Extraction of the surface

Our main interest lies in the use of prior acquired geometric data in order to create a sufficiently, realistic model of the different regions of an anatomical structure. Following the numerous applications of head and brain imaging we decided to use the head's geometry as a test bed. We can use good resolution MRI or CT-scan images as prototypes. Both those imaging modalities use voxels maps to create an image. We are going to use those images to extract the boundary surface of the structure, fig. (6.1).

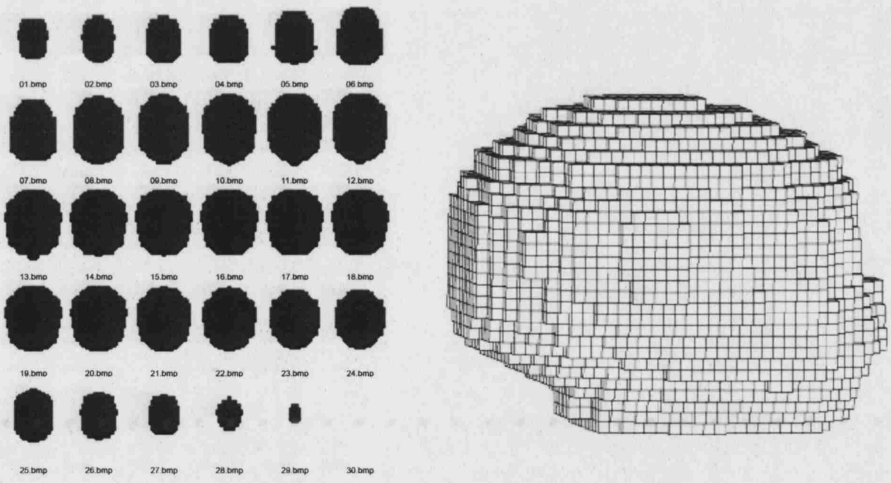

Figure 6.1: Segmented MRI data of a baby's scalp as bitmap slices(left) and as voxel volume (right). Thanks to Richard Bayford, Middlesex University.

For a successful mapping on the sphere, it is very important to extract a valid representation of the surface of the object. The current algorithm copes with closed surfaces with six-connectivity between the voxels, as seen in fig (6.2).

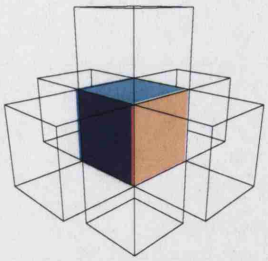

Figure 6.2: Six-connectivity for a voxel.

A simple algorithm [126] that reads through the binary voxel image and extracts the surface faces from all the voxels of the object (mapped as 1's in the binary map) is used to create a list of the voxel faces. In this list, the boundary faces are mentioned once, while the faces inside the volume are mentioned twice. We extract only the surface faces, mentioned only once in the above list. Then in anticlockwise order we extract the vertices that define those boundary faces. The surface is now stored as a lists of vertices $\{\mathbf{v}_1, \ldots, \mathbf{v}_n\}$, where $\mathbf{v}_j = \{x_j, y_j, z_j\}$. Information on the connectivity net of the boundary vertices is saved as well in a list $\{\mathbb{B}_1, \ldots, \mathbb{B}_n\}$, where $\mathbb{B}_j$ is the set of the $\mathrm{L}_{\mathbb{B}j}$ indices for the direct neighbours of the node $\mathbf{v}_j$ on the surface's net, in an anticlockwise manner as observed from outside.

6.4 Initial mapping

Having extracted a surface from the voxel object, we are interested in mapping this net of connected nodes on the surface of a sphere. Since the voxel faces are squares the mapped objects would be considered as spherical quadrilaterals. There are two essential constraints that should be taken in respect for a well posed mapping.

- The sphere should be completely covered with spherical quadrilaterals
- The spherical quadrilaterals should not overlap

This initial mapping is clearly a distribution of spherical coordinates ϑ and φ to the nodes consisting the surface net. Longitude should range $0 \leq \varphi \leq 2\pi$ and latitude $0 \leq \vartheta \leq \pi$. A simple way to achieve such mapping could be by taking the projection of a radial function $\mathbf{r}(\vartheta, \varphi)$ on the surface of the object. However, this trivial mapping is only valid for *star-shaped*

objects. That is, objects that have at least one internal point that can be directly connected with a straight line to any of the boundary points.

Since our application exceeds the family of star-shapes, a harmonic distribution of the extracted surface's net onto the sphere's surface was chosen instead of a direct radial function. We use the discrete solution of the Laplace equation (6.1) for the steady state heat distribution T to assign initial parameters to the surface vertices in agrement with the constraints for the well posed mapping.

$$\nabla^2 T = \frac{\partial^2 T}{\partial x^2} + \frac{\partial^2 T}{\partial y^2} + \frac{\partial^2 T}{\partial z^2} = 0 \tag{6.1}$$

The implementation will be done in two separated steps, one for each spherical parameter.

6.4.1 Latitude ϑ from diffusion

Since latitude ϑ should grow smoothly from 0 to π we assign two poles among the nodes. Experiments have shown that the selection of the poles does not bias the mapping function, but in order to reduce the computational effort later on, we choose the two nodes with the greatest and smallest coordinates of x. Latitude values ϑ should grow smoothly from 0 at the *North pole* to π at the *South pole*. We rearrange the list of vertices $\{\mathbf{v}_1, \ldots, \mathbf{v}_n\}$ so that he North pole is noted $\mathbf{v}_1$ and the South pole $\mathbf{v}_n$.

Latitude should not be considered as a free variable, but rather as an unknown function, of the location of the vertex on the object, for which we are looking. Following the heat conductive paradigm the problem can be portrayed as: we heat the South pole to temperature π, simultaneously cool the North pole to temperature 0 and ask for the stationary temperature distribution on the heat-conducting surface. The problem of creating a harmonic distribution of ϑ then can be formed as the continuous problem of the surface Laplacian equation,

$$\nabla^2 \vartheta = 0 \tag{6.2}$$

with Dirichlet boundary conditions for the poles,

$$\vartheta_{Northpole} = 0, \tag{6.3}$$

$$\vartheta_{Southpole} = \pi \tag{6.4}$$

The discrete case of the Laplace's equation (6.1) suited to the fact that we only work with the vertices is approximated by finite second differences of the available direct neighbours $\mathbb{B}_j$ of a vertex $\mathbf{v}_j$.

Which can be formed in a sparse set of linear equations

$$\mathrm{A}\,\vartheta = \mathbf{b} \tag{6.5}$$

If we note n the number of nodes in the net, then A is a $(n-2) \times (n-2)$ (poles excluded) symmetric connectivity matrix with elements calculated by:

$$a_{i,j} = \begin{cases} \mathrm{L}_{\mathbb{B}i}, & \text{if } j = i \ ; \\ -1, & \text{if } j \in \mathbb{B}_i \ ; \\ 0, & \text{otherwise.} \end{cases} \tag{6.6}$$

The vector b expresses the Dirichlet boundary conditions with elements:

$$b_j = \begin{cases} \pi, & \text{if } j \in \mathbb{B}_{Southpole}; \\ 0, & \text{otherwise.} \end{cases} \tag{6.7}$$

The system (6.5) is solved using a generic conjugate gradient solver .

6.4.2 Longitude φ from diffusion

Unlike latitude, longitude is a periodic (cyclic) parameter. Following longitude as we walk around the sphere, in the clockwise direction when seen from the South pole, we watch it increasing smoothly until we reach the line of discontinuity where it leaps back by 2π. This line connects the two poles and it is not necessarily straight. One good parallelism is the terrestrial date line, which is not a meridian but a jagged line of the 24-hour discontinuity. On the sphere surface net, we define the date line as the path with the steepest latitude ascent from the North to the South pole. In the same way as in the geographic parallelism, longitude values crossing the date line from west to east are decreased by 2π while values spreading towards the west are incremented by 2π. For the poles, longitude is set arbitrary to zero, and generally, poles are removed from the distribution of longitude values. The node's net during this procedure has the topology of a tube.

Harmonic distribution of the φ parameter is implemented by the solution of the Laplace's equation, this time with a date line. The values of longitude that are neighbouring to the date line on the east are enforced by -2π and those on the west are treated with $+2\pi$. The new linear system,

$$\mathrm{A}'\,\varphi = \mathrm{b}',$$

is singular having dependent equations due to the periodicity of longitude, $\varphi + 2\pi = \varphi$. To convert it to a regular one, we specify an arbitrary longitude value for the second node by introducing the equation $2\varphi_2 = 0$.

Our approach to the solution of the Laplace's equation is similar to one used for latitude. Therefore, the connectivity information from matrix A, from the latitude calculation, can be used with some modifications. Information about the neighbours of the poles is removed and the diagonal is recalculated. The elements of the new matrix A′ will be:

$$a'_{i,j} = \begin{cases} \mathrm{L}_{\mathbb{B}i}, & \text{if } j = i \quad \text{(without considering the poles } \mathbf{v}_1 \text{ and } \mathbf{v}_n\text{)}\,; \\ -1, & \text{if } j \in \mathbb{B}(i)\,; \\ 0, & \text{otherwise.} \end{cases} \tag{6.8}$$

Finally, $a'_{2,2}$ is incremented by $+2$ to account for the longitude regularisation term $2\varphi_2 = 0$.

In [23], the algorithm (5) is given that initially defines the steepest ascent latitude path from the North to the South pole. Then sets up the new constants vector $\mathbf{b}'$ by following this path and enforcing the $+2\pi$ to direct neighbours on the west of the date-line nodes .

In figure (6.3) we can see the initial mapping of the surface of the voxel object projected upon a sphere. As expected the initial mapping creates a parametrisation that covers the whole area of the sphere. We notice that the shape of the spherical quadrilaterals is quite distorted from that of the square. Also the size of each spherical quadrilateral varies unlike the original squares on voxels that all had size one.

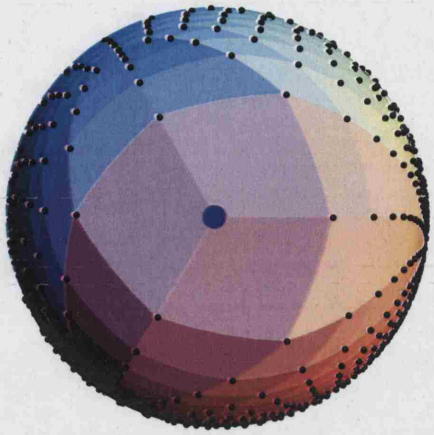

Figure 6.3: The initial mapping of the head surface form figure (6.1) on the sphere. The nodes are denoted by black dots, the North Pole is also visible as a big dot.

Algorithm 5 Calculate b'

Initialise:
`NorthPole` : =1;
`SouthPole` : = n;
`PreviousNode` : = `NorthPole`;
`Here` : = 2;
$\max \vartheta := 0$;
while `Here` != `SouthPole` **do**
  for all $j \in \mathbb{B}_{\texttt{Here}}$ **do**
    if $\vartheta_j > \max \vartheta$ **then**
      $\max \vartheta = \vartheta_j$;
      `NextPosition` = Position of j in the list $\mathbb{B}_{\texttt{Here}}$;
    end if
    if j = `PreviousNode` **then**
      `PrevPosition` = Position of j in list $\mathbb{B}_{\texttt{Here}}$;
    end if
    for all nodes g in the list $\mathbb{B}_{\texttt{Here}}$ anticlockwise from `PrevPosition` to `NextPosition` **do**
      Add 2π to $b'[g]$
      Subtract 2π from b'[`Here`]
    end for
    `PreviousNode` : = Here;
    `Here` :=`NextPosition`
  end for
end while

The harmonic distribution of the surface's net on the sphere succeeded in projecting a non-

star-shaped surface on the sphere but introduced distortion. The parametrisation is not yet well defined. This calls for some fixing of the vertices locations on that initial mapping. In the next sections we are going to examine how we achieved that with the help of constrained optimisation techniques introduced in chapter 5 .

6.5 Optimisation of the mapping

We are looking for the minimisation of the distortions created by the initial mapping so that a one-to-one relationship will be established between the voxel surface and the sphere. More precisely we want the spherical quadrilaterals to approximate spherical squares, with equal spherical areas each. The following paragraphs, define the notions of variables, objective function and constraints in the context of this optimisation problem.

6.5.1 Variables

The variables of the optimisation problem are the coordinates of the projected vertices on the surface of the sphere. We note as $\mathbf{s}_j$ the projection on the sphere of the vertex v_j. The initial mapping produces spherical coordinates $\{\vartheta, \varphi\}$ for each of the vertices. We found that for the purposes of the optimisation algorithm we should transform them to Cartesian $\{x, y, z\}$, in order to avoid the effects of cyclic periodicity.

6.5.2 Objective function

The target of the optimisation is defined as the minimisation of the distortions of the mapped surface's net on the sphere. Ideally, this can be modelled as a formulation of the mapped spherical quadrilaterals similar to the square faces of the voxels. Conceptional this equals to the preservation of the angles and sides on the faces throughout the mapping. Nevertheless, only in exceptional cases it can be achieved perfectly. e.g. the case of an object that consists of one voxel. Consequently, we try to minimise the distortions by reaching the best possible approximation of spherical squares for the spherical quadrilaterals.

We notice that from all the possible spherical quadrilateral formations covering a given area, the spherical square has the property of the minimum circumference. A side of the spherical quadrilateral noted s_{ij} is defined by two nodes $\mathbf{s}_i$ and $\mathbf{s}_j$, and is the segment of the great circle that connects those two nodes. The length $\|s_{ij}\|$ of a spherical quadrilateral side will have a range from 0 to π. Minimising the length of the edge s_{ij} of a quadrilateral, maximises

$\cos(\|s_{ij}\|)$. Since the nodes belong on a unit sphere centred on $(0,0,0)$, $\cos(\|s_{ij}\|)$ will be given from the dot product of their vectors $\mathbf{s}_i \cdot \mathbf{s}_j$.

We define the objective function $f(\mathbf{s})$ using the sum of $\cos(\|s_{ij}\|)$, when $\|s_{ij}\|$ ranges through the lengths of all the edges s_{ij} on the net of nodes. That is for every node i all the vertices $j \in \mathbb{B}_i$ direct neighbours of i.

$$f(\mathbf{s}) = \frac{1}{2} \sum_{i \in V} \sum_{j \in \mathbb{B}_i} \cos(\|s_{ij}\|) \tag{6.9}$$

The $\frac{1}{2}$ factor was introduced since each side s_{ij} in this expression is mentioned twice. The goal of optimisation algorithms in general is to minimise a function, thus we set $-f(\mathbf{s})$ as the objective. By nature, the minimisation of this function punishes long edges and favours short ones, which is a desirable effect. Early attempts to minimise the objective function using unconstrained steepest descent methods were fruitless. The only force applied to the nodes was towards the direction that minimises the objective gradient. As a result, the nodes tend to merge in one point, creating distortion and unequal areas. Those results suggested that constraints should be applied.

6.5.3 Constraints

This section defines the two types of equalities and one inequality constraints used in the optimisation procedure.

Normalisation

The employment of Cartesian coordinates for the vertices created a virtual degree of freedom that allowed the nodes to move away from the unit sphere's surface. To compensate, we force the vectors pointing the vertices on the sphere to have unit length. In other words, the Euclidean norm of the coordinates of any vertex should be equal to one. Expressed as an equality constraint, for every node $\mathbf{s}_i$ with coordinates $\{x_i, y_i, z_i\}$ we have:

$$\|\mathbf{s}_i\| = 1 \Rightarrow \sqrt{x_i^2 + y_i^2 + z_i^2} = 1 \tag{6.10}$$

Initially, we established one equation for each vertex in the optimisation. Further experiments suggested that, we treat vector lengths by continuous projection whenever an optimisation step

is changing the variables. Each triple $\{x_i, y_i, z_i\}$ is normalised by dividing by $\|s_i\|$.

Preservation of Areas

The preservation of areas is the second goal of the optimisation. Voxel faces with equal areas should map to spherical quadrilaterals with equal areas. The entire surface of the unit sphere is equal to 4π, the number of faces is NoF. Therefore, each spherical quadrilateral should cover area equal to $4\pi/NoF$. We set one constraint for each face.

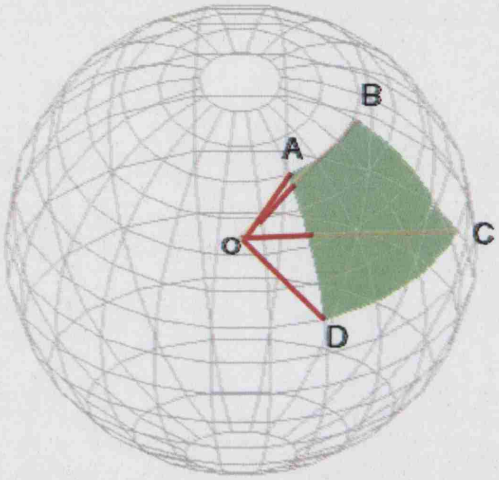

Figure 6.4: The spherical quadrilateral $\mathbf{Q}_m$ defined from the nodes A, B, C and D.

This requires a formula to express the area of the spherical quadrilateral. We refer to spherical trigonometry for the necessary background [123]. A spherical quadrilateral $\mathbf{Q}_m$, where m is an index over all the faces, is defined from four points on the surface of a sphere A, B, C and D (see figure (6.4)). Those points are joined by great circle arcs. A great circle is the trace of a plane passing through the centre of the sphere and the surface of the sphere. From spherical trigonometry, we know that the area of a spherical quadrilateral, defined by great circles, is given by the formula, [123]:

$$Area\,(\mathbf{Q}_m) = R^2(\hat{a} + \hat{b} + \hat{c} + \hat{d} - 2\pi) \tag{6.11}$$

Where $\hat{a}, \hat{b}, \hat{c}$ and $\hat{d}$, are respectively the spherical angles $\angle BCD$, $\angle CDA$, $\angle DAB$ and $\angle ABC$ of the spherical quadrilateral (6.4), and R the radius of the sphere. We will try to calculate the spherical angles, for example $\angle DAB$. The cosine formula from spherical trigonometry

defines that for the spherical $arcDB$, the great circle segment along the surface of the sphere that connects point D with point B, with length $arc\langle DB\rangle$ (measured in radians) is:

$$\begin{aligned}\cos(arc\langle DB\rangle) = \cos(arc\langle AD\rangle)\cdot\cos(arc\langle AB\rangle)+\\ +\sin(arc\langle AD\rangle)\cdot\sin(arc\langle AB\rangle)\cdot\cos(\angle DAB)\end{aligned} \tag{6.12}$$

so that,

$$\cos(\angle DAB) = \frac{\cos(arc\langle DB\rangle) - \cos(arc\langle AD\rangle)\cdot\cos(arc\langle AB\rangle)}{\sin(arc\langle AD\rangle)\cdot\sin(arc\langle AB\rangle)}. \tag{6.13}$$

From the cross product we also have the identity:

$$\sin(\angle DAB) = \frac{\|\mathbf{OA}\times\mathbf{OB}\|\times\|\mathbf{OA}\times\mathbf{OD}\|}{\|\mathbf{OA}\times\mathbf{OB}\|\cdot\|\mathbf{OA}\times\mathbf{OD}\|} \tag{6.14}$$

or,

$$\sin(\angle DAB) = \frac{[\mathbf{OA},\mathbf{OB},\mathbf{OD}]}{\sin(arc\langle AB\rangle)\cdot\sin(arc\langle AD\rangle)} \tag{6.15}$$

or,

$$\sin(\angle DAB) = \frac{\mathbf{OA}\cdot\mathbf{OB}\times\mathbf{OD}}{\sin(arc\langle AB\rangle)\cdot\sin(arc\langle AD\rangle)} \tag{6.16}$$

Having calculated the sine (6.16) and the cosine (6.13) of the angle, we make use of an *arctan* function to find the spherical angle $\angle DAB$.

$$\angle DAB = \arctan\left(\frac{\sin(\angle DAB)}{\cos(\angle DAB)}\right) \tag{6.17}$$

or,

$$\angle DAB = \arctan\left(\frac{\mathbf{OA}\cdot\mathbf{OB}\times\mathbf{OD}}{\cos(arc\langle DB\rangle) - \cos(arc\langle AD\rangle)\cdot\cos(arc\langle AB\rangle)}\right) \tag{6.18}$$

Now we can define one constraint equation for each spherical quadrilateral $\mathbf{Q}_m$. The equation is formed:

$$Area\,(\mathbf{Q}_m) - \frac{4\pi}{NoF}. \tag{6.19}$$

Enforcement of permissible spherical angles

The last constraint that we set is designed to prevent spherical angles becoming less than zero or greater than π. Consequently we need to constrain the spherical angles $\angle DAB$ to the interval $[0,\pi]$, which is similar to $\sin(\angle DAB) > 0$ and can be calculated from (6.16).

In early attempts of optimisation, inequality constraints were set with the aid of barrier functions, like

$$b(\angle DAB) = -\log(\angle DAB) + \log(\pi - \angle DAB) \tag{6.20}$$

which were added to the objective function (6.9) for each of the spherical angles. The specific barrier function, would act as a penalty term which would increase the optimisation cost exponentially if the angle $\angle DAB$ becomes too small (less than zero) or too large (greater then π). Therefore, the violation of one inequality would restrain the optimisation from following the direction that favours the violation. Experiments with the barrier function gave inefficient results and this technique was abandoned. The current optimisation algorithm uses an active set method for the inequalities. For every iteration all angles are checked for violation of the $[0, \pi]$ range and the violated inequalities are placed to an active set. For every active inequality, a corresponding equality

$$\sin(\angle DAB) = p \tag{6.21}$$

is included into the constraint vector. The parameter p is set to a small positive value e.g. $p = 0.2$ and is constant until the problem finishes. The active inequality $\sin(\angle DAB) > 0$ through the corresponding equality will drive $\sin(\angle DAB)$ towards zero. If a subsequent iteration satisfies the active inequality, the constraint is removed and the inequality is set back to the inactive set. The constraints that influence the direction of the optimisation at any point are the equalities and the active inequalities.

6.6 Optimisation Methodology

The size of the objects that we are dealing with in medical imaging applications as well as the complexity of the constraints that should apply for a good mapping posed a hard problem in the optimisation of the position of the nodes. We tried with many of the commonly used, standard methods for constraint optimisation, but the results were in most of the cases poor. In search for an efficient, fast and low computational cost method we adapted a version of the method described in [46] and [22] for constraint optimisation in orthogonal spaces, with an additional step of equal charged particle forces on the sphere to accelerate the positioning of the nodes. The conceptual model of the optimisation technique used is that of the nodes as charged particles on a sphere allowed to oscillate, while the forces from the constraints and the objective

function make sure that the model stays legitimate.

Algorithm 6 Optimisation Algorithm

repeat

Step 1 : Particles positioning on a sphere so as to maximise their separation

Step 2 : (Optimisation in orthogonal spaces) Newton scheme for constraints

Step 3 : (Optimisation in orthogonal spaces) Conjugate Gradient minimisation for the objective function

until The constraints are satisfied and the objective function minimal

In the next sections we will analyse each of the optimisation steps that we used.

6.6.1 Electrostatic model for particle forms

Since the sides of the voxels are all equal to one we need to maintain this property upon the sphere mapping. The initial mapping refrains from keeping the distances of the vertices with its direct neighbours constant. We realised that the nodes near the poles are much closer to each other than the ones near the equator. Using the constraints and the objective function in a orthogonal space minimisation fashion made slow progress in correcting that. It became obvious that an external force was necessary to accomplish that task.

The main idea behind the employment of the charged particles model comes directly from the bonding electron model. The particles are treated as mutually repulsive, where the forces acting are the electrostatic repulsions, subject to the constraint that the particles remain on the surface of a sphere. The dynamic system will oscillate until it reaches a steady state. The electrostatic forces are determined by Coulomb's Law: given two points $\mathbf{x}_1$ and $\mathbf{x}_2$ with identical charge, we can collect that charge information with other constants involved in Coulomb's Law into a constant k to generate the following equation:

$$\mathbf{F}_{12} = k\frac{\mathbf{x}_1 - \mathbf{x}_2}{\|\mathbf{x}_1 - \mathbf{x}_2\|^3}, \tag{6.22}$$

Clearly, when the particles system reaches equilibrium the particles have reached maximum separation positions. In practice the whole algorithm is quite straight forward and fast. For convenience we set the spring constant k to one for all the particles. Since there is a force connecting every node with all the others, the total force applied on that node $\mathbf{F}_i$ is equal to the sum of the forces from all vectors.

For every vertex S_i we calculate:

$$\mathbf{F}_i = \sum_{j \in V} \frac{\mathbf{s_i} - \mathbf{s_j}}{\|\mathbf{s_i} - \mathbf{s_j}\|^2} \tag{6.23}$$

The new positions for every vertex i in then updated by adding the force $\mathbf{F}_i$ applied on the vertex.

$$\mathbf{s'}_i = \mathbf{s}_i + \mathbf{F}_i. \tag{6.24}$$

6.6.2 Newton scheme for constraints

The Newton scheme will be used as part of an optimisation in orthogonal spaces approach to solve the constraint vector $\mathbf{C(s)} = \mathbf{0}$, which is constructed from all the m active constraints at the current state. The active constraints consists of the area equalities (6.19), and the active inequalities for the spherical angles (6.21). The Newton scheme is based in the assumption that the general non linear constraints can be linearised in a small area around the current state $\mathbf{x}$. Therefore, if we consider a small perturbation $\delta\mathbf{x}$ the first order Taylor series gives:

$$\mathbf{C}(\mathbf{x} + \delta\mathbf{x}) \approx \mathbf{C}(\mathbf{x}) + \mathrm{C}'(\mathbf{x})\, \delta\mathbf{x}, \tag{6.25}$$

where, C′ is the Jacobian matrix of C

$$\mathrm{C}'(\mathbf{x}) = \frac{\partial \mathbf{C}(\mathbf{x})}{\partial \mathbf{x}} = \begin{bmatrix} \frac{\partial C_1}{\partial x_1} & \cdots & \cdots & \frac{\partial C_1}{\partial x_n} \\ \vdots & \ddots & & \vdots \\ \frac{\partial C_m}{\partial x_1} & \cdots & \cdots & \frac{\partial C_m}{\partial x_n} \end{bmatrix} \tag{6.26}$$

The solution is reached as we show in the example of figure (5.6)when $\mathbf{C}(\mathbf{x}) = 0$, thus (6.25) becomes

$$\mathbf{C}(\mathbf{x} + \delta\mathbf{x}) = 0 \approx \mathbf{C}(\mathbf{x}) + \mathrm{C}'(\mathbf{x})\, \delta\mathbf{x}, \tag{6.27}$$

or

$$-\mathbf{C}(\mathbf{x}) = \mathrm{C}'(\mathbf{x})\, \delta\mathbf{x}, \tag{6.28}$$

In a least squares sense then (6.28) becomes,

$$\delta\mathbf{x} = -(\mathrm{C}'(\mathbf{x})^T\, \mathrm{C}'(\mathbf{x}))^{-1}\, \mathrm{C}'(\mathbf{x})^T\, \mathbf{C}(\mathbf{x}), \tag{6.29}$$

We solved this square symmetric problem using a conjugate gradient generic solver. The Jacobian C′ was initially calculated by using the analytic derivatives of the constraint functions, but a finite differences scheme proved easier to implement, although slower. The derivatives of the constraint function C_m is replaced by recalculating its value after a small perturbation ϵ and subtracting the original value. This difference is divided by the perturbation ϵ.

$$\frac{\partial C_m(\mathbf{x})}{\partial x_n} \approx \lim_{\epsilon \to 0} \frac{C_m(\mathbf{x}+\epsilon) - C_m(\mathbf{x})}{\epsilon} \tag{6.30}$$

Finally, due to the approximation through linearisation the Newton step might be too long and the feasible area missed. A backtracking line search algorithm is employed. When the final step $\delta\mathbf{x}$, is found the new state $\mathbf{x}' = \mathbf{x} + \delta\mathbf{x}$.

6.6.3 Minimisation for the objective function

The second step in each iteration of the constraint optimisation in orthogonal spaces involves the minimisation of the objective function (6.9) in the space tangent to the constraints hypersurface $\mathbf{C}(\mathbf{x}) = \mathbf{0}$, as it was described in section (5.7). We denote $G(\mathbf{x})$ the gradient of the objective function.

$$\nabla f(\mathbf{x}) = G(\mathbf{x}) = \begin{bmatrix} \frac{\partial f(\mathbf{x})}{\partial x_1} \\ \vdots \\ \\ \vdots \\ \frac{\partial f(\mathbf{x})}{\partial x_n} \end{bmatrix}. \tag{6.31}$$

This is the direction that will minimise the objective function. As described in the section (5.7), $G(\mathbf{x})$ can be analysed to one tangent to the constraints hypersurface part , $G_{\|}(\mathbf{x})$, and to one perpendicular $G_{\perp}(\mathbf{x})$, so that:

$$G = G_{\|} + G_{\perp} \tag{6.32}$$

The part perpendicular to the constraint surface, can be expressed as a linear combination of C′, the Jacobian used in the previous Newton step.

$$\mathrm{C}'\,\lambda = G_{\perp}(\mathbf{x}) \tag{6.33}$$

Since we are interested in the components of $G(\mathbf{x})$ in direction tangent to the constraint hypersurface $G_{\|}(\mathbf{x})$, we form a least squares problem

$$\lambda = (\mathrm{C}'^{T}\,\mathrm{C}')^{-1}\,\mathrm{C}'^{T}\,G(\mathbf{x}) \tag{6.34}$$

which we solve in respect to λ using a conjugate gradient generic solver. Then using,

$$G_{\|}(\mathbf{x}) = G(\mathbf{x}) - \mathrm{C}'\,\lambda \tag{6.35}$$

we can calculate the gradient projection in the tangent to the constraints space $G_{\|}(\mathbf{x})$.

We could use $G_{\|}$ as it is to perform the step towards the descending direction, using the steepest descent algorithm. However, using the current projected gradient direction in conjunction with all the previous gradients in a conjugate gradient scheme was practically faster. In each step a combination of the current and the previous projected gradients is used to calculate the conjugate gradient $\mathbf{P}$. The method used is the Polak and Ribière described in section (5.3).

Another addition to the above mentioned algorithm that proved beneficial for the minimisation of the objective function in respect to the constraints uses a Lagrangian function $\mathcal{L}$ to replace the objective f,

$$\mathcal{L}(\mathbf{x}, \lambda) = f(\mathbf{x}) - \lambda^{T}\,C(\mathbf{x}) \tag{6.36}$$

The minimisation step now minimises the Lagrangian in the space tangent to the constraints hypersurface. The gradient G of the objective function f is replaced by the gradient of the Lagrangian $\nabla\mathcal{L}(\mathbf{x}, \lambda)$ in respect to both $\mathbf{x}$ and λ. When we are on the $C(\mathbf{x}) = 0$ surface , $\nabla\mathcal{L}(\mathbf{x}, \lambda)_{\|} = G_{\|}$ in which case the tangent plane is the same. When not on $C(\mathbf{x}) = 0$, then $G_{\|}$ contains a contribution of the constraints. With the Lagrangian $\mathcal{L}(\mathbf{x}, \lambda)$ set up we are now taking better control over the constraints during the step to minimise the objective function.

A backtracking line search is employed to find the optimal state that minimises the Lagrangian function, along the path of the conjugate gradient $\mathbf{P}$. For a successful step $\delta\mathbf{s}$ we calculate the constraint vector $\mathbf{C}(\mathbf{x} + \delta\mathbf{s})$, making sure that none of the constraints is violated badly (which was set experimentally to $\|C(\mathbf{x} + \mathbf{1}) - C(\mathbf{x})\| < 0.1$) and at most only one of the inactive inequality constraints becomes active.

6.7 Convergence Conditions and results

The solution of the constrained optimisation problem, defined in the previous paragraphs is reached when the objective function is minimal and all the equality constraints are satisfied, all the inequalities inactive. The Euclidean norm of the constraint vector $\|\mathbf{C}(\mathbf{x})\|$, is used to define the cost of the constraints.

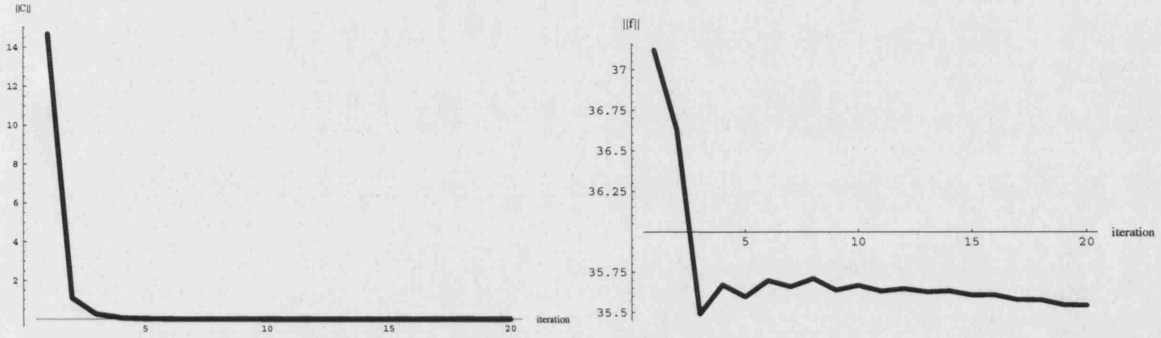

Figure 6.5: Graph for the process of the minimisation of the constraints (left) and the objective function(right), over 20 iterations of the described algorithm.

We know that the optimisation task has a feasible solution, since it is possible to construct a mapping that preserves area ratios. Then again, it is not possible in the general case to map every surface facet to a spherical square, it is not possible to avoid distortions, but we are satisfied if they are minimal. In the following graphs we can see the initial mapping and the optimised distribution of the nodes upon the sphere surface. The visual examination can verify the success of the optimisation procedure. Both the graphs show the same side of the sphere around the north pole. The spherical quadrilaterals seem to have the same size in contrast to the initial mapping where the ones around the poles were clearly larger. We notice that the pole in the final image has lost its significance and is treated like any other node. Finally, the shape of the quadrilaterals is now more stretched into the shape of spherical squares.

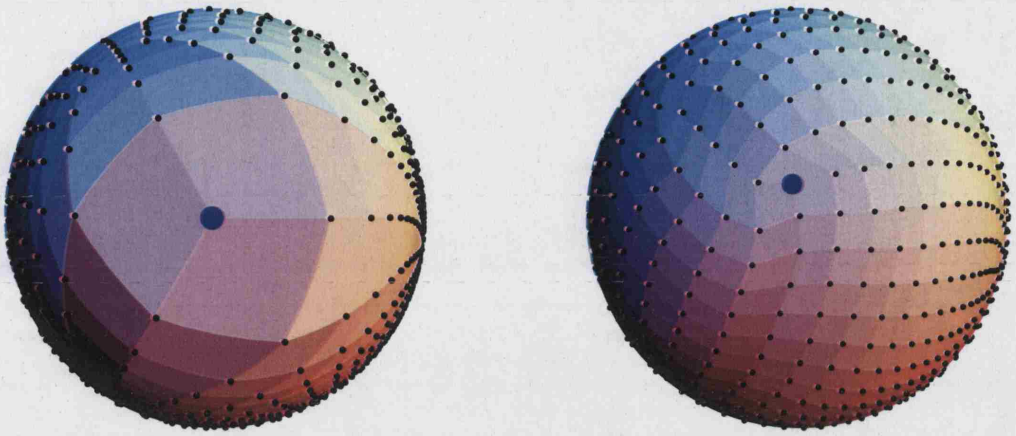

Figure 6.6: The distribution of the nodes on the sphere surface. The initial (left) and the one after the optimisation(right).

6.8 Conclusions

In this chapter we have presented a unified set of procedures for the mapping of a $3D$ object initially described as a set of voxels, to a sphere. An extraction of the surface from the voxel object, an initial mapping to the sphere and a constrained non linear optimisation procedure for the establishment of a well defined mapping was gradually built. The mapping offering a parametrisation of the closed surface of the object in two dimensions has many interesting applications. In combination to the spherical harmonics expansion that we are going to build in the next chapter can offer a compact and mathematically useful representation of volumetric objects. To the best of our knowledge, the cost and properties of the described algorithm is "well" comparable to those found in the literature [23, 39], and the results satisfactory for the proposed from this thesis applications in 3D shape reconstructions.

Chapter 7

Spherical Harmonics Representation

7.1 Introduction

In chapter 6, we defined a spherical parametrisation as the an invertible mapping from the unit sphere S^2 to a closed surface M, described as a net of surface vertices $\mathbf{v}$. The mapping is defined by assigning for each vertex $\mathbf{v}$ a parametrisation $\mathbf{s} = \upsilon^{-1}(\mathbf{v})$.

For the regular samples $\mathbf{s}$ on the sphere S^2, we have defined their image to a vertex $(\mathbf{v})$ on the surface M of the voxel object. Subsequently, in a process similar to the Fourier series decomposition we can use basis functions to represent the mapping υ on the sphere.

A natural choice of basis is spherical harmonics, functions defined on the sphere with nice mathematical properties. In the following sections we will explain the procedure for the representation of the mapping function υ using spherical harmonics along with some interesting applications.

7.2 Definition of spherical harmonics

The spherical harmonics degree l and order m are defined by:

$$Y_l^m(\vartheta, \varphi) = \sqrt{\frac{2l+1}{4\pi}\frac{(l-m)!}{(l+m)!}} P_l^m(\cos\vartheta) e^{im\varphi} \tag{7.1}$$

Where $m = \{-l, -(l-1), \ldots, (l-1), l\}$ and P_l^m are the *Legendre polynomials*. Using the identity,

$$Y_l^{-m}(\vartheta, \varphi) \equiv (-1)^m \bar{Y}_l^m(\vartheta, \varphi) \tag{7.2}$$

where, $\bar{z}$ denotes complex conjugate of z, we can deduce the real and imaginary part:

$$Re[Y_l^m] \equiv \frac{1}{2}\left(Y_l^m + (-1)^m Y_l^{-m}\right) \equiv \sqrt{\frac{2l+1}{4\pi}\frac{(l-m)!}{(l+m)!}} P_l^m(\cos\vartheta)\cos m\varphi \quad (7.3)$$

$$Im[Y_l^m] \equiv \frac{1}{2i}\left(Y_l^m - (-1)^m Y_l^{-m}\right) \equiv \sqrt{\frac{2l+1}{4\pi}\frac{(l-m)!}{(l+m)!}} P_l^m(\cos\vartheta)\sin m\varphi \quad (7.4)$$

Where the ϑ and φ dependance of the spherical harmonics has been dropped from the notation for clarity. One very interesting property of spherical harmonics is the orthogonality relation,

$$\int_0^{2\pi}\int_0^{\pi} Y_l^m(\vartheta,\varphi)\bar{Y}_{l'}^{m'}(\vartheta,\varphi)\sin(\vartheta)\, d\vartheta\, d\varphi \;= \quad (7.5)$$

$$= \int_0^{2\pi}\int_0^{1} Y_l^m(\cos(\vartheta),\varphi)\bar{Y}_{l'}^{m'}(\cos(\vartheta),\varphi)\, d\cos(\vartheta)\, d\varphi \;=\; \delta_{mm'}\delta_{ll'} \quad (7.6)$$

Since the spherical harmonics form a complete orthonormal basis, when normalised, a real function $f(\vartheta,\varphi) \in L^2(S^2)$, can be expanded in terms of spherical harmonics.

$$f(\vartheta,\varphi) = \sum_{l=0}^{\infty}\sum_{m=-l}^{l} C_l^m Y_l^m(\vartheta,\varphi), \quad (7.7)$$

Where the coefficients, which are in general complex numbers $\{C_l^m\}$, can be determined by a process analogous to the Fourier Series Theory.

$$C_l^m = \langle f(\vartheta,\varphi), Y_l^m(\vartheta,\varphi)\rangle = \int_0^{\pi}\int_0^{2\pi} f(\vartheta,\varphi)Y_l^m(\vartheta,\varphi)\, d\varphi\sin\vartheta\, d\vartheta. \quad (7.8)$$

Where $\langle \_, \_ \rangle$ symbolises the inner product. The coefficients $\{C_l^m\}$, are the spherical harmonics descriptors of the function $f(\vartheta,\varphi)$. Having calculated them we can reproduce the function according to (7.7). In practice we truncate the infinite series of coefficients and use them up to some degree l to approximate $f(\vartheta,\varphi)$.

One last comment is that in order to ease the calculations and make the descriptors more compact, we define a real basis as:

$$\tilde{Y}_l^m(\vartheta,\varphi) := \begin{cases} Re[Y_l^m](\vartheta,\varphi), & \text{when } m \le 0; \\ Im[Y_l^m](\vartheta,\varphi), & \text{when } m > 0. \end{cases} \quad (7.9)$$

for which the orthogonal condition $\langle\, \tilde{Y}_l^m,\ \bar{\tilde{Y}}_{l'}^{m'}\,\rangle = \delta_{mm'}\delta_{ll'}$, can be easily proved.

7.3 Representation

Returning to the spherical parametrisation of the voxel object. The parametric function $\upsilon(\vartheta, \varphi)$, moves throughout the surface of the object, while the parameters ϑ and φ range in $[0, \pi]$ and $[0, 2\pi]$ correspondingly.

$$\upsilon(\vartheta, \varphi) = \begin{pmatrix} x(\vartheta, \varphi) \\ y(\vartheta, \varphi) \\ z(\vartheta, \varphi) \end{pmatrix} \tag{7.10}$$

where $(\{x, y, z\}$ are the Cartesian coordinates of the surface points. The parametrisation procedure has estimated the (ϑ, φ) parameters only for the vertices $\mathbf{v}$ on the voxel object's surface net. Therefore, some kind of interpolation should be used in order to recover the whole surface. We choose to use a weighted average of real spherical harmonics as described in equation (7.7). Consequently, we need to calculate the coefficients $\{C_l^m\}$ in the following expression which forms a discrete version of (7.8).

$$\{C_l^m\} = \begin{pmatrix} C_{l,x}^m \\ C_{l,y}^m \\ C_{l,z}^m \end{pmatrix} \simeq \frac{4\pi}{n} \sum_{i=1}^{n} \begin{pmatrix} x_i \\ y_i \\ z_i \end{pmatrix} Y_l^m(\vartheta_i, \varphi_i) \tag{7.11}$$

Where $\mathbf{v}_i = \{x_i, y_i, z_i\}$ are the coordinates of the vertices on the voxel object with $\mathbf{s}_i = (\vartheta_i, \varphi_i)$ their image on the sphere with $i = 1 \ldots, n$. Experiments show that this method fails to produce an accurate description of the shape. Instead, we are going to use a least squares fitting of the spherical harmonics series created by the coefficients on the original positions of the vertices.

Initially, an indexing scheme $\beta^{(l,m)}$ was created, storing all the possible combinations of different degrees l and orders m up to some desired degree ϖ for the representation .

$$\beta^{(l,m)} = \{(0,\ 0),\ (1,-1),\ (1,\ 0),\ (1,\ 1),\ (2,-2),\ (2,-1),\ (2,\ 0),\ (2,\ 1),\ (2,\ 2),\ \ldots\} \tag{7.12}$$

We arrange the values of the basis functions in a matrix B with dimensions $(n \times w)$, where n

is the total number of vertices and

$$w = 1 + \sum_{k=1}^{\varpi} 2k + 1$$

the desired number of basis functions that will be used. Its elements will look like

$$b_{i,j} = Y_l^m(\vartheta_i, \varphi_i)$$

where l and m are taken from the j^{th} entry in $ß^{(l,m)}$.

Finally, a matrix X, of size $(n \times 3)$, is created to store the Cartesian coordinates of the vertices $\mathbf{v}_i$, so that $\mathrm{X_i} = \{x_i, y_i, z_i\}$, and the unknown coefficients $\{C_l^m\}$ arranged into the $(n \times 3)$ matrix C. The equation (7.11) becomes:

$$\mathrm{C} \simeq \frac{4\pi}{n} \mathrm{B}^T \mathrm{X}. \tag{7.13}$$

Since we want to make sure that the spherical harmonics series approximates the vertices net, we want to minimise the error E in:

$$\mathrm{X} = \mathrm{BC} + E \tag{7.14}$$

From least squares, using the pseudo inverse of B:

$$\mathrm{C} = (\mathrm{B}^T\mathrm{B})^{-1}\mathrm{B}^T\mathrm{X} \tag{7.15}$$

Which is solved with a standard conjugate gradient algorithm in order to calculate the $\{C_l^m\}$ coefficients.

7.4 The parametric representation

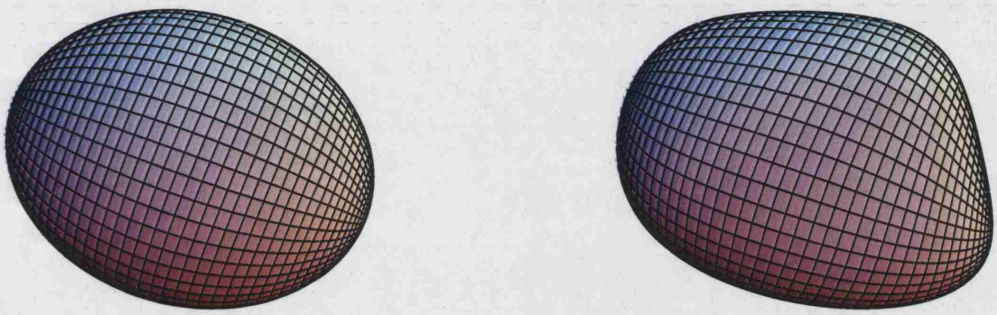

Figure 7.1: Representation of the object in figure (6.1) with the spherical harmonics truncated over the first degree (3×4 coefficients) (left) and fourth degree (3×25 coefficients)(right).

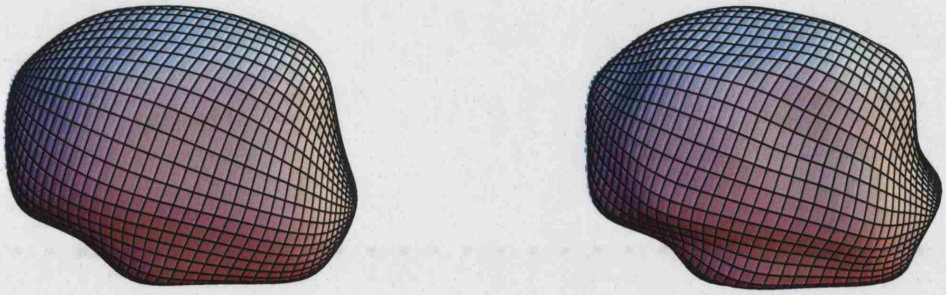

Figure 7.2: Representation of the object in figure (6.1) with the spherical harmonics truncated over the seventh (3×64 coefficients)(left) and the eleventh degree (3×144 coefficients) (right).

Having defined the complex coefficients $\{C_l^m\}$, we can use them to create the parametric description of the surface, by weighted averaging with the relevant spherical harmonics.

$$v = \begin{cases} v_x(\vartheta,\varphi) &= \sum_{l=0}^{\varpi}\sum_{m=-l}^{l} C_{l,x}^{m} Y_l^m(\vartheta,\varphi), \\ v_y(\vartheta,\varphi) &= \sum_{l=0}^{\varpi}\sum_{m=-l}^{l} C_{l,y}^{m} Y_l^m(\vartheta,\varphi), \\ v_z(\vartheta,\varphi) &= \sum_{l=0}^{\varpi}\sum_{m=-l}^{l} C_{l,y}^{m} Y_l^m(\vartheta,\varphi), \end{cases} \tag{7.16}$$

where ϖ is the maximum degree of spherical harmonics that we used for the particular representation. By truncating the spherical harmonics series in different degrees we can create a level of detail series of representation as shown in figures (7.1) and (7.2).

7.5 Creation of surface mesh

In the previous section the parametric mapping of the voxel object was represented. This technique offers two contributions. A parametric function $v(\vartheta,\varphi)$ from a unit sphere to the objects surface and a compact description of the surface in a small number of spherical harmonics coefficients. There are numerus applications of the presented method. However, since we would like to link the parametric shapes with the solution of Boundary Elements Method, there is a meshing requirement on the surface of the objects. We experimented with two approaches that both use the parametric description as defined in (7.16), to automatically create a surface mesh.

7.5.1 Drawing equatorial grid

In (7.16), ϑ is assigned values from 0 to π, while φ ranges from 0 to 2π. For $\vartheta = 0$ and $\vartheta = \pi$ we get the two poles, North and South. A first step towards the triangulation of the surface is the division into stripes by drawing the equatorial grid for ϑ = constant and φ = constant in regular intervals. This produces rectangular surface patches. Following our requirements for a triangular mesh we can divide the rectangular patches into two triangles each, by using one of the diagonals as seen in figure (7.3).

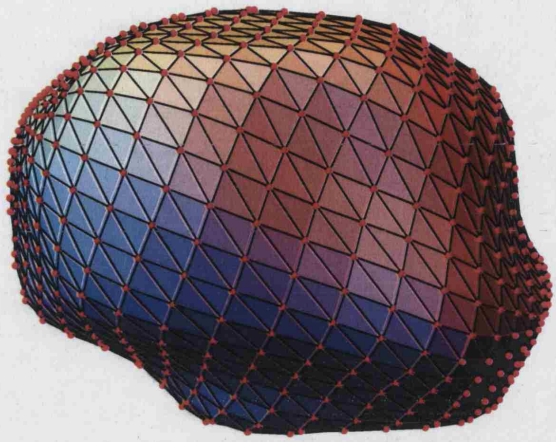

Figure 7.3: Triangle surface mesh created by equatorial grid

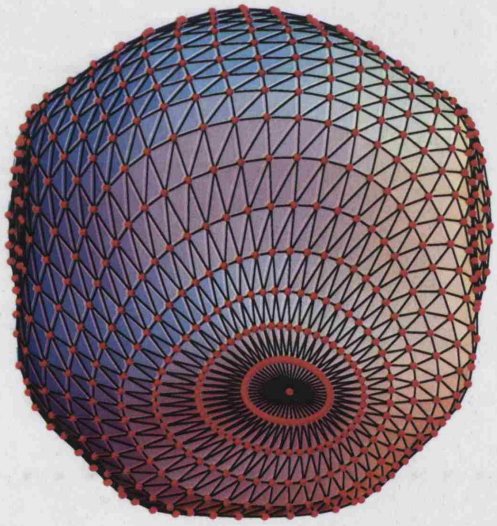

Figure 7.4: Equatorial grid, mesh around the poles

Some special care is needed around the poles during the triangulation in order to avoid singularities and too long triangles. Using the first set of samples placed on the iso-contour surrounding the pole we construct triangles with one corner on the pole and two on successive nodes on the first iso-contour, as seen in figure (7.4).

The created mesh is fully adaptable in the sense that changing the resolution becomes as trivial as deciding how many iso-contours we will draw. A mesh of any size with any number of elements can be constructed in a very straight forward way. A major drawback of the method can be seen in figure (7.4), where around the poles we can trace some slim and lengthy elements with small angles which are generally to be avoided in numerical solutions like BEM, since they affect badly the accuracy of the numerical solution by introducing errors and delays [85].

7.5.2 Mapping a spherical mesh

A second method that produced much more acceptable results arises from the fact that we have constructed a mapping function υ from a sphere surface to the surface of the object. Consequently, any mesh V' defined on the sphere surface could be easily mapped to any parametrically defined object. Here, a regular triangular mesh , having e.g.980 elements, on the sphere's surface was created by tessellation of an embedded icosahedron. (see fig. (7.5).

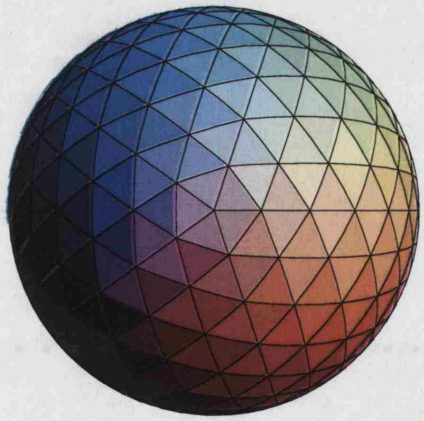

Figure 7.5: Mesh defined on the sphere by tessellation of a icosahedron

The areas defined by each triangle on the sphere surface have equal size and similar shape. Since the spreading of the parameters along the object surface is homogeneous, a regular mesh defined V' on the sphere can be mapped on the final object as in fig. (7.5.2). Every node

in the spherical mesh has a pair of spherical coordinates (ϑ, φ). We can use the parametric function (7.16) in order to find the coordinates of the nodes mapped on the new object. Thus, the irregular meshing and the ugly elements around the poles of the iso-contours method, will not be an issue any more. (see fig. (7.7).

Figure 7.6: A regular spherical mesh mapped on the voxel object

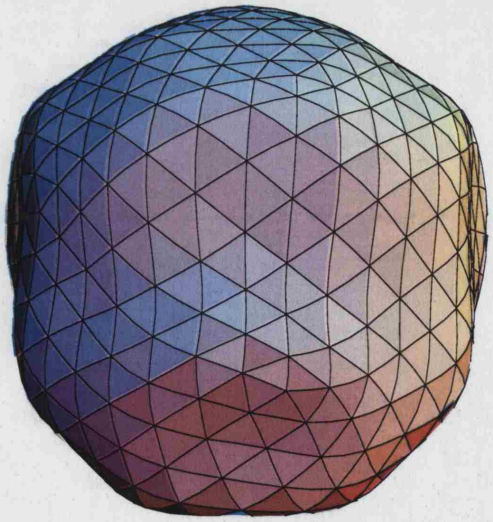

Figure 7.7: A regular spherical mesh mapped on the voxel object, frontal view. Notice that the effect of the poles disappears.

7.6 Multi-layer models

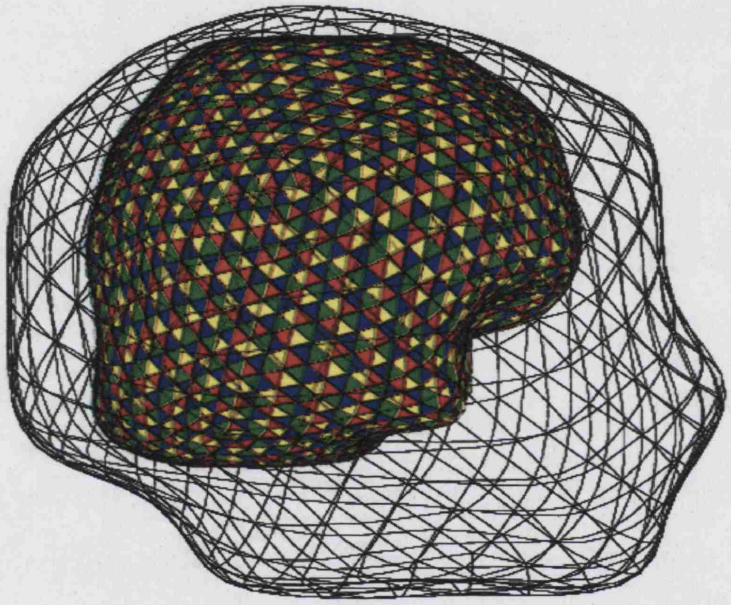

Figure 7.8: A two-layer model. In the mesh for the brain surface a different colour scheme was used for each of the triangles.

Using the meshing methods described in the previous sections we are ready now to construct a multi-layer model of a head anatomy from MRI or CT-scan data. Using a segmented image of the brain surface in voxels as shown in fig. (7.9), from the same MRI that was used for the scalp surface of fig. (6.1), we created a parametric model for the brain surface and a mesh as shown in fig. (7.10)

Following up the two meshes, fig. (7.10) for the brain and fig. (7.5.2) for the scalp were placed together to give the model fig. (7.8).

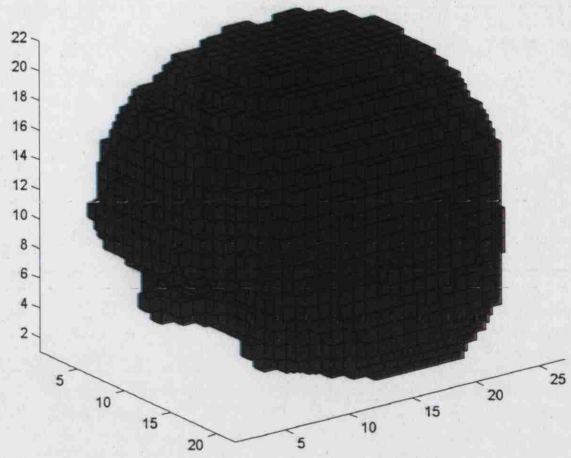

Figure 7.9: Voxel representation of a baby's brain surface from segmented MRI data. Thanks to Richard Bayford, Middlesex University.

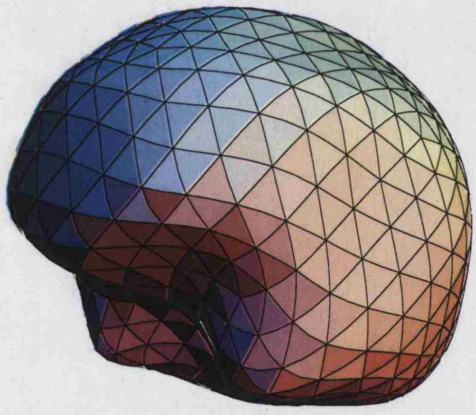

Figure 7.10: Regular spherical mesh mapped onto a brain's surface

7.7 Conclusions

We notice that the definition of the regular mesh on the sphere's surface provides equal areas triangles, and since we have created a one-to-one mapping this quality will be inherited on the objects surface mesh. In addition, the creation of the mesh on the sphere initially, leaves us with

unlimited potential to create a mesh with any number of elements, and a hierarchy of meshes can be created for a particular object, defining a level-of-details description.

Finally, the decomposition of the object shape in spherical harmonics coefficients allows for a shape descriptor using few $\{C_l^m\}$ parameters. A feature that will be explored in a shape based inverse problem in chapter 8.

Chapter 8

Shape Reconstruction Technique

8.1 Introduction

Up to this point we have described almost all of the tools that are necessary for the development of a shape based reconstruction using the spherical harmonics parametric surfaces. In this chapter we will try to combine those techniques to define the shape based approach to the inverse and forward problem in OT.

Let's consider once more the bounded domain $\Omega \subset \mathbb{R}^3$ which we assume that is divided into L disjoint regions Ω_ℓ

$$\Omega = \bigcup_{\ell=1}^{L} \Omega_\ell, \tag{8.1}$$

which are bounded by smooth surfaces Γ_ℓ, and have piecewise constant optical properties $\{D, \mu_a\}_\ell$.

The proposed technique based on the assumption that $\Omega_1 = \partial\Omega$ and the optical coefficients $\{D, \mu_a\}_\ell$, $\ell = 1, \ldots, L$ are *a-priori* known, works towards the recovery of the unknown boundaries Γ_ℓ, starting from some initial guess and a least squares fitting. Having recovered the boundaries the complete 3D image of the light absorption and scattering inside the domain Ω can be fully reconstructed.

To describe the boundaries Γ_ℓ in few parameters we will use the parameterisation method and the description in few spherical harmonics coefficients $\{C_l^m\}_\ell$. Then the recovery of the boundaries Γ_ℓ becomes the estimation of the spherical harmonics coefficients that describe

them. In the rest of this chapter for simplicity we introduce the notation

$$\gamma_\ell = \{C_l^m\}_\ell, \quad with \quad l = 1, \ldots, \varpi \quad and \quad m = -l, \ldots, l. \tag{8.2}$$

for the finite set of spherical harmonics coefficients that describe the surface Γ_ℓ reconstructed with up to degree ϖ spherical harmonics.

The objective of the novel 3D shape estimation method described in this chapter is the reconstruction of the boundaries Γ_ℓ based on OT measurements on $\partial\Omega$. The shapes and locations of the boundaries are described by finite sets of shape coefficients $\{\gamma_\ell\}$ and then the forward problem, which is based on a BEM discretisation of the diffusion equation, is formulating the mapping from the shape coefficients $\{\gamma_\ell\}$ and the optical parameters values $\{D, \mu_a\}_\ell$ to the data $\mathbf{g}$ on the surface $\partial\Omega$. The inverse problem is then to find the representation $\{\gamma_\ell\}$ when observed or simulated measurement $\mathbf{g}$ and the values $\{D, \mu_a\}_\ell$ are given.

One attractive feature of this technique is the dimension of the search space for the inverse problem which is significantly reduced than with the commonly used local pixel basis techniques. The reduction of the dimension for the search space is potentially leading to less ill posed inverse problems. In addition the use of the BEM discretisation upon surface meshes constructed by mapping on the sphere, reduces the effort taken for the construction of volume meshes necessary in the pixel basis techniques.

The rest of the chapter deals with the formulation and the details of the forward and inverse problems for the shape based approach.

8.2 The Forward Problem

Following the typical experimental configuration, we place S sources p_s , $s = 1, \ldots, S$ and M detectors m_d, $d = 1, \ldots, M$, widely spread on the top and back of the surface $\partial\Omega$, as illustrated in the graph (8.1).

During the experiment, light is shone from one source p_s and collected from all the detectors m_d, $d = 1, \ldots, M$. Next, a different source is chosen and measurements are collected each time, until all individual sources are used. We note $g_{s,d}$ the measurements collected on detector d when light was shone from source s alone , and $\mathbf{g}_s$ the vector of the measurements from all detectors, done with source s.

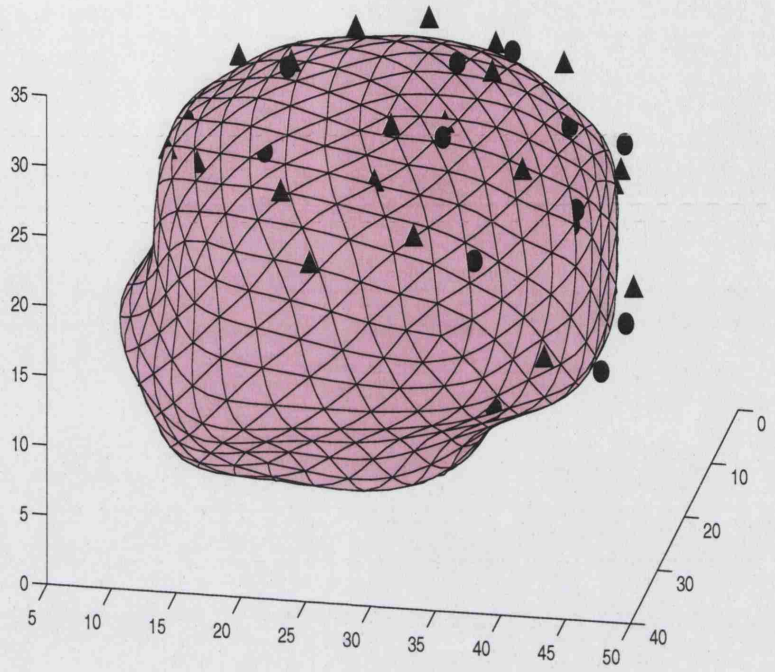

Figure 8.1: The experimental setup commonly used in OT, shown from the back, by circles we denote the sources p_s and by triangles the detectors m_d

Using the mapping of regular sphere meshes to the parametric surfaces defined by the coefficients $\{\gamma_\ell\}$ we achieve a discretisation of the boundaries Γ_ℓ which divide the domain Ω into regions with different optical coefficients, $\{D, \mu_a\}_\ell$ into P_ℓ surface elements $\tau_{\ell,k}$; $k = 1, \ldots, P_\ell$ with N_ℓ vertices $\mathbf{N}_{\ell,k'}$; $k' = 1, \ldots, N_\ell$.

Using those meshes the light intensity Φ on $\partial\Omega$ can be approximated from a piecewise function

$$\Phi(\mathbf{r}) \approx \sum_{k'=1}^{N_1} \Phi^{k'} u_{k'}(\mathbf{r})$$

with the basis functions $u_{k'}(\mathbf{r})$ chosen to have local support. The diffusion equation or rather the equivalent Helmholtz (3.30) from chapter 3 can then be solved numerically using BEM as described in chapter 4 to evaluate the vector $\mathbf{\Phi} = \{\Phi^1, \ldots, \Phi^{k'}, \ldots, \Phi^{N_1}\}$. Using the formulation described in chapter 4 and one source position p_s we construct the BEM linear system (4.35).

$$\mathrm{T}(\,\{\gamma_\ell\}\,,\ \{D\,,\ \mu_a\}_\ell\,)\,\mathbf{\Phi}_{p_s} = \mathbf{q}(p_s) \tag{8.3}$$

To relate the BEM approach to the forward model, we define the discrete-to-discrete operator $\mathcal{M} : \mathbb{R}^{N_1} \to \mathbb{R}^M$ from [11].

$$\mathcal{M}\Phi_{p_s} = \mathbf{g}_s, \tag{8.4}$$

to get the measurements on the discrete points m_d, $d = 1, \ldots, M$.

We can define then the nonlinear forward operator $\mathcal{K}(\gamma, D, \mu_a)$ as the mapping from the optical properties and the geometric parameters to the measurements on the surface of Ω.

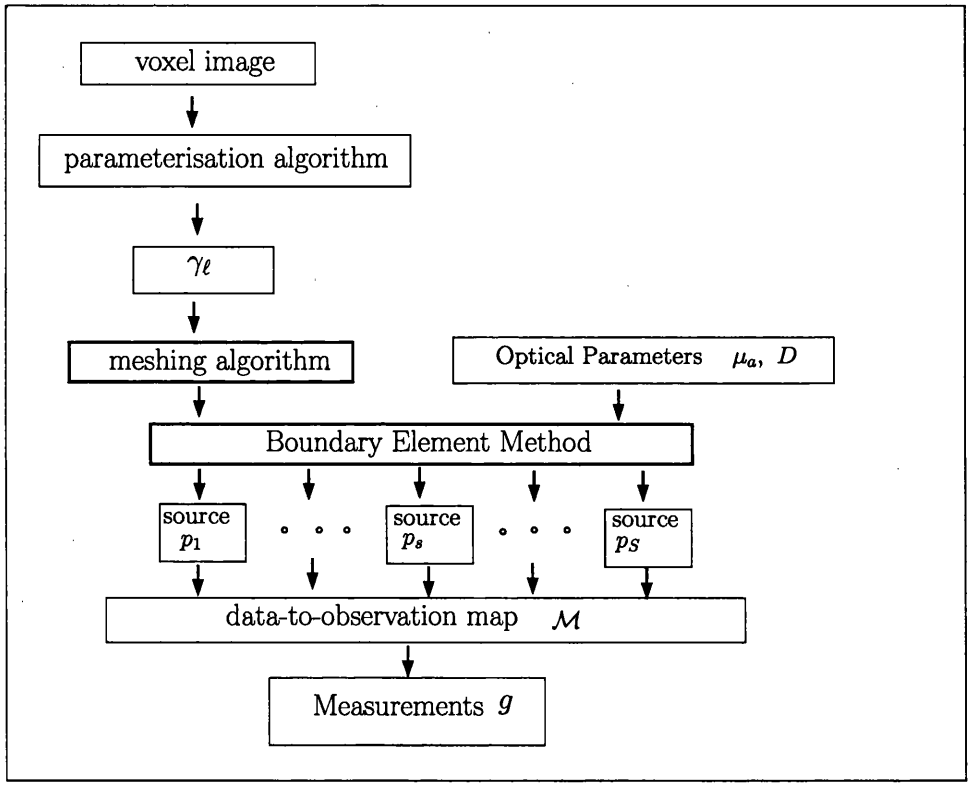

Figure 8.2: Schematic operation of the forward model

In the OT measurement set up, there are independent sets of measurements from all detectors for each of the sources and the forward mapping will actually have the form:

$$\begin{Bmatrix} \mathcal{K}_1(\gamma, D, \mu_a) \\ \mathcal{K}_2(\gamma, D, \mu_a) \\ \vdots \\ \mathcal{K}_S(\gamma, D, \mu_a) \end{Bmatrix} = \begin{Bmatrix} \mathbf{g}_1 \\ \mathbf{g}_s \\ \vdots \\ \mathbf{g}_S \end{Bmatrix} \quad \text{for all sources} \quad s = 1, \ldots, S \tag{8.5}$$

The forward calculation is used S times, one for each alternative source, and the results are arranged in the measurements vector g as shown in (8.5).

8.3 The shape inverse problem

Starting from a geometric configuration defined by the set of shape coefficients (γ^0), we will try to search for the set (γ^*) that minimises the distance between computed $\mathcal{K}(\gamma^h, D, \mu_a)$ and (measured/simulated) known data g. Therefore, defining the least squares-functional for that distance:

$$\Xi(\gamma) \ : \ = \ \|\mathbf{g} - \mathcal{K}(\gamma, D, \mu_a)\|^2 \tag{8.6}$$

The inverse problem is a cost minimisation procedure:

$$\text{find } (\gamma^*) \text{ so that } \ \Xi(\gamma^*) \ = \ \arg\min_{\gamma} \|\mathbf{g} - \mathcal{K}(\gamma^h, D, \mu_a)\|^2 \tag{8.7}$$

A typical way to minimise such a cost function would be a Newton-type method, which we discussed in chapter 5, where we seek for a minimum for $\Xi(\gamma)$ by iterations of local linearisation and Taylor expansion around the current estimate as :

$$\gamma^{h+1} = \gamma^h \ + \ (J_h^T J_h)^{-1} \ J_h^T(\mathbf{g} - \mathcal{K}(\gamma^k, D, \mu_a)) \tag{8.8}$$

Where the Jacobian matrix J, is a derivative of the forward operator $\mathcal{K}$ with respect to the shape coefficient γ .

$$J = \frac{\partial \mathcal{K}(\gamma, D, \mu_a)}{\partial \gamma} \tag{8.9}$$

However, after experimentation the Newton method was found unstable and slow due to the ill-conditioned Jacobian matrices J_k and some additional speed was gained by the use of the following iteration.

$$\gamma^{k+1} = \gamma^k + (J_k^T J_k + \lambda \, \mathrm{I})^{-1} J_k^T (g - \mathcal{K}(\gamma^k, D, \mu_a)) \tag{8.10}$$

We should notice that this iteration formula is similar to that of the Levenberg-Marquandt, described in chapter 5 with the addition of the control parameter, λ, being a vector $\lambda = \{\lambda_1, \ldots, \lambda_i, \ldots, \lambda_n\}$, with $0 < \lambda_1 < \ldots < \lambda_i < \ldots < \lambda_n$ that acts on the diagonal of $(J_k^T J_k)$

as a scaling factor to compensate for the difference in the magnitude of the shape parameters.

This method has been proven practically to favour the evolution of the minimisation in the directions defined from the coefficients of lower degree. In this way we favour the low frequencies in the spherical harmonics description that define the location and the coarser characteristics of the parametric surface. As a result the convergence of the minimisation becomes faster with the location and the general shape of the parametric surface recovered in the first few initial iterations of the algorithm. While the minimisation proceeds the values of λ_i are changed *ad hoc* to flatten out that effect and allow for the minimisation to follow the highest frequencies directions. That is done by setting $\lambda_i = 0$ for $i = 1, \ldots, n$, and thus following the Gauss Newton iteration (8.8). (See also figure (8.9).)

The modified Newton method (8.10), for the minimisation of the residual (8.6) produces the descent direction in the parameters space, by providing a step $\delta\gamma^k = \gamma^{k+1} - \gamma^k$. In practice moving $\Xi(\gamma)$ to the full step length $\delta\gamma^k$ could lead the residual far from the actual minimum. A quadratic fit line search method (5.5.2) is introduced in order to avoid detours in the down hill direction and speed up the optimisation.

8.4 Differentiation of the Forward Operator

One of the key elements in the implementation of the optimisation (8.10) is the calculation of the Jacobian J.

$$J = \frac{\partial \mathcal{K}(\gamma, D, \mu_a)}{\partial \gamma} \tag{8.11}$$

The usual way to calculate these derivatives is by finite differences based on the definition of the derivative. Let's assume we need the derivative in respect to a particular geometric coefficient γ_i , $i = 1, \ldots, n$ from the vector of the coefficients (γ^h) that describe the current state. Then

$$J_h = \frac{\partial \mathcal{K}(\gamma, D, \mu_a)}{\partial \gamma_i} = \lim_{\varepsilon_i \to 0} \frac{\mathcal{K}(\gamma_1, \ldots, \gamma_i + \varepsilon_i, \ldots, \gamma_n, D, \mu_a) - \mathcal{K}(\gamma_1, \ldots, \gamma_i, \ldots, \gamma_n, D, \mu_a)}{\varepsilon_i} \tag{8.12}$$

where ε_i is a relatively small perturbation for the spherical harmonic coefficient γ_i. The practical choice of ε_i requires a compromise between the mathematical accuracy of the derivative approximation and the computer roundoff error consideration [128]. In our case it was approximated experimentally to $10^{-4} * \gamma_i$. The calculation of the discrete derivative in this sense is a

simple procedure. It does not require any alteration into the tools that we already constructed, since the BEM solver is used in a black box configuration and could be implemented straight forwardly.

Unfortunately the finite differences method for the calculation of the derivative of the forward operator $\mathcal{K}$ in respect to the geometric parameters γ involves many forward solutions. We need to calculate the forward problem separately for each of the sources p_s , $s = 1, \ldots, S$ with a small perturbation ε_i in one at the time of the n geometric coefficients. Therefore we need $n \times S$ calculations of the forward problem. This translates to n constructions of a new matrix T and the same number of solutions the BEM linear system . The calculation of the Jacobian in this way due to the the cost of the BEM calculations for each of the perturbed parameters is alarming.

8.5 The Adjoint Method

We found that an adjoint method can drastically reduce the cost of the Jacobian evaluations and the numerical errors. Assume that the matrix T is invertible and differentiable with derivative $\frac{\partial \mathrm{T}(\gamma)}{\partial \gamma_i}$. Differentiation of the identity,

$$\mathrm{T}(\gamma)^{-1} \cdot \mathrm{T}(\gamma) = \mathrm{I} \tag{8.13}$$

yields,

$$\frac{\partial \mathrm{T}(\gamma)^{-1}}{\partial \gamma_i} \mathrm{T}(\gamma) + \mathrm{T}(\gamma)^{-1} \frac{\partial \mathrm{T}(\gamma)}{\partial \gamma_i} = 0 \tag{8.14}$$

so

$$\frac{\partial \mathrm{T}(\gamma)^{-1}}{\partial \gamma_i} \mathrm{T}(\gamma) = -\mathrm{T}(\gamma)^{-1} \frac{\partial \mathrm{T}(\gamma)}{\partial \gamma_i} \tag{8.15}$$

giving

$$\frac{\partial \mathrm{T}(\gamma)^{-1}}{\partial \gamma_i} = -\mathrm{T}(\gamma)^{-1} \frac{\partial \mathrm{T}(\gamma)}{\partial \gamma_i} \mathrm{T}(\gamma)^{-1} \tag{8.16}$$

The relation (8.16) can be used in a technique that reduces the number of forward calculations needed for the construction of the Jacobian J by associating the derivative of the forward operator $\mathcal{K}(\gamma)$ in respect to the shape coefficients γ_i to the derivative of the actual BEM matrix T (4.35).

Starting from the BEM linear system constructed for a source position s:

$$\mathrm{T}(\gamma)\,\mathbf{\Phi}_s = \mathbf{q}_s(\gamma) \Rightarrow \mathbf{\Phi}_s = \mathrm{T}(\gamma)^{-1}\,\mathbf{q}_s(\gamma) \tag{8.17}$$

Where $\mathrm{T}(\gamma)$ is the BEM system matrix constructed for the geometrical setup defined by the parameters (γ), $\mathbf{q}_s(\gamma)$ the right hand side vector and $\mathbf{\Phi}_s$ the solution vector for the s^{th} source.

In the same way as we defined the measurements operator $\mathcal{M}$ in (8.4) to get the measurement on the detectors m_d from the solution Φ_s, we can form a standard d^{th} unit vector $\mathbf{e}_d = [\,0\;0\;\cdots\;0\;1\;0\;\cdots\;0\;0\,]$, where the value 1 is at d^{th} position that represents a detector, and get the measurement g_{sd} from the solution,

$$g_{sd} = \mathbf{e}_d^T \cdot \Phi_s = \mathbf{e}_d^T \cdot \mathrm{T}(\gamma)^{-1} \cdot \mathbf{q_s}(\gamma) \tag{8.18}$$

By differentiation in respect to γ_i we get:

$$\frac{\partial g_{sd}}{\partial \gamma_i} = \mathbf{e}_d^T \cdot \frac{\partial\, \mathrm{T}^{-1}(\gamma)}{\partial \gamma_i} \cdot \mathbf{q_s}(\gamma) + \mathbf{e}_d^T \cdot \mathrm{T}^{-1}(\gamma) \cdot \frac{\partial \mathbf{q_s}(\gamma)}{\partial \gamma_i} \tag{8.19}$$

Using the identity (8.16):

$$\frac{\partial g_{sd}}{\partial \gamma_i} = \mathbf{e}_d^T \cdot \mathrm{T}^{-1}(\gamma) \cdot \frac{\partial\, \mathrm{T}(\gamma)}{\partial \gamma_i} \cdot \mathrm{T}^{-1}(\gamma) \cdot \mathbf{q_s}(\gamma) + \mathbf{e}_d^T \cdot \mathrm{T}^{-1}(\gamma) \cdot \frac{\partial \mathbf{q_s}(\gamma)}{\partial \gamma_i} \tag{8.20}$$

If we denote:

$$\mathbf{\Psi}_d = \mathbf{e}_d^T \cdot \mathrm{T}^{-1}(\gamma) \tag{8.21}$$

Then

$$\begin{aligned} \mathbf{\Psi}_d^T &= (\mathrm{T}^T(\gamma))^{-1} \cdot \mathbf{e}_d \\ \mathrm{T}^T(\gamma) \cdot \mathbf{\Psi}_d^T &= \mathbf{e}_d \end{aligned} \tag{8.22}$$

Which we can solve using a linear solver like GMRES to calculate $\mathbf{\Psi}_d$ for each detector d.

Likewise, denoting:

$$\mathbf{\Phi}_s = \mathrm{T}^{-1}(\gamma) \cdot \mathbf{q}_s(\gamma) \tag{8.23}$$

forms the linear system

$$\mathrm{T}(\gamma) \cdot \mathbf{\Phi}_s = \mathbf{q}_s(\gamma) \tag{8.24}$$

which we can again solve with a linear solver for each source s.

As for the second term in (8.20), denoting:

$$\mathbf{Q}_s = \mathrm{T}^{-1}(\gamma) \cdot \frac{\partial\, \mathbf{q}_s(\gamma)}{\partial \gamma_i} \tag{8.25}$$

we form the linear system

$$\mathrm{T}(\gamma) \cdot \mathbf{Q}_s = \frac{\partial\, \mathbf{q}_s(\gamma)}{\partial \gamma_i} \tag{8.26}$$

Then the equation (8.20) becomes:

$$\frac{\partial g_{sd}}{\partial \gamma_i} = \mathbf{\Psi}_d \cdot \frac{\partial\, \mathrm{T}(\gamma)}{\partial \gamma_i} \cdot \mathbf{\Phi}_s + \mathbf{e_d} \cdot \mathbf{Q_s} \tag{8.27}$$

Where we notice that $\frac{\partial g_{sd}}{\partial \gamma_i}$ are the actual entries of the Jacobian J_h. In contrast to the black box approach to the forward operator this adjoint method reduces the number of the necessary BEM matrix creations to n. The creation of the system matrix is so far proven to be the most costly procedure in our experiments so this adjoint method proved to increase the speed significantly.

8.6 Derivative of the BEM System Matrix

Even though the adjoint configuration decreased the cost of the calculation of the derivative and removed the dangers involved in a black box method, there still is the need to calculate the derivative of the BEM system matrix T in respect to the geometrical parameter γ_i. In our case this is done again by a finite difference method following the definition of the derivative.

$$\frac{\partial\, \mathrm{T}(\gamma)}{\partial \gamma_i} = \lim_{\varepsilon_i \to 0} \frac{\mathrm{T}(\gamma_1, \ldots, \gamma_i + \varepsilon_i, \ldots, \gamma_n) - \mathrm{T}(\gamma_1, \ldots, \gamma_i, \ldots, \gamma_n)}{\varepsilon_i} \tag{8.28}$$

At this point it is worthy to investigate what is the effect that the small perturbation ε_i on the geometric parameter γ_i has on the BEM solution. By the perturbation of the coefficient

γ_i, which acts on the relevant spherical harmonic Y_k in the parametric expression (7.16), the surface configuration changes from Ω_ℓ to Ω'_ℓ.

Lets assume without loss of generalisation, that we have a two layer set-up where Γ_1 is the boundary of the domain and Γ_2 the hidden obstacle. Then according to (4.35) the system matrix T will have the form:

$$\begin{pmatrix} \frac{1}{2}\mathrm{I} + \mathrm{A}_{11} + \frac{1}{2\alpha D}\mathrm{B}_{11} & -\mathrm{A}_{12} & \mathrm{B}_{12} \\ 0 & \frac{1}{2}\mathrm{I} + \mathrm{A}_{22} & -\mathrm{B}_{22} \end{pmatrix}$$

where we notice that since only the surface Γ_2 is changing with the perturbation in any coefficient γ_i, for the calculation of $\mathrm{K}(\gamma_1, \ldots, \gamma_i + \varepsilon_i, \ldots, \gamma_n)$ the $\mathrm{A}_{11}, \mathrm{B}_{11}$ blocks of the system matrix can be reused.

There are better ways to implement the derivative of the BEM solution. One can look in the relevant literature for direct derivation of the boundary equation in respect to the design parameters e.g. in [80]. But in the framework of this thesis the development and implementation of a direct differentiation has to be set as future work.

8.7 Scaling for the data

In practice the measurements in the FD experiment for OT are complex numbers, that is $\mathbf{g} \in \mathbb{C}^M$ and that is also true for the simulated measurements from the solution of the forward problem $\mathcal{K}(\gamma, D, \mu_a) \in \mathbb{C}^M$, where we remind that M is the total number of detectors m_d.

We use the following representation for g:

$$g = Re(g) + i\, Im(g) = \|g\|\, e^{i \arg(g)} \tag{8.29}$$

where

$$\|g\| = (Re(g)^2 + Im(g)^2)^{\frac{1}{2}} \tag{8.30}$$

is the *amplitude* of the data, and

$$\arg(g) = \arctan\left(\frac{Im[g]}{Re[g]}\right) \tag{8.31}$$

the *phase*. Then by taking the log of (8.29),

$$\log(g) = \log(\|g\|) + i \arg(g) \tag{8.32}$$

This logarithmic scaling has been proved to smoothen out the difference in the magnitude of the values for amplitude and phase. Taking the residual $\mathbf{g} - \mathcal{K}(\gamma)$ in the scaled data will produce a new residual:

$$\hat{\Xi}(\gamma) = \| \log(\mathbf{g}) - \log(\mathcal{K}(\gamma)) \|^2 \tag{8.33}$$

The Jacobian $\hat{J}$ then will be:

$$\hat{J}(\gamma) = \frac{\partial \log(\mathcal{K}(\gamma))}{\partial \gamma} = \text{diag}\left(\frac{1}{\mathcal{K}(\gamma)}\right) J(\gamma) \tag{8.34}$$

8.8 Numerical Results from 3D reconstructions

We consider some numerical results of the proposed method for reconstructions in optical tomography with frequency domain data. We are going to use the shape recovery approach with the utilisation of the spherical harmonics parametric surfaces. In the next sections we will try to portray the capabilities and the weaknesses of the proposed method in applications that have some interest for the medical world.

Specifically, we will begin with the effort for the reconstruction of an inhomogeneous region inside a realistic head geometry. Then the reconstruction of the actual shape of the brain will be attempted, in order to extract structural information for our model from optical measurements on the surface of the head. Finally, an attempt is made to test the simultaneous recovery of both optical and shape coefficients.

8.9 Region Recovery Inside Homogeneous Medium

In this experimental setup a geometric model that has resemblance to an infant's head is created and treated as a homogeneous domain with an embedded randomly shaped inhomogeneity, which we are called to recover.

Initially an MRI image of an infant's head was used to extract the surface of the outer boundary of the scalp in order to define the domain of our problem as shown in chapter 7. The parameter-

isation algorithm created a mapping on the sphere and a spherical mesh of 386 nodes and 192 surface elements was subsequently mapped on the parametric surface. The optical parameters chosen for this homogeneous background were set to $\mu_a = 0.01\ cm^{-1}$ and $\mu_s = 1.\ cm^{-1}$.

In the interior of the head surface a region Ω_2, with different optical properties of $\mu_a = 0.05\ cm^{-1}$ and $\mu_s = 2.\ cm^{-1}$ was placed. This second surface is described by 16 spherical harmonic coefficients γ_0 for each Cartesian coordinate $x,\ y,\ z$ defining a parametric surface using up to the 3^{rd} degree spherical harmonics. A regular mesh with 48 elements and 98 nodes, is mapped onto that surface to create the discrete approximation necessary for the BEM calculation.(see fig. 8.3)

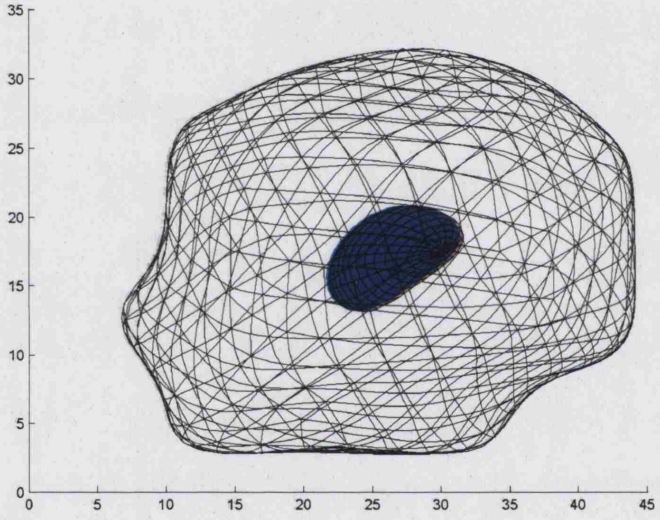

Figure 8.3: The geometrical setup for the calculation of the simulated data g

Using this geometric setup we assign 20 sources and 20 detectors positions on the surface of the head as seen in figure (8.1). The modulation frequency on the sources in set to $100MHz$. Synthetic data are then collected using the forward model $\mathcal{K}(\gamma_0)$ with one source illuminated at the time from the 20 detectors. This results in a measurements vector $\hat{g} \in \mathbb{C}^{400}$. To simplify further calculations we separate the real and imaginary part of the signal to get a vector $g \in \mathbb{R}^{800}$.

Gaussian random noise with deviation of 1% of the measured signal was added to the signal to compensate for the noise that exists in the real-life measurements.

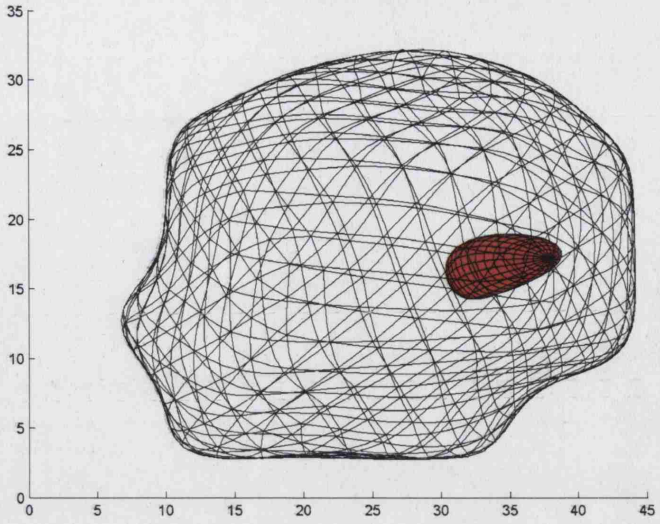

Figure 8.4: The geometrical setup with the initial estimation for the region Ω_2

For the inverse problem we select a closed surface placed at a random position as we can see in fig. (8.4). In this case we use 9 parameters for each direction in a 2^{nd} spherical harmonic degrees description. This choice leads to a search space of dimension 3×9.

The solution follows the residual minimisation technique described in section (8.3). The resulting boundary can be seen in fig.(8.5). Fig. (8.6) contains the relative data error $\|g\|^{-1}\|g - \mathcal{K}(\gamma_k, D, \mu_a)\|^2 \cdot 100\%$ versus iteration index k on the left.

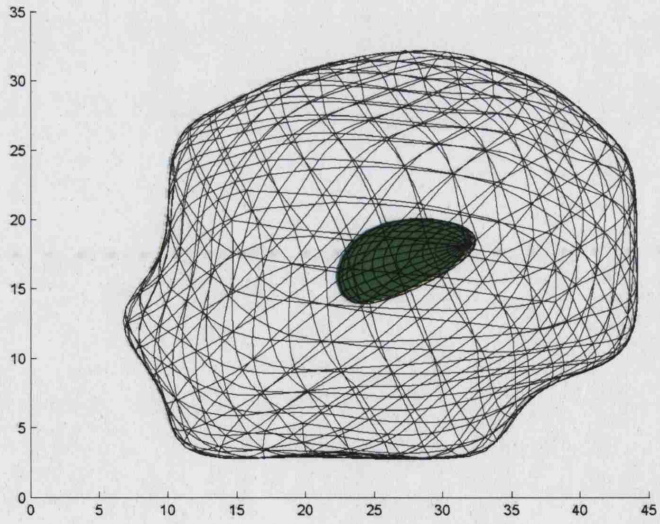

Figure 8.5: The solution for the region Ω_2

A measure for the goodness of the approximation of the surface used for the simulated data to

the one reconstructed from the minimisation of the least squares problem can be seen on fig. (8.6) on the right. This is actually from the boundary used for the simulated data and the one during the k^{th} iteration versus the iteration index k.

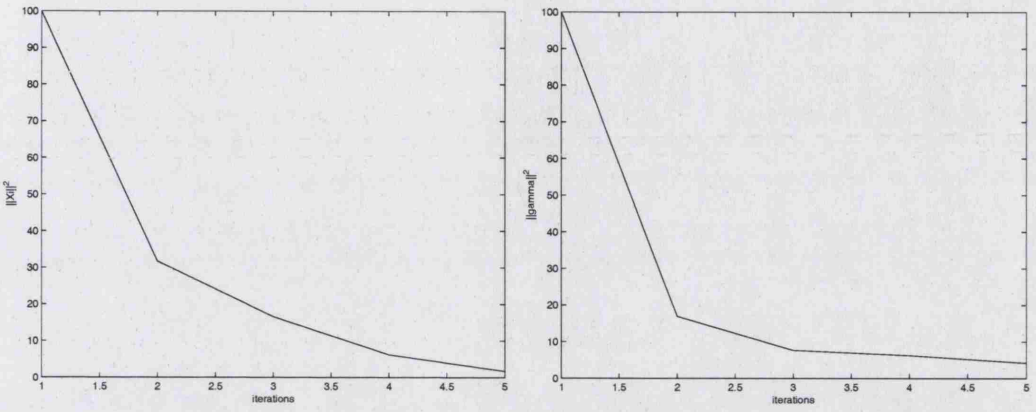

Figure 8.6: Relative data error, $\|g\|^{-1}\|g-\mathcal{K}(\gamma_k)\|^2 \cdot 100\%$ on the left, and the distance between the spherical harmonics coefficients $\|\gamma_0 - \gamma_k\|^2 \cdot 100\%$ on the right.

As can be seen, the location and the approximate shape of the simple 3D homogeneous region, fig. (8.3) can be recovered with good accuracy from noisy data, fig. (8.5). The minimisation of the least squares functional was successful with the distance norm becoming 100 times smaller that the initial value after only 5 iterations. On the other hand the distance between the shape coefficients shows good convergence if we consider that a different degree of spherical harmonics was used for the creation of the simulated data and a much lower for the perturbation shape.

8.10 Recovery of the brain surface from OT measurements

In this second experiment, we are interested in the recovery of the shape of the brain from OT measurements on the surface of an infants head. In this case we used the same scalp surface along with the brain described using 11^{th} degree spherical harmonics (see fig. (8.7)). The optical properties were set to $\mu_a = 0.01\ cm^{-1}$ and $\mu_s = 1.\ cm^{-1}$ for the homogeneous background. For the brain region we set $\mu_a = 0.05\ cm^{-1}$ and $\mu_s = 2.\ cm^{-1}$. Simulated measurements were created from the forward solution on the geometric setting shown in fig. (8.7).

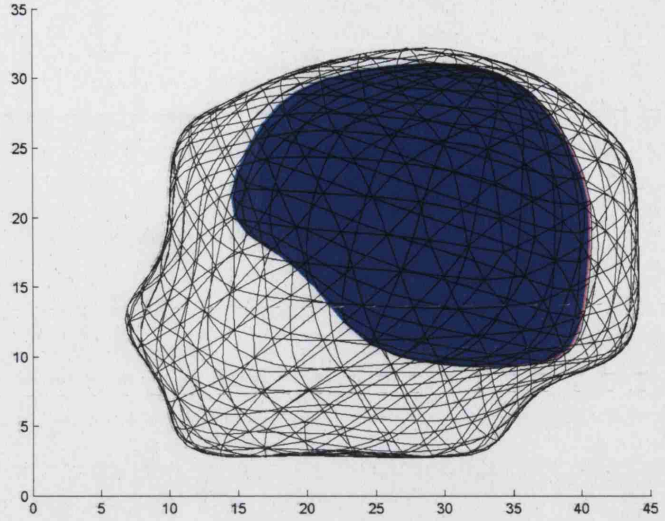

Figure 8.7: The geometrical model for the simulated data.

The perturbation shape then was initiated using 8 degrees of spherical harmonics, which made the search space having the dimension 81×3. The initial guess comes from a different head model that we constructed using MRI data and the spherical harmonics representation.

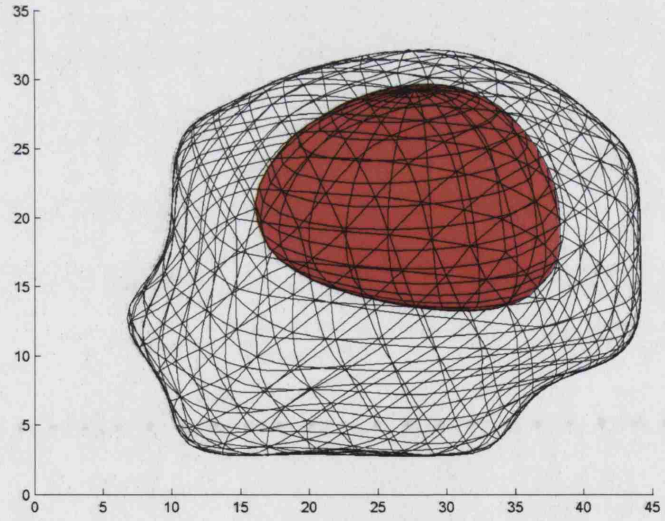

Figure 8.8: The initial guess for the brain shape.

The minimisation procedure followed the iteration step (8.10) with the scaled λ shown in fig.(8.9). In each iteration the lower degrees of shape coefficients are treated with a smaller value of $lambda$, which proved to increase the speed of the convergence for the lower shape description frequencies. As seen in fig.(8.9) the values for λ are updated after each iteration to

reduce that effect and allow the minimisation in the directions of the higher shape descriptor frequencies as well.

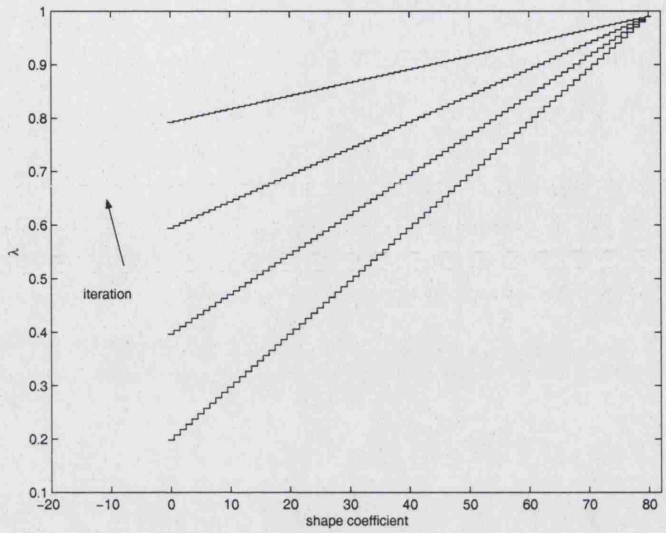

Figure 8.9: The values for the parameter λ chosen for the first 4 iterations of the minimisation algorithm.

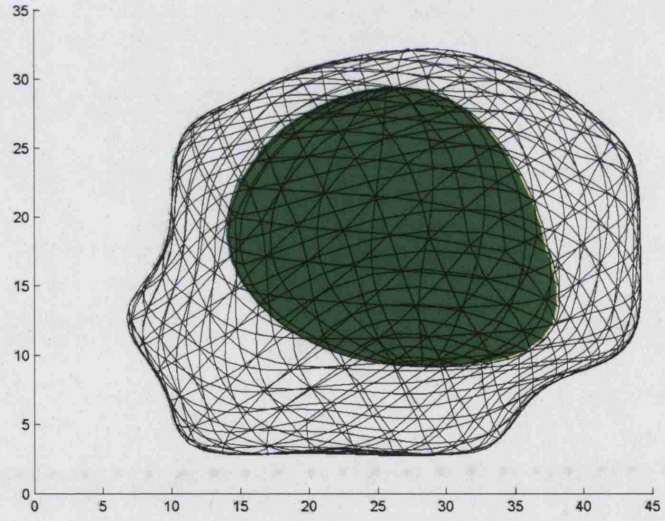

Figure 8.10: The estimation for the brain shape.

After 5 iterations only the minimisation has reached a local minimum as seen in fig.(8.10). The convergence in the least square distance between the simulated data and the ones created during the minimisation is shown in fig.(8.11). We noticed that this an approximation of the brain shape used for the simulated data (see fig. 8.8). The shape of the brain is not fully recovered but the results show steps towards that direction, especially if we consider the diffusive nature

of the OT measurement.

The introduction of an adaptable procedure that will increase the number of shape parameters along the iterations of the minimisation is suggested as future work. It will allow for the first few spherical harmonic coefficients to be reconstructed in the initial iterations before the highest frequencies, that define the finer details of the shape, enter the minimisation. Also the adoption of a more realistic initial guess, could improve the results.

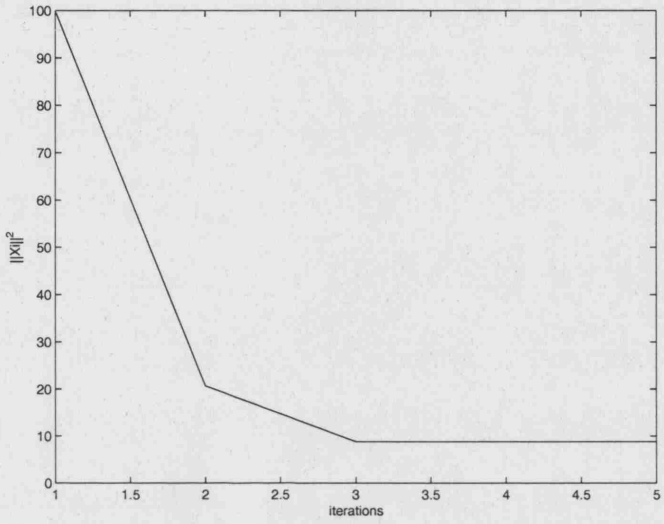

Figure 8.11: The relative data error, $\|g\|^{-1}\|g - \mathcal{K}(\gamma_k)\|^2 \cdot 100\%$

8.11 Simultaneous recovery of optical coefficients and shape parameters

This experiment extents the shape recovery method to the case where the values of μ_a are also considered as unknown variables. More precisely, the simulated data used are coming from section (8.9), created with optical properties of $\mu_{a,0} = 0.05\ cm^{-1}$ and $\mu_s = 2.\ cm^{-1}$ for the region Ω_2 and $\mu_a = 0.01\ cm^{-1}$ and $\mu_s = 1.\ cm^{-1}$ for the homogeneous background on the geometric set up of fig.(8.3).

In this case the initial estimation for the perturbation shape is again this of fig.(8.4) but the initial absorption coefficient μ_a for the region Ω_2 was set to $\mu_{a,1} = 0.1\ cm^{-1}$.

The search space for the least squares minimisation (8.7) is increased by one value corresponding to the absorption coefficient of the unknown region. The Jacobian used for the iteration of the modified Gauss-Newton method (8.10) has now one extra row to accommodate the deriva-

tive $\frac{\partial \mathcal{K}(\gamma,D,\mu_a)}{\partial \mu_a}$ of the forward operator in respect to the absorption coefficient for the region ω_2. The resulting shape estimation can be seen in fig.(8.12).

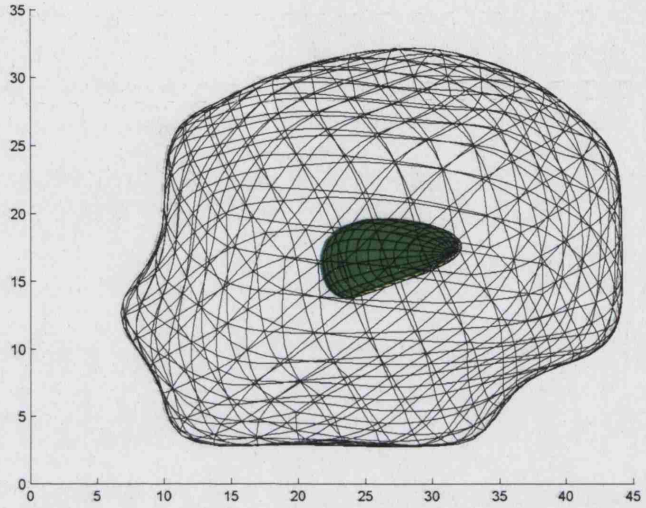

Figure 8.12: The solution with the value of the absorption coefficient for the region Ω_2 considered as unknown variable

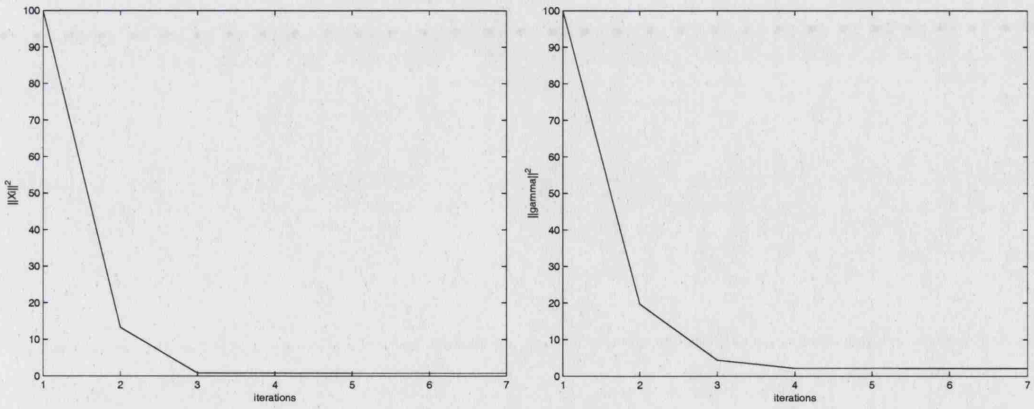

Figure 8.13: Relative data error, $\|g\|^{-1}\|g - \mathcal{K}(\gamma_k, \mu_{a,k})\|^2 \cdot 100\%$ on the left, and the distance between the spherical harmonics coefficients $\|\gamma_0 - \gamma_k\|^2 \cdot 100\%$ on the right.

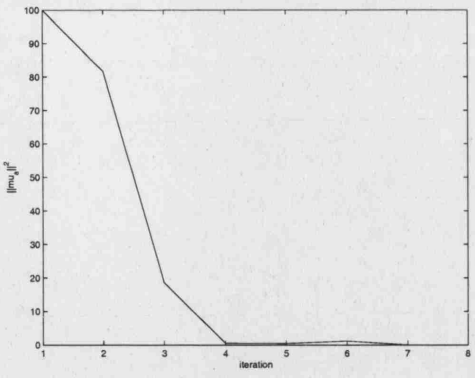

Figure 8.14: The relative error for μ_a, $\|\mu_{a,0}\|^{-1}\|\mu_{a,0}-\mu_{a,k}\|^2 \cdot 100\%$ plotted versus the iteration index k

The relative least squares distance between simulated and estimated measurements and also the distances between the actual shape coefficients and the recovered are presented in fig. (8.13). Those results indicate that the generalisation of the shape estimation method to include the recovery of unknown optical parameters is possible and the implementation straight forward. Fig. (8.14) shows the progress made for the value of the absorption coefficient, that started from the initial guess of $\mu_{a,1} = 0.1\ cm^{-1}$ to reach a good estimate $\mu_{a,k} = 0.0499\ cm^{-1}$ of the actual one $\mu_{a,0} = 0.05\ cm^{-1}$.

8.12 Summary

In this chapter we reviewed the theoretical background for the formulation of a shape based three dimensional forward and inverse problem for OT, in the search space of shape parameters defined from spherical harmonic coefficients. The techniques for parametrisation of closed surfaces and definition of regular meshes upon those parametric surfaces, the least squares minimisation and the boundary elements, presented in the previous chapters were combined in a shape based approach for the reconstruction of boundaries for regions with piecewise constant optical parameters. In addition some experiments with interest in the reconstruction of OT images, were presented, to explore the advantages and limitations of the proposed method.

More specifically, a recovery of a small region with a-priori known optical parameters embedded inside a realistic head model was attempted. The results were very promising with good convergence for both the measurements and the associated shape coefficients. Then the recovery of a brain region was attempted. In this case the results showed convergence but the size

of the regions and the large number of shape coefficients used for their representation proved problematic and possibly some kind of adaptable inversion that would start from a small number of shape coefficients and gradually would increase their number should be employed. Finally, the absorption coefficient was considered unknown and an inverse problem that recovered both shape and optical parameters was solved. The results in this case showed only small loss of convergence in comparison to the ones taken with the a-priori knowledge of the optical parameter.

Chapter 9

Conclusions and future work

This dissertation showed that a shape based approach for a non-linear ill-posed tomographic inverse problem is possible. Furthermore, the proposed approach is using an explicit shape representation that could now accommodate non star shaped objects as well. A 3D shape based reconstructions method from OT measurements was presented. The method, based on the assumption that the optical parameters inside a domain are distributed in piecewise constant regions, used parametrisation for the surfaces that bound those regions, to describe them in a finite number of spherical harmonic coefficients. A forward and inverse problem was then constructed in the search space defined from those shape coefficients. The forward problem was solved using a boundary element method, and following on, the inversion was attempted based on a least squares minimisation to recover the shape coefficients.

Chapter 2 briefly presented the theoretical framework for the forward and inverse problems on tomographic and imaging applications. The review was concentrated in the existing shape based approaches from literature, supporting the need for a contribution in this area that could reconstruct three-dimensional boundaries from regions that do not necessary fell in the set of star-shaped objects.

Chapter 3 dealt with the physical model and the commonly used experimental setup for measurements in OT. This chapter gave a background on the details of the forward model that we used in the shape reconstruction method. The assumptions taken by the diffusion approximation and the techniques used by clinicians for the acquisition of measurements in OT were of fundamental importance for the establishment of realistic simulations from the solution of the forward problem. The problematic behaviour of the diffusion approximation for clear regions

where scattering is minimal, as it is in the Cerebrospinal fluid, were not part of this work, but are considered to be an important subject for future applications.

The necessity for a numerical method that could integrate the piecewise constant regions with the physical model for the propagation of light led to the choice of the boundary elements method. The method is well established, with many references in literature. In chapter 4 a BEM formulation for OT was described. The BEM proved an indispensable tool for the construction of simulated OT measurements in the shape based approach since it provided a safe option for numerical calculations in 3D with a natural capability to deal with surfaces changes.

Chapter 5 dealt with the elementary notions involved in an optimisation problem and some of the most widely used gradient methods for iterative minimisation of a functional. This background chapter provided an understanding of the optimisation methods used for the minimisation of the least squares formulation that governed the inverse problem and likewise for the constrained optimisation used for the surface's mapping on the sphere.

Chapter 6, presented the mapping for closed surfaces extracted from voxel images of biological tissue acquired from CT or MRI upon a unit sphere. The proposed method works with the net of connected nodes from the surface's of voxel object's and therefore overcomes the limitation for star-shaped objects, commonly found in literature. Formed as a constrained optimisation problem for minimisation of distortions and annihilation of discontinuities works on the distribution for the net of connected nodes on a unit sphere. This method satisfied the needs for an explicit shape parametrisation necessary for the shape based reconstruction. In chapter 7, spherical harmonics and a least squares fitting were employed to create an estimation of the original voxel objects by a finite set of weighted spherical harmonic coefficients. The results show a representation of the geometries involved in a human head as functions of the two spherical coordinates. The creation of a mesh, initially on the sphere's surface by the tessellation of an embedded icosahedron, and the mapping upon the parametric surface has produced results with evenly spaced elements, a prerequisite for the minimisation of numerical errors in BEM.

Chapter 8 presented a shape based approach for tomographic reconstructions in OT with preliminary results that display the capabilities of such an approach. This chapter discussed the forward and inverse shape based problem formulated from the use of the spherical harmonics shape parametrisation and the boundary elements method in OT. The parametrisation algorithm

provided the connection between original structural data from MRI or CT and the parametric description for boundaries of regions with piecewise constant optical parameters. The meshing algorithm linked the parameters describing the shape of the domain Ω with the numerical BEM solution following the physical laws that govern the transportation of light in that scattering body.

Following, the forward problem was defined as the mapping from the shape and optical parameters to the actual measurements on the surface $\partial\Omega$. The related inverse problem was then formulated as the recovery of those shape parameters that will minimise the distance between the simulated/observed data and the solution of the forward problem starting from some initial guess for those parameters. For the minimisation of this distance a least squares formulation was used with an iterative Gauss-Newton method. The necessary Jacobian was calculated using finite differences. Our future work will involve further investigation into the possibility for an analytic Jacobian of either the forward operator or the BEM matrix in respect to the shape parameters, [72, 80].

The possible applications for such a method are numerous. We included a few examples showing the good convergence of the method for the recovery of the position and approximate shape of a inhomogeneity inside a homogeneous domain of approximated realistic geometry for two cases, one using spherical harmonic coefficients up to the 3^{rd} degree and one using up to the 8^{th}. The results were satisfactory for both cases, even though the involvement of less shape parameters for the description of the surface provided faster and more accurate convergence. To deal with this effect, an adaptable approach that will start with a description of the evolving shape in few degrees of spherical harmonics and iteratively will add the higher frequencies is in our future plans.

Finally, an extension to our approach was tested with the case where the values of the optical coefficients are also set as unknown variables in our problem. This experiment indicated that the accuracy on the values of the *a-priori* known optical parameters, in this case the absorption coefficient, is not of fundamental importance for the actual reconstruction in a shape based approach. We consider this initial result as a stimuli for further experimentation.

To sum up, we consider the results exciting and showing the possibilities for improvement in the currently used pixel basis approaches for reconstruction in OT. In our future plans we are

also going to explore the possibility that actual OT clinical measurements could be used for reconstructions with this shape based approach.

Bibliography

[1] P.K. Agarwal and S. Suri. Surface approximation and geometric partitions. *Proceedings of 5th ACM-SIAM Symposium on Discrete Algorithms*, pages 24–33, 1994.

[2] A.G.Yodh and D.A.Boas. *Biomedical Photonics Handbook.* CRC Press, 2003.

[3] G. Alessandrini, E. Baretta, F. Santosa, and S. Vessella. Stability in crack determination from electrostatic measurments at the boundary - a numerical investigation. *Inverse Problems*, 11:17–24, 1995.

[4] G. Alessandrini and L. Rondi. Stable determination of a crack on a planar inhomogeneous conductor. *SIAM J. Math. Anal.*, 30:326–340, 1998.

[5] G. Alessandrini and E. Rosset. The inverse problem with one measurement : Bounds on the size of the unknown object. *SIAM J. Appl Math.*, 58, 1998.

[6] P. Alfeld, M. Neamtu, and L.L. Schumaker. Fitting scattered data on sphere-like surfaces using spherical splines. *J. Comp. Appl. Math.*, 73:5–43, 1996.

[7] A.Litman, D.Lesselier, and F.Santosa. Reconstruction of a two-dimensional binary obstacle by controlled evolution of a level-set. *Inverse Problems*, 14:685–706, 1998.

[8] A.P.Gibson, J.C.Hebden, and S.R.Arridge. Recent advances in diffuse optical imaging. *Phys. Med. Biol*, submitted 2004.

[9] A.Roger. Reciprocity theorem applied to the computation of functional derivatives of the scattering matrix. *Electromagnetics*, 2:69–83, 1982.

[10] S. R. Arridge, H. Dehghani, M. Schweiger, and E. Okada. The finite element model for the propagation of light in scattering media : A direct method for domains with non-scattering regions. *Med. Phys.*, 27:252–264, 2000.

[11] S.R. Arridge. Optical tomography in medical imaging. *Inverse Problems*, 15:41–93, 1999.

[12] S.R. Arridge, M. Cope, and D.T. Deply. The theoretical basis for the determination of optical pathlengths in tissue: temporal and f requency analysis. *Phys. Med. Biol.*, 37(7):1531–1560, 1992.

[13] S.R. Arridge and M. Schweiger. A general framework for iterative reconstruction algorithms in optical tomography, using a finite element method. In C. Borgers and F. Natterer, editors, *In Computational Radiology and Imaging : Therapy and Diagnosis*, IMA Volumes in Mathematics and its Applications, pages 45–70. Springer-Verlag (Berlin), 1998.

[14] S.R. Arridge, M. Schweiger, M. Hiraoka, and D.T. Delpy. A finite element approach for modelling photon transport in tissue. *Med.Phys.*, 20:299–309, 1993.

[15] U. Ascher, S. Pruess, and R.D. Russell. On spline basis selection for solving differential equations. *SIAM journal on Numerical Analysis*, 20(1), 1983.

[16] A.A. Becker. *The Boundary Element Method in Engineering - A Complete Course.* McGraw-Hill Book Company, 1992.

[17] G. Beer. *Programming the Boundary Element Method: An Introduction for Engineers.* John Wiley and Sons, 2001.

[18] A. Björck. *Numerical Methods for Least Square Problems.* SIAM, 1996.

[19] D. A. Boas, M. A. O'Leary, B. Chance, and A. G. Yodh. Scattering of diffuse photon density waves by spherical inhomogeneities within turbid media: Analytic solution and applications. *Proc. Natl. Acad. Sci. USA*, 91:4887–4891, 1994.

[20] M. Bonnet. *Boundary Integral Equation Methods for Solids and Fluids.* John Wiley and Sons, 1995.

[21] C.P. Bradley, A.J. Pullan, and P.J. Hunter. Geometric modelling of the human torso using cubic Hermite elements. Technical report, Department of Engineering Science, University Of Auckland, New Zealand, 1997.

[22] C. Brechbühler. Constraint optimization, extended version of chapter 2 in " Imposing hard constraints on soft snakes" by P. Fua and C. Brechbühler. *[46]*, 1996.

[23] C. Brechbühler, G. Gerig, and O. Kübler. Parameterization of closed surfaces for 3-D shape description. *Computer Vision and Image Understanding*, 61(2):154–170, 1995.

[24] C.M. Brechbühler-Miskuv. *Description and analysis of 3-D shapes by parametrization of closed surfaces.* PhD thesis, Swiss Federal Institue of Technology Zurich, 1995.

[25] B.U.Koo. Shape design sensitivity analysis of acoustic problems using a boundary element method. *Computer and Structures*, 65(5):713–719, 1997.

[26] A. Crouzeix, B. Yvert, O. Bertrand, and J. Pernier. An evaluation of dipole reconstruction accuracy with spherical and realistic head models in MEG. *Electroenceph. Clin. Neurophysiol.*, 110(12):2176–2188, 1999.

[27] C.A. Davatzikos and J.L. Prince. An active contour model for mapping the cortex. *JHU-ECE Technical Report 93-06*, 1993.

[28] J.C. de Munck, T.J.C. Faes, and R.M. Heethaar. The boundary element method in the forward and inverse problem of electrical impedance tomography. *IEEE transactions on Biomedical Engineering*, 47(6):792–800, 2000.

[29] O. Dorn. A transport-backtransport method for optical tomography. *Inverse Problems*, 14(5):1107–1130, 1998.

[30] R. Duraiswami, G.L. Chanine, and K. Sarkar. Boundary element techniques for efficient 2-D and 3-D electrical impedance tomography. *Chemical Engineering Science*, 52(13):2185–2196, 1997.

[31] R. Duraiswami, K. Sarkar, and G.L. Chanine. Efficient 2D and 3D electrical impedance tomography using dual reciprocity boundary element techniques. *Engineering Analysis with Boundary Elements*, 22:13–31, 1998.

[32] G. Eason, A.R.Veitch, R.M.Nisbet, and F.W.Turnbull. The theory of the back-scattering of light by blood. *J. Rhys. D: Appl. Phys*, 11:1463–1479, 1977.

[33] M. Eck and H. Hoppe. Automatic reconstruction of B-Spline surfaces of arbitrary topological type. *SIGGRAPH 96 Conference Proceedings*, 1996.

[34] K. Eppler and H. Harbrecht. 2nd order shape optimization using wavelet BEM. *Optim. Methods Softw.*, 2003.

[35] K. Eppler and H. Harbrecht. Numerical solution of elliptic shape optimization problems using wavelet-based BEM. *Optim. Methods Softw.*, 18:105–123, 2003.

[36] E.Praun and H.Hoppe. Spherical parametrization and remeshing. *ACM Trans. Graph.*, 22(3):340–349, 2003.

[37] S.C. Fan and M.H. Luah. Free vibration analysis of arbitrary thin shell structures by using finite element. *Journal Of Sound and Vibration*, 179(5):763–776, 1995.

[38] G.E. Fasshauer and L.L. Schumaker. Scattered data fitting on the sphere. *Mathematical Methods for Curves and Surfaces II*, pages 117–166, 1998.

[39] F.Bruce, M.I.Sereno, and A.M.Dale. Cortical surface-based analysis ii: Inflation, flattening, and a surface-based coordinate system. *NeuroImage*, 9(2):195–207, 1999.

[40] T.C. Ferree. Spline interpolation of the scalp EEG. Technical report, Electrical Geodesics, Inc., 2000.

[41] M. Firbank, S. R. Arridge, M. Schweiger, and D. T. Delpy. An investigation of light transport through scattering bodies with non-scattering regions. *Phys. Med. Biol.*, 41:767–783, 1996.

[42] R. Fletcher. *Practical Methods of Optimization, Second Edition.* Wiley-Interscience Publication, 1996.

[43] J.D. Foley, A. Van Dam, S. Feiner, J. Hughes, and R. Phillips. *Introduction to Computer Graphics.* Addison-Wesley, 1993.

[44] W. Freeden, M. Schreiner, and R. Franke. A survey on spherical spline approximation. *Surveys on Mathematics for Industry*, 1997.

[45] F.Santosa. A level-set approach for inverse problems involving obstacles. *ESAIM : Control, Optimisation and Calculus of Variations*, 1:17–33, 1996.

[46] P. Fua and C. Brechbühler. Imposing hard constraints on deformable models through optimization in orthogonal subspaces. *Computer Vision and Image Understanding*, 65(2):148–162, 1997.

[47] T. Funkhouser, P. Min, M. Kazhdan, J. Chen, A. Halderman, D. Dobkin, and D. Jacobs. A searce engine for 3D models. *ACM Tranaactions on Graphics*, 22:83–105, 2003.

[48] C. Greenough and K. Robinson. *Finite Element Library.* Rutherford Appleton Laboratory, 1981.

[49] L. Grisoni, C. Blanc, and C. Schlick. Hermitian B-splines. *Computer Graphics Forum,*, 18(4), 1999.

[50] Zhou H and van Oosterom A. Electrical impedance tomography. solving anisotropic mixed boundary value problems by means of the boundary element method. *Clin Phys Physiol Meas.*, 13:131–133, 1992.

[51] W.S. Hall. *The Boundary Element Method.* Kluwer, Academic Publishers, 1994.

[52] H.B.Ameur, M.Burger, and B.Hackl. Level set methods for geometric inverse problems in linear elasticity. *Inverse Problems*, 20:673–696, 2004.

[53] J. C. Hebden, A. P. Gibson, T. Austin, R. Md. Yusof, N. Everdell, D. T. Delpy, S. R. Arridge, J. H. Meek, and J. S. Wyatt. Imaging changes in blood volume and oxygenation in the newborn infant brain using three-dimensional optical tomography. *Phys. Med. Biol.*, 49(7):1117–1130, 2004.

[54] J. Heino and E. Somersalo. Estimation of optical absorption in anisotropic background. *Inverse Problems*, 18:559–573, 2002.

[55] S.A. Mehrdad Mohammad Hejazi. *Parametric Cubic Spline Finite Element Method.* PhD thesis, University of London, 1997.

[56] F. Hettlich and W. Rundell. Iterative methods for the reconstruction of the inverse potential problem. *Inverse Problems*, 12:251–266, 1996.

[57] F. Hettlich and W. Rundell. Recovery of the support of a source term in an elliptic differential equation. *Inverse Problems*, 13:959–976, 1997.

[58] F. Hettlich and W. Rundell. The determination of a discontinuity in a conductivity from a single boundary measurement. *Inverse Problems*, 14:67–82, 1998.

[59] H.Tortel. Localization and derivation of an optimal sphere for 3d perfectly conducting objects. *Journal of Electromagnetism, Waves and Applications*, 16:771–791, 2002.

[60] H.Tortel. Electromagnetic imaging of a three-dimensional perfect conducting object using a boundary integral formulation. *Inverse Problems*, 20:385–398, 2004.

[61] A. Ishimaru. *Wave Propagation and Scattering in Random Media*, volume 1. New York: Academic, 1978.

[62] A. Ishimaru. *Wave Propagation and Scattering in Random Media.* IEEE/OUP series on Electromagnetic Wave Theory, 1997.

[63] Jr. J.E.Dennis and Robert B. Schnabel. *Numerical Methods for Unconstraint Optimisation and Nonlinear Equations.* Siam, 1996.

[64] J.Haslinger and R.A.E.Mäkinen. *Introduction to Shape Optimization.* SIAM, 2003.

[65] J.Nocedal and S.J.Wright. *Numerical Optimization.* Springer, 1999.

[66] P. Kagan, A. Fischer, and P.Z. Bar-Yoseph. Mechanically based design: Adaptive refinement for B-spline finite element. *International Conference on Shape Modeling and Applications*, pages 345–353, 2001.

[67] I.T. Katsikadeles. *Συνοριακα Στοιχεια στην επιστημη του Μηχανικου.* Symeon, 1999.

[68] P.G. Kaup, F. Santosa, and M. Vogelius. Method for imaging corrosion damage in thin plates from electrostatic data. *Inverse Problems*, 12:279–293, 1996.

[69] M.E. Kilmer, E.L. Miller, A. Barbaro, and D. Boas. 3D shape-based imaging for diffuse optical tomography. *Applied Optics*, 42:3129–3144, 2003.

[70] V. Kolehmainen. *Novel approaches to image reconstruction in diffusion tomography.* PhD thesis, University of Kuopio, Finland, 2001.

[71] V. Kolehmainen, S.R. Arridge, W.R.B. Lionheart, M. Vauhkonen, and J.P. Kaipio. Recovery of region boundaries of piecewise constant coefficients of an elliptic PDE from boundary data. *Inverse Problems*, 15:1375–1391, 1999.

[72] V. Kolehmainen, S.R. Arridge, M. Vauhkonen, and J.P. Kaipio. Recovery of constant coefficients in optical diffusion tomography. *Optical Express*, 7:468–480, 2000.

[73] L. Lapidus and G.F. Pinder. *Numerical Solutions of Partial Differential Equations in Science and Engineering.* John Wiley and Sons, 1999.

[74] J.D. Logan. *Applied Partial Differential Equations.* Springer, 1998.

[75] W.E. Lorensen and H.E. Cline. Marching cubes: A high resolution 3D surface construction algorithm. *Computer Graphics*, 21(4):163–169, 1987.

[76] J.D. MacDonald. *A Method for Identifying Geometrically Simple Surfaces from Three Dimensional Images.* PhD thesis, School of Computer Science, McGill University, Montreal, 1997.

[77] M.Alexa. Recent advances in mesh morphing. *Computer Graphics Forum*, 21(2):173–196, 2002.

[78] D. W. Marquardt. An algorithm for least-squares estimation of nonlinear parameters. *J. Soc. Industrial Math*, 11(2):431–441, 1963.

[79] M.Bertero and P.Boccacci. *Introduction to Inverse Problems in Imaging.* IoP, 1998.

[80] M.Bonnet. Bie and material differentiation applied to the formulation of obstacle inverse problems. *Engineering Analysis with Boundary Elements*, 15:121–136, 1995.

[81] M.Bonnet. Boundary element based formulations for crack shape sensitivity analysis. *Engineering Analysis with Boundary Elements*, 25:347–362, 2001.

[82] M.Burger. A level set method for inverse problems. *Inverse Problems*, 17:1327–1355, 2001.

[83] M.H.Aliabadi. *The boundary element method.* Wiley, 2002.

[84] M.Hämäläinen, R.Hari, R.J.Llmoniemi, J.Knuutila, and O.V.Lounasmaa. Magnetoencephalography - theory, instrumentation, and applications to noninvasive studies of the working human brain. *Previews of Modern Physics*, 65(2):413–497, 1993.

[85] A. Mohamed and C. Davatzikos. Finite element mesh generation and remeshing from segmented medical images. *Proceedings of the 2004 IEEE International Symposium on Biomedical Imaging: From Nano to Macro, Arlington, VA, USA, 15-18 April 2004*, pages 420–423, 2004.

[86] M.J. Mohlenkamp. A fast transform for spherical harmonics. *The Journal of Fourier Analysis and Applications*, 5(2/3):159–184, 1998.

[87] M. Müller, F. Sachse, and C. Meyer-Waarden. Creation of finite element models of human body based upon tissue classified voxel representations. *http : //www.nlm.nih.gov/research/visible/vhp$_c$onf/mueller/paper.htm*, -.

[88] V. Nassehi and J. Petera. A new general-purpose leat square Finite Element model for steady incompressible low-viscosity laminar flow using isoparametric c^1 continuous Hermite elements. *Int. Journ. for Numer. Methods in Fluids*, 18:215–226, 1994.

[89] I. Nissila, K. Kotilahti, K.Fallstrom, and T. Katila. Instrumentation of the accurate measurement of phase and amplitude in optical tomography. *Review of Scientific Instruments*, 73(9):3306–3312, 2002.

[90] O.Dorn, E.L.Miller, and C.M.Rappaport. A shape reconstruction method for electromagnetic tomography using adjoint fields and level sets. *Inverse Problems*, 16:1119–1156, 2000.

[91] M. A. OLeary, D. A. Boas, B. Chance, and A. G. Yodh. Simultaneous scattering and absorption images of heterogeneous media using diffusive waves with the rytov approximation. *Optical Tomography: Photon Migration, and Spectroscopy of Tissue and Model Media: Theory, Human Studies, and Instrumentation, B. Chance and R. R. Alfano, eds., Proc. SPIE*, 2389:320–327, 1995.

[92] J. Ollikainen, M. Vauhkonen, P.A. Karjalainen, P.J. Ronkanen, and J.P. Kaipio. Effect of skull inhomogeneities on EEG localization accuracy. *Procced. 19th Intern. Conf. IEEE/EMBS*, 1997.

[93] S.J. Park and T.H.Kwon. Sensitivity analysis formulation for three-dimensional conduction heat transfer with complex geometries using a boundary element method. *International Journal for numerical Methods in Engineering*, 39:2837–2862, 1996.

[94] P.E.Gill, W.Murray, and M.H.Wright. *Practical Optimization.* Academic Press Inc., 1981.

[95] J. Petera and J.F.T. Pittman. Isoparametric Hermite elements. *International Journal for Numerical Methods in Engineering*, 37:3489–3519, 1994.

[96] R. Pfeifle and H. Seidel. Spherical triangular B-splines with application to data fitting. *Proc. Eurographics,*, pages 89–96, 1995.

[97] W.H. Press, B.P. Flannery, S.A. Teukolsky, and W.T. Vetterling. *Numerical Recipes in C, The Art of Scientific Computing.* Cambridge University Press, 2001.

[98] A. Pullan. *FEM - BEM Notes.* Department of Engineering Science, The University of Auckland, New Zealand, 2001.

[99] M. Quicken, C. Brechbühler, J. Hug, H. Blattmann, and G. Szkely. Parametrization of closed surfaces for parametric surface description. *Computer Vision and Pattern Recognition*, 1:354–360, 2000.

[100] R.Aithal and S. Saigal. Shape sensitivity analysis in thermal problems using BEM. *Engineering Analysis with Boundary Elements*, 15:115–120, 1995.

[101] C. Ramananjaona, M. Lambert, D. Lesselier, and J-P. Zolesio. Shape reconstruction of buried obstacles by controlled evolution of a level set: from a min-max formulation to numerical experimentation. *Inverse Problems*, 17:1087–1111, 2000.

[102] R.A.Meric. Differential and integral sensitivity formulations and shape optimisation by BEM. *Engineering Analysis with Boundary Elements*, 15:181–188, 1995.

[103] A.G Ramm and A.I.Katsevich. *The Radon Transform and Local Tomography*. CRC press, 1996.

[104] J. Riley, H. Dehghani, M. Schweiger, S.R. Arridge, J. Ripoll, and M. Nieto-Vesperinas. 3D optical tomography in the presence of void regions. *Optics Express*, 7(13):462–467, 2000.

[105] J. Ripoll. *Light Diffusion in Turbid Media with Biomedical Application*. PhD thesis, Science Faculty of the Universidad Autonoma of Madrid, 2000.

[106] J. Ripoll, S. R. Arridge, H. Dehghani, and M. Nieto-Vesperinas. Boundary conditions for light propagation in diffusive media with nonscattering regions. *J. Opt. Soc. Am. A*, 17(9):1671–1681, 2000.

[107] J. Ripoll, V. Ntziachristos, R. Carminati, and M. Nieto-Vesperinas. Kirchhoff approximation for diffusive waves. *Phys. Rev. E*, 64, 2001.

[108] J. Ripoll, V. Ntziachristos, J. P. Culver, D. N. Pattanayak, A. G. Yodh, and M. Nieto-Vesperinas. Recovery of optical parameters in multiple layered diffusive media: Theory and experiments. *J. Opt. Soc. Am. A.*, 18:821–830, 2001.

[109] Youcef Saad and Martin H Schultz. GMRES: a generalized minimal residual algorithm for solving nonsymmetric linear systems. *SIAM J. Sci. Stat. Comput.*, 7(3):856–869, 1986.

[110] M.A. Sabin. *Spline Finite Elements*. PhD thesis, University of Cambridge, Department of Applied Mathematics and Theoretical Physics, September 1997.

[111] P. Schröder and W. Sweldens. Spherical wavelets. *In Proceedings of Siggraph 95*, 1995.

[112] W.J. Schröeder, J.A. Zarge, and W.E. Lorensen. Decimation of triangle meshes. *Computer Graphics*, 26(2):65–70, 1992.

[113] L.L. Schumaker. On super splines and finite elements. *SIAM Jour. on Numer. Anal.*, 26(4):997–1005, 1989.

[114] M. Schweiger, S.R. Arridge, M. Hiraoka, and D.T. Delpy. The finite model for the propagation of light in scattering media: Boundary and source conditions. *Med. Phys.*, 22:1779–1792, 1995.

[115] M. Schweiger, S.R.Arridge, M.Hiraoka, and D.T.Delpy. The finite element method for the propagation of light in scattering media:boundary and source conditions. *Medical Physics*, 22:1779–1791, 1995.

[116] J.A. Sethian. *Level Set Methods*. Cambridge University Press, 1996.

[117] G. Sewell. *The Numerical Solution of Ordinary and Partial Differential Equations*. Academic Press,Inc., 1988.

[118] J. R. Shewchuk. An introduction to the conjugate gradient method without the agonizing pain. Technical report, Carnegie Mellon University, 1994.

[119] H. Shum, M. Hebert, and K. Ikeuchi. On 3D shape similarity. *Proceedings of the IEEE Conference on Computer Vision and Pattern Recognition (CVPR '96)*, pages 526 – 531, 1996.

[120] J. Sikora. Boundary element method in optical tomography. Technical report, Dept of Computer Science, UCL, 2001.

[121] J. Sikora and S.R. Arridge. Some numerical aspects of 3D BEM application to optical tomography. *IV International Workshop Computational Problems of Electrical Engineering*, 2002.

[122] J. Sikora, S.R. Arridge, J. Ripoll, A.D. Zacharopoulos, and J.D. Riley. Light propagation in diffusive media with non-scattering regions using 3D BEM. *Boundary Integral Methods: Theory and Applications, University of Reading, 14-18 September*, 2004.

[123] W.M. Smart. *Textbook on Spherical Astronomy*. Cambridge University Press, sixth edition edition, 1977.

[124] S.Osher and R.Fedkiw. *Level Set Methods and dynamic Implicit Surfaces*. Springer, 2003.

[125] W.A. Strauss. *Partial Differential Equations, An Introduction*. John Wiley and Sons,Inc., 1992.

[126] J. K. Udupa and V. G. Ajjanagadde. Boundary and object labelling in three-dimensional images. *Comput. Vision Graph. Image Process.*, 51(3), 1990.

[127] M. Unser. Splines, a perfect fit for signal and image processing. *IEEE Signal Processing Magazine*, 1999.

[128] C.R. Vogel. *Computational Methods for Inverse Problems*. Number 23 in Frontiers in Applied Mathematics Series. SIAM, 2002.

[129] G. Wahba. Spline interpolation and smoothing on the sphere. *J. Sci. Stat. Comput.*, 2:5–16, 1981.

[130] Q.F. Wang. Spline finite member element method for vibration of thin walled members with shear lag. *Journ. of Sound and Vibration*, 206(3):339–352, 1997.

[131] Y. Yamada. Diffusion coefficient in the photon diffusion equation optical tomography, photon migration, and spectroscopy of tissue and model media: Theory, human studies, and instrumentation. *Proc. SPIE 2389*, pages 87–97, 1995.

[132] A. Zacharopoulos, J. Sikora, and S. Arridge. Parametric surface models in medical imaging. *Proc. Institute of Physics and Engineering in Medicine 10th Annual Scientific Meeting, York, 6 - 8 September*, 2004.

[133] A. Zacharopoulos, J. Sikora, and S. Arridge. Reconstruction of 3d region boundaries in optical tomography using parametric surfaces and bem. *Proc. IMA 3rd International Conference on Boundary Integral Methods: Theory and Applications, University of Reading, 14-18 September.*, 2004.

[134] A.D. Zacharopoulos. A parameterisation of closed surfaces for parametric surface description using spherical harmonics. Master's thesis, Dept. of Computer Science, UCL, 2000.

[135] A.D. Zacharopoulos and S.R. Arridge. Surface mesh creation for 3D objects with sphere topology by homeomorphism on a unit sphere. In *Proc. IV International Workshop on Computational Problems of Electrical Engineering*, pages 211–215, 2002.

[136] P-B. Zhou. *Numerical Analysis of Electromagnetic Fields*. Springer-Verlag, 1993.

[137] O.C. Zienkiewicz and R.L. Taylor. *The Finite Element Method*, volume 1. McGraw-Hill, 4th edition, 1989.